HEMATOCRIT-CORRECTED DIFFUSE OPTICAL MONITORING OF BLOOD FLOW AND OXYGEN METABOLISM DURING CARDIOPULMONARY BYPASS

Emilie J. Benson

A DISSERTATION

in

Physics and Astronomy

Presented to the Faculties of the University of Pennsylvania

in

Partial Fulfillment of the Requirements for the

Degree of Doctor of Philosophy

2023

Supervisor of Dissertation

Arjun G. Yodh

James M. Skinner Professor of Science and
Department Chair, Department of Physics and
Astronomy

Co-Supervisor of Dissertation

Wesley B. Baker

Assistant Professor of Neurology and Director of
Biomedical Optical Devices to Monitor Cerebral
Health Frontier Program, CHOP

Graduate Group Chairperson

Ravi K. Sheth, Professor of Physics and
Astronomy

Dissertation Committee

Philip Nelson, Professor of Physics and Astronomy

I. Joseph Kroll, Professor of Physics and Astronomy

Evelyn Thomson, Professor of Physics and Astronomy

HEMATOCRIT-CORRECTED DIFFUSE OPTICAL MONITORING OF BLOOD FLOW AND OXYGEN METABOLISM DURING CARDIOPULMONARY BYPASS

COPYRIGHT

2023

Emilie Jan Benson

For all the small-town, ordinary girls.

ACKNOWLEDGEMENTS

There are so many people that I need to acknowledge who have helped to make it possible to complete my PhD. I would like to start by thanking my parents as they have been there from the beginning. My parents, Lisa and Brent Benson, have always encouraged my love of science and inquisitive outlook on life. They have supported me through all of my decisions, including the one to move to the East Coast to pursue a doctorate in something neither of them understood. Continuing in chronological order, I would also like to thank both of my brothers, Nick and Tim Benson, who have challenged me in so many ways, but have always had my back when it matters. I even convinced Tim to move to Philadelphia and work in the lab for a year, and it turned out he was the best roommate I could have asked for.

I would also like to thank my undergraduate friends and mentors from Gustavus. The friends I made there continue to be my closest friends – Eric Hanson, Caroline David, and Morgan Timm. I am so grateful for your unending support and encouragement. Thank you for your willingness to hop on a plane or send encouragement from afar. Thank you to my undergraduate advisors, Chuck Niederieter and Jessie Petrika, for cultivating my love for teaching and encouraging me to pursue my doctorate.

I was also fortunate enough to make some great friends during my graduate studies at Penn. I am thankful for the comradery that my cohort shared; especially Sophie Ettinger, Jesse Hanlan, Matt DeCross and Jack Orlowski-Scherer who supported me both in and out of the classroom, and for encouraging me to follow my gut as I switched research fields after my third year at Penn. I am grateful for the opportunity to be a fellow with the Center for Teaching and Learning which allowed me to focus more on teaching and education for a year. During that fellowship, I was also able to work with Cathy Turner and Ian Petrie, who encouraged my passion for teaching but were also supportive of my interest in pursuing to science policy. And to the other women I met studying physics – Analisa Hill, Charlotte Slaughter and Yvonne Zagzag – you are some of the smartest and toughest people I know.

I learned the medical terminology and later respecting my opinion and needs as a scientist. You all helped in so many ways as I grew as a researcher.

Last, but certainly not least, I would like to thank those who I have met in Philly who have become my family over the past few years. First, to my partner Christopher Perkes who has encouraged and supported me throughout this, and so many other, endeavors. I would also like to thank my whole medical treatment team as I hit several medical roadblocks of my own throughout my time as a graduate student. And to the close friends I have made along the way, Elizabeth Chagnon, Elizabeth Yutzey and Kate McCammon. I never expected to have people who understand me the way that you all do. Finally, I need to thank my "small" brown dog Willa, who has filled my days with happiness and reminds me to take care of myself and breathe. Thank you for always loving me no matter what.

ABSTRACT

HEMATOCRIT-CORRECTED DIFFUSE OPTICAL MONITORING OF BLOOD FLOW AND OXYGEN METABOLISM
DURING CARDIOPULMONARY BYPASS
Emilie Jan Benson

Arjun G. Yodh

Wesley B. Baker

This thesis addresses the need for continuous cerebral monitoring immediately after birth. For

at-risk populations, such tools potentially enable early detection of injury and possible interventions to

mitigate further neurological injury. More specifically, adverse neurological outcomes are common in

neonates with severe congenital heart defects following cardiac surgeries that employ cardiopulmonary

bypass (CPB). Since adequate oxygen delivery and metabolism are both critical for avoiding neurologic

injury, we have developed instrumentation to monitor cerebral impacts of CPB, and we have utilized this

instrumentation in animal model (swine) experiments which explore the use of mild hypothermic CPB

(MH-CPB) for neuroprotection (by decreasing metabolic demand).

Here we employ diffuse optics, specifically combined instrumentation based on diffuse optical

spectroscopy (DOS) and diffuse correlation spectroscopy (DCS), as a continuous, non-invasive and

portable means of measuring absolute blood oxygenation, oxygen extraction fraction, blood flow, and

oxygen metabolism in the brain during and after MH-CPB surgery. We applied these technologies to a pre-

clinical neonatal model of swine undergoing CPB. Notably, we concurrently obtained other metabolic

biomarkers from invasive cerebral microdialysis sampling, including metrics of metabolic distress (lactate-

pyruvate ratio) and injury (glycerol). Thus, the work provides comparison metrics for diffuse optics, and

the work teaches us about brain physiological response during mild hypothermic CPB.

The measurements were performed before, during, and after MH-CPB in a neonatal swine model

(n=28). Changes in cerebral physiology during and after MH-CPB were assessed using linear mixed effects

models. Importantly, profound changes in hematocrit during MH-CPB (*e.g.,* +54% variation from baseline) motivated the development and application of a hematocrit-corrected analysis for the optical measurements; we found that the hematocrit corrections led to reduced cerebral blood flow and oxygen metabolism values compared to predictions of the conventional analysis of diffuse optical data. We believe that this approach for hematocrit correction is important, because it could impact optical measurements in a plethora of medical procedures wherein hematocrit is likely to change, *e.g.,* blood transfusions, large loss of blood during surgery, or extracorporeal membrane oxygenation (ECMO).

Using this correction, and other standard diffuse optics analyses, we learned about brain physiology during and after MH-CPB. While no significant metabolic distress was detected during CPB, we did find that several parameters (*i.e.,* glycerol, StO$_2$) were significantly elevated 0 to 8 hours following MH-CPB and then started to resolve between 8 and 24 hours after CPB. Coupled with our pathology results, this finding suggests that a resolution in neurologic injury from CPB occurs around 8-12 hours post-CPB. Thus, more care may be needed for the first 8-12 hours.

We also found that amount of oxygen extracted from blood significantly increased during CPB, while blood flow and cerebral metabolism slightly decreased with increased duration on bypass. This finding could indicate that prolonged exposure to CPB can cause additional neurologic injury.

In addition to the hematocrit/MH-CPB studies, this thesis also addressed two weaknesses of the current generation of diffuse optical probes. The first advance developed/demonstrated a chassis coupling technique which improved reproducibility of any diffuse optical measurements that involved attachment and reattachment of the probe to the tissue surface. The second advance improved the capability of the probe to measure blood flow through hair, which is a major absorber of light that reduces signal-to-noise of brain measurements. This scheme placed fibers directly on the scalp, 'combing' the hair

out of the way; the work identified a path for additional improvements to improve patient comfort and

measurement fidelity in clinical settings.

Table of Contents

LIST OF TABLES

LIST OF FIGURES

<div align="center">**CHAPTER 1**</div>

<div align="center">**INTRODUCTION**</div>

There are few things as necessary for life as the human brain. Unfortunately, our ability to monitor the brain continuously and at the bedside is limited. This limitation is especially crucial for infants who are starting life with the vulnerabilities associated with congenital heart defects. Congenital heart defects (CHD), abnormalities in the structure of the heart, arise in approximately 13 per 1,000 live births and are among the most common types of birth defects [1]. Infants with severe CHD require surgery within the first few months of life to repair the defect. Moreover, even when the repair is successful, they are still at an increased risk of developmental disorder or developmental delay [2]. These facts highlight the need for continuous cerebral monitoring immediately after birth. Especially for the at-risk populations, such tools could enable earlier detection of injury and possible interventions that mitigate the risk of further neurological injury.

1.1 Monitoring with Diffuse Optical Spectroscopies

Diffuse optics, specifically diffuse correlation spectroscopy (DCS) and diffuse optical spectroscopy (DOS), have been demonstrated recently as a means to non-invasively monitor cerebral blood flow, oxygen saturation, and metabolism in vulnerable populations [3-5]. These optical techniques can fill a gap in the current standard of care. They provide capability to continuously, and noninvasively, monitor cerebral hemodynamics (without ionizing radiation) at the bedside. The diffuse optics techniques take advantage of an observation, made famous by Jöbsis in the 1977, that near-infrared (NIR) light within a large spectral window (650-950 nm) can penetrate tissue without significant absorption [6,7]. In the NIR window, the light absorption of the two main chromophores (light absorbers) in tissue, water and hemoglobin, is relatively low (Figure 1.1). The absorption of tissue is characterized by a wavelength-dependent absorption coefficient (μ_a), which is the rate of photon absorption in the medium per unit length traveled by the photon. In tissue, μ_a is on the order of 0.1 cm^{-1}. Its reciprocal is the mean absorption length in

<div align="center">1</div>

tissue: 10 cm; this means that a photon absorption event will be likely to occur within tissue after it has traveled about 10 cm. This lack of absorption enables experimenters to use NIR light to investigate tissues located several centimeters below the surface. Furthermore, although the overall NIR tissue absorption is low, the spectra of the dominant chromophores are distinct. Thus, if one can measure tissue absorption spectra, using multiple optical wavelengths, then one can in principle calculate the concentrations of oxy-(HbO_2) and deoxy-hemoglobin (Hb) in tissue. DOS measures tissue absorption at multiple wavelengths to gather this information about tissue chromophores. The details of how this is accomplished with be further discussed in Chapter 2, but it is loosely based on Beer's law (albeit with an effective pathlength that depends on tissue scattering).
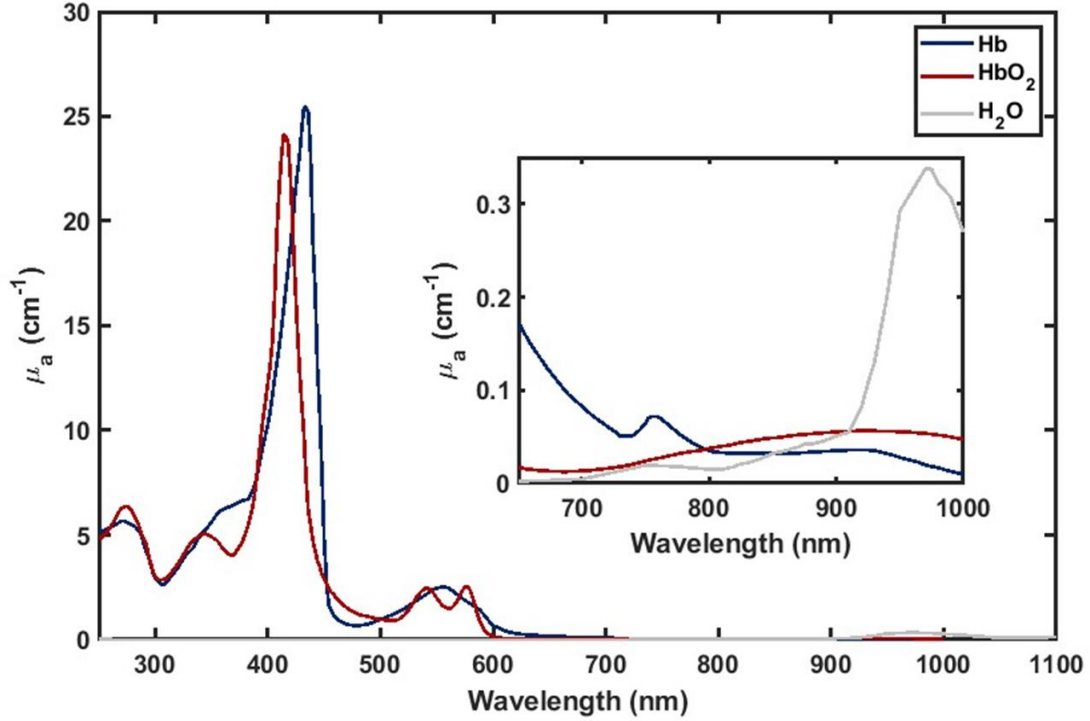
Figure 1.1 Absorption (μ_a) spectra of water, oxy- and deoxy- hemoglobin. The inset shows the

"physiological window" in the near-infrared range where absorption of water and hemoglobin is

relatively low. Since these are the main chromophores in tissue, light can penetrate several

centimeters into tissue in this wavelength range. The data for this figure is derived from work of

Scott Prahl assuming the tissue has a 20 µM concentration of Hb and HbO_2 and is 75% water

[8,9].

While absorption by tissue is relatively low in the NIR region, tissue scattering is high. The

analogous scattering coefficient (μ_s) represents a rate of photon scattering in the medium per unit length

traveled by the photon. In tissue, μ_s is on the order of 100 cm^{-1}, making it about 1000 times more likely

for a scattering event to occur than an absorption event. The so-called reduced scattering coefficient,

denoted as μ_s', is often used instead of the scattering coefficient given in the photon diffusion regime. μ_s'

relates more directly than μ_s to the diffusion of photons. The reciprocal of the reduced scattering

coefficient ($1/\mu_s'$) is the photon random walk step in the medium; the photon random walk step is the

distance a photon travels in the medium (on average) before its direction is randomized. The reduced scattering coefficient thus accounts for the fact that typical photon scattering events are biased towards the forward direction.

Photons transport in deep tissues is characterized by many, many scattering events; the photons transport is in the high, multiple scattering limit. In this limit, light propagation is well approximated as a diffusive process (more on this in Chapter 2) [10]. Figure 1.2 depicts a single source-detector pair for the most basic diffuse optical cerebral measurement. The NIR light passes through the scalp and skull, and then diffuses through brain tissue; a very small fraction of the input photons will eventually reach the detector. Using these detected photons, we probe a "banana shape" region with a depth approximately half the source-detector separation on the surface (in this case, ≈1.5cm for a source-detector separation of 3cm); the detected photons predominantly "interact" with tissue in the banana-shaped region shown in the figure. In this situation, typical photons travel through approximately 90 cm in the tissue before emerging in the typical reflectance geometry experiment shown in Figure 1.2 [11].
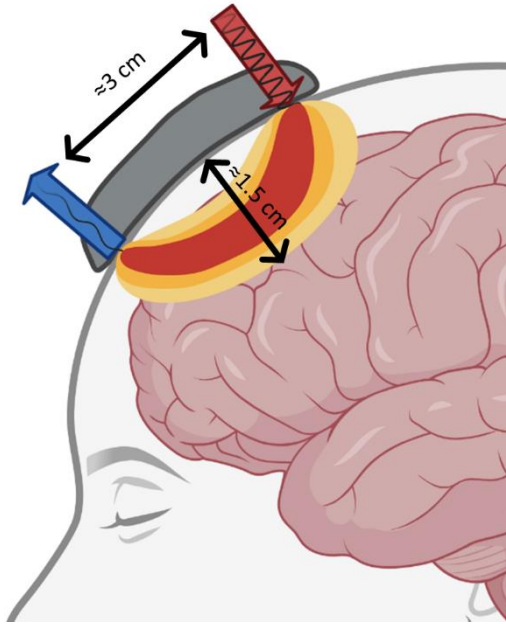
Figure 1.2 A single source-detector pair in the reflectance geometry used for brain tissue measurements.

So far, we have described the DOS technique. The DCS technique has the same light penetration issues as DOS, but DCS measures light intensity temporal fluctuations (rather than light absorption changes via light transmission) on comparatively short timescales (microseconds). These light fluctuations are due to movement of red blood cells in the vasculature. DCS measures a blood flow index (BFI) which is obtained from the decay of the temporal intensity autocorrelation function (further discussed in Section 2.6). Typically, both DOS and DCS measurements employ the same experimental geometry in our brain studies. Thus, a single probe-head with multiple optical fibers can be employed to make DOS and DCS measurements simultaneously. DOS, the "static" technique, measures variations in μ_a and μ_s to derive tissue chromophore concentrations. DCS measures light intensity fluctuations to derive tissue blood flow.

These diffuse optical techniques have great potential for use in clinical settings. They enable measurement of tissue blood oxygenation, blood flow and oxygen metabolism, all noninvasively. However, while these techniques have been used in a variety of research settings ranging from breast imaging to neuromonitoring, they have not yet been established as a standard of care.

1.2 Other Metrics of Metabolism and Neurologic Injury

Several other techniques are currently used in pre-clinical studies to monitor neurologic injury and cerebral metabolism. These techniques, including microdialysis, respirometry, and pathology, will be discussed in Chapter 4 (along with a few other physiological metrics). These measurements are typically invasive, and in some instances the measurements can only be performed after euthanasia of the subject. Of course, this limits their usefulness in the clinical space. However, in the pre-clinical space, they can be extremely useful. For example, we can compare results of the diffuse optical measurements to these invasive metrics for validation, thereby validating the non-invasive optical metrics for future clinical space monitoring.

A major focus of my research is oxygen metabolism. My optics research entailed concurrent use of a clinically accepted metrics of metabolism for comparison to optics. To this end, I employed microdiaylsis; microdialysis provides specific and quantitative information about cerebral metabolism but is collected at several time points (rather than continuously) throughout the surgical/post-surgery procedure. The comparison to microdialysis represents a major improvement for comparison to optics metrics; for example, pathology parameters are only obtained at a single timepoint at euthanasia.

1.3 Contributions to the Field

1.3.1 Cardiopulmonary Bypass Measurements

At the beginning of this chapter, I outlined the clinical need for cerebral monitoring in infants with CHD. These infants often have corrective heart surgery, requiring the use of cardiopulmonary bypass (CPB). CPB is a form of extracorporeal membrane support, meaning that it provides oxygen and blood flow to the body while the heart is being operated on. These procedures can be long and are known to result in neurological injury. I chose to examine the cerebral hemodynamic time course during these procedures to help elucidate when and what could be the cause of neurologic injury.

My work centered on two different models of mild-hypothermic cardiopulmonary bypass (MH-CPB): one examined effects for the duration of MH-CPB, and the other focused on trends during and up to 24 hours post MH-CPB. Both of these studies were completed in a neonatal swine model, allowing for much more control than in clinical studies. The first study was able to thoroughly examine the impacts of one, two, three, or four hours of MH-CPB support; this enabled us to explore how, why, and when injury is occurring during CPB [12]. The second study focused on different survival times post-MH-CPB.

We focused on MH-CPB models in order to examine the efficacy of mild hypothermia (*e.g.,* compared to deep hypothermia) per reducing metabolic demand and slowing inflammatory responses; many open questions remain regarding optimal temperature management during CPB procedures [13-15]. Recently, the clinical use of mild hypothermic CPB (MH-CPB) (34°C), instead of deep hypothermia (18°C), has grown because MH-CPB requires less time on CPB, thus potentially reducing risks of injury [16]. Our studies were set up to test the impact of the duration of MH-CPB on cerebral health as well as to monitor the time course for potential injuries during MH-CPB.

Per results, even though MH-CPB is thought to reduce metabolic demand, we did not observe a significant reduction in metabolism at the start of MH-CPB, signifying that this may not be as protective as deep hypothermia. Both blood flow and metabolism decreased with time on MH-CPB, while the fraction of oxygen extracted increased. This finding indicates a growing imbalance between oxygen delivery and demand with increasing time on CPB, suggesting that prolonged CPB duration is a risk factor for neurological injury.

I also studied the acute survival period after coming off MH-CPB to further characterize the time course for potential injury. I carried out a sensitivity analysis (see Section 6.4.2) which found a return to baseline around eight hours post decannulation from the CPB circuit. This finding is consistent with a

trending peak likelihood of organ dysfunction around 9-12 hours post-CPB and stabilization around 24-hours post-CPB, which has been observed clinically [17-20].

1.3.2 Hematocrit Correction

In the process of analyzing these measurements, I discovered the importance of an effect that often arises during CPB. In particular, the hemoglobin concentrations are often increased in the blood during bypass. These very large increases in hemoglobin affect both DOS and DCS measurements. Notably, they can have a very strong effect that has not been clinically accounted for on the DCS blood flow measurement [21]. While the idea that large changes in hemoglobin concentration can impact DCS measurements is known, such corrections have not been applied in any *in vivo* studies [22,23]. Especially, since hemoconcentration (hemofiltration to remove excess fluids thus increasing hemoglobin concentration) occurs during CPB procedures, the changes in hemoglobin concentrations swing drastically. My work showed that these swings are critical to include in the analysis. My work during CPB is the first application of a hematocrit correction in an *in vivo* study. It showed how (and under what circumstances) future studies must be performed to account for this important issue.

1.3.3 Instrumentation Developments

My work was primarily focused on the applications of diffuse optics to CPB. However, to keep the instrumentation operational and to improve the measurements, I developed calibration technology for our diffuse optics instrumentation. I identified an optimal regime for device calibration, and I worked to calibrate these instruments "in vitro" at the bench.

Additionally, I worked to modify the optical probes so that they work better on the scalp and through hair-covered regions of the head. I mentored an undergraduate student in the lab whose primary focus was on the creation and validation of a probe that would fit into a chassis that could be securely fixed to the scalp. This allowed for easier attachment and detachment of the optical probe. I also worked

on re-engineering the optical probe layout, because our current instrumentation now includes an additional broadband diffuse optics system that requires more optical fibers in the optical probe. Finally, I worked on creating a DCS-only optical probe that improved our ability to measure tissue blood flow through hair covered regions of the head. This required a new style of probe that averts the hair follicle regions that attenuate light differently compared to non-hair covered regions (like the forehead).

All of these technical contributions advanced our ability to measure the brain in more diverse settings and for a broader range of applications.

1.4 Summary and Thesis Organization

Neonates with CHD are at an increased risk of developing neurological deficits. As mentioned above, diffuse optics provides a novel means to monitor cerebral hemodynamics that potentially enables us to elucidate the timing and causes of this injury.

Chapter 2 focuses on the diffuse optics theory, and Chapter 3 describes the instrumentation for FD-DOS (frequency-domain DOS) and DCS respectively. In Chapter 4, I discuss other metrics that I used to examine effects of CPB, focusing on the biology and physiology of these techniques and how they relate to our optical measurements. Chapter 5 describes the statistical analyses needed to examine changes at the onset of MH-CPB, trends over time during these procedures, as well as comparison of the optical data to other clinical standards. Chapter 6 is the heart of the thesis; it provides the details for several experiments conducted on swine models for CPB. This chapter digs deeply into the protocols used and discusses the publications will result from the primary study. Finally, Chapter 7 provides an overview of the optical probes that I developed to improve diffuse optical measurements, and Chapter 8 summarizes the work and briefly discusses the future.

CHAPTER 2

THEORIES UNDERLYING DIFFUSE OPTICAL TECHNIQUES

Diffuse optical techniques monitor tissue in the near-infrared (NIR) range due to the fact that tissue absorption in this spectral region is low. Many different diffuse optical methods are used, including: diffuse optical spectroscopy (DOS), broadband diffuse optical spectroscopy (bDOS), diffuse optical tomography (DOT), and diffuse correlation spectroscopy (DCS). My measurements employ DOS and DCS. I will therefore only discuss these two techniques at length. I will focus on DOS first, since DCS is more subtle, and since DCS also relies on the scattering and absorption coefficients obtained from DOS for the most accurate measurements.

The intent of this chapter is to introduce the basic theory needed to understand my measurements. Note, the chapter liberally uses the theory developed in subsections of *Biomedical Optics: Principles and Imaging* by Wang and Wu [24], in previous theses from my lab [25-29], and in review papers [30]. None of my work would have been possible without work previously completed by others ("if I have seen further than others, it is by standing on the shoulders of giants." -Isaac Newton).

2.1 Diffuse Optical Spectroscopy

Diffuse optical spectroscopy (DOS), which is also called Near-Infrared Spectroscopy (NIRS), relies on near-infrared light to noninvasively probe the optical properties of the tissue. When NIR light propagates through the tissue, it interacts with the tissue through two fundamental processes: absorption and scattering. An absorption event happens when light interacts with matter (atoms/molecules); the interaction excites an electron of the atom/molecule from the ground state into an excited state. When these electrons relax back to the ground state, the atom/molecule typically gives off a photon (*e.g.,* a photon with energy less than the excitation photon in a random direction) or the atom/molecule relaxes

non-radiatively (*e.g.,* it gives off "heat"). The absorption process thus serves to irretrievably remove input light from tissue, decreasing the amount of light that makes it to the detector.

Photon scattering happens in one of two forms: elastic or inelastic scattering. As in classical mechanics, elastic scattering involves no energy transfer, while inelastic scattering requires exchange of energy between the photon and the atom/molecule. In elastic (Raleigh or Mie) scattering, photon energy in conserved, but the momentum (which is directional) is not necessarily conserved. In tissue, elastic scattering is a dominant interaction effect in the near-infrared region.

DOS utilizes near-infrared light to measure absorption and scattering properties of tissue. An optical probe containing optical fibers is used to couple source NIR light to a point (or point-like region) on the scalp surface; another optical fiber, embedded in the same optical probe, is employed to collect a component (part of) the light "reflectance" emerging from the tissue surface some distance away from the source fiber, and this collected light is then coupled to a photon detector. The photon path distribution in the tissue has the typical "banana shape" the gives an approximate volume of tissue that is probed by the source-detector configuration (Figure 1.2) [30]. Depending on source-detector separation, the mean tissue depth that is probed by the "banana" can range from a few millimeters to several centimeters below the scalp surface [31]. The precise depth and attenuation of light through the tissue is dependent on the optical setup as well as both the absorption and scattering properties of the tissue, but it is approximately 1/3 to 1/2 of the source-detector separation for typical tissues; note, the width of the depth distribution is roughly equal to the penetration depth. In order to separate the effects of scattering from those of absorption using this diffusing light, a quantitative model of light transport is required.

The diffusion model provides a way to separate the scattering and absorption events by approximating that light travels over long distances in tissue as a diffusive process. Below, I provide some

details about how the diffusive light transport model is obtained from the more general radiative transport theory.

2.2 Radiative Transport Theory

Radiative transport theory is the starting point for most diffuse optics derivations. In tissue, radiative transport theory is a good approximation for approaches based fully on Maxwell's equations. It is roughly equivalent to using a numerical Monte Carlo method to calculate photon trajectories, which can be computationally inefficient. The radiative transport equation (RTE) is derived using the principles of conservation of energy, but neglecting the influence of coherence, polarization (or averaging over all possible light polarizations), and optical nonlinearities.

Several assumptions are made to arrive at the radiative transfer equation (RTE). First, as noted above, it is assumed that interference of electric fields of different multiple scattering paths is negligible (on average). Secondly, the source is assumed monochromatic. Third, the scattering particles are independent and non-interacting. Fourth, the far-field approximation is used, which essentially assumes that the distance between scattering events is much larger than the wavelength of incident light.

Transport theory is based on the behavior of light radiance ($L(\vec{r}, \widehat{\Omega}, t)$, [Wcm^{-2}sr^{-1}]). The radiance is defined as the light power per unit area per solid angle traveling in the $\widehat{\Omega}$ direction at position $\vec{r}$ and time t; it is given for a specific wavelength of light, λ, and thus specific tissue index of refraction (n). The amount of radiant power, $W(\widehat{\Omega})$ [W], which is transported through an element of area dA (at position $\vec{r}$ and time t) in the direction $\widehat{\Omega}$ with angular "width" $d\Omega$ (Figure 2.1) is given by,

$$W(\widehat{\Omega}) = Lcos\theta dAd\Omega .$$

(2.1)

Here θ is the angle between $\widehat{\Omega}$ and the area element normal vector, n̂. The fluence rate (or intensity) Φ (Wm^{-2}) represents the energy flow per unit area per unit time flowing radially outward from the volume element; it is defined in terms of the radiance integrated over the entire 4π solid angle as:

$$\Phi(\vec{r}, t) = \int_{4\pi} L(\vec{r}, \widehat{\Omega}, t) d\Omega .$$

(2.2)
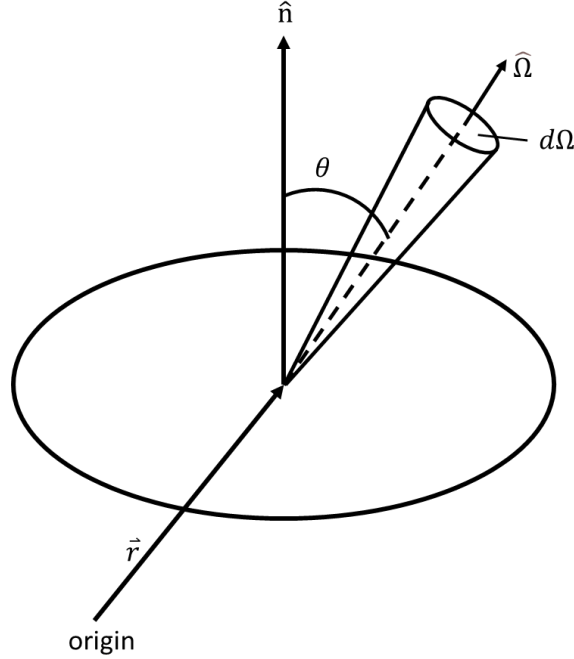
Figure 2.1 Schematic of energy flow within a differential solid angle element $d\Omega$.

We define N_s as the number density of the scatterers which can in principle depend on position and time; $N_s dV$ denotes the number of scatters in the volume element. We also define σ_s as the total elastic scattering cross section of a scatterer. Thus, we can now introduce the scattering coefficient: $\mu_s = N_s \sigma_s$. Note that $1/\mu_s$ is the mean distance a photon travels between scattering events. Similarly, tissue absorption is characterized by an absorption coefficient, μ_a, whose inverse, $1/\mu_a$, is the mean distance photons travel before they are absorbed (μ_a depends on the concentrations of absorbing chromophores in tissue, as described below). The total transport coefficient, $\mu_t = \mu_a + \mu_s$, is the rate of radiance (photon) "extinction" due to both absorption and scattering in the volume element.

The radiative transport equation (RTE; sometimes also called the Boltzmann equation) is a conservation equation for radiance in the volume element:

13

$$\frac{\partial L(\vec{r}, \widehat{\Omega}, t)/v}{\partial t} = -\widehat{\Omega} \cdot \nabla L(\vec{r}, \widehat{\Omega}, t) - \mu_t L(\vec{r}, \widehat{\Omega}, t) + \mu_s \left[\int_{4\pi} L(\vec{r}, \widehat{\Omega}, t) P(\widehat{\Omega}', \widehat{\Omega}) d\widehat{\Omega}' \right] + Q(\vec{r}, \widehat{\Omega}, t). \quad (2.3)$$

$Q(\vec{r}, \widehat{\Omega}, t)$ is the contribution from sources in the volume element that has units of [Wm⁻³sr⁻¹]; and

$P(\widehat{\Omega}', \widehat{\Omega})$ is the phase function representing the probability that light with propagation direction $\widehat{\Omega}'$ is

scattered into $\widehat{\Omega}d\Omega$.

Before proceeding, an additional variable of importance for describing light transport through

tissue is the scattering anisotropy term, which is defined as $g \equiv \langle cos\theta \rangle$. A value of zero for the scattering

anisotropy indicates that a typical elastic scattering event scatters light isotropically; a value close to unity

indicates that a typical elastic scattering event scatters light dominantly in the forward direction. The

scattering is defined by the following integral:

$$g = \int_{4\pi} (\widehat{\Omega}' \cdot \widehat{\Omega}) P(\widehat{\Omega}' \cdot \widehat{\Omega}) d\Omega. \quad (2.4)$$

Note that $P(\widehat{\Omega}', \widehat{\Omega})$ satisfies $\int_{4\pi} P(\widehat{\Omega}', \widehat{\Omega}) d\Omega = 1.$ In typical tissue samples, g ranges from 0.8-0.98 [32].

2.3 Diffusion Theory

The RTE is difficult to solve analytically except for very simple, highly symmetric geometries, in part

because there are six independent variables to account for. For highly scattering tissues (high albedo,

$\mu_a \ll \mu_s$) the RTE can be greatly simplified using what is commonly known as the diffusion approximation.

This means that the scattering medium is nearly isotropic after sufficient scattering. To make this

approximation, we expand $L(\vec{r}, \widehat{\Omega}, t)$ in terms of the spherical harmonics Y_ℓ^m (with coefficients $\phi_{\ell,m}$) up

to terms with $\ell = 1$ (known as the P₁ approximation). The radiance can then be written as [24,30]:

$$L(\vec{r}, \widehat{\Omega}, t) = \frac{1}{4\pi} \Phi(\vec{r}, t) + \frac{3}{4\pi} \vec{J}(\vec{r}, t) \cdot \widehat{\Omega} \quad (2.5)$$

with the photon fluence, $\Phi(\vec{r}, t)$, is defined by Equation (2.2), and the photon flux, $\vec{J}(\vec{r}, t)$ (W/cm²), is

defined as

$$\vec{J}(\vec{r},t) \equiv \int_{4\pi} L(\vec{r},\widehat{\Omega},t)\,\widehat{\Omega}d\Omega = \frac{1}{\sqrt{2}}(\phi_{1,-1} - \phi_{1,1})\hat{x} - \frac{i}{\sqrt{2}}(\phi_{1,-1} + \phi_{1,1})\hat{y} + \phi_{1,0}\hat{z} \qquad (2.6)$$

We can then relate $\vec{J}(\vec{r},t)$ to $\Phi(\vec{r},t)$ through integrating Eq. (2.3) over all solid angles to get:

$$\frac{1}{v}\frac{\partial\Phi(\vec{r},t)}{\partial t} + \nabla \cdot \vec{J}(\vec{r},t) + \mu_a\Phi(\vec{r},t) = S(\vec{r},t)\,. \qquad (2.7)$$

$S(\vec{r},t)$ (W/cm³) is the total power per volume emitted outward from $\vec{r}$ at time t ($S(\vec{r},t) \equiv \int_{4\pi} Q(\vec{r},\widehat{\Omega},t)d\Omega$). Another relationship between $\vec{J}(\vec{r},t)$ and $\Phi(\vec{r},t)$ can be obtained by substituting (2.5) into Eq (2.4). We then multiply by $\widehat{\Omega}$ and integrate over all solid angles, producing

$$\nabla\Phi(\vec{r},t) = -\frac{3}{v}\frac{\partial\vec{J}(\vec{r},t)}{\partial t} - 3\mu_t\vec{J}(\vec{r},t) + 3\int Q(\vec{r},\widehat{\Omega},t)\widehat{\Omega}d\Omega + 3\mu_s g\vec{J}(\vec{r},t) \qquad (2.8)$$

If the source is isotropic, *i.e.,* $Q(\vec{r},\widehat{\Omega},t) = Q(\vec{r},t)$, then the integral over Q in Eq. (2.8) is zero. If we also assume slow temporal variations in $\vec{J}(\vec{r},t)$, then the $\partial\vec{J}(\vec{r},t)/\partial t$ term in Eq (2.8) can be neglected. These assumptions simplify Eq. (2.8) to Fick's law of diffusion for photons:

$$\nabla\Phi(\vec{r},t) = -3(\mu_s' + \mu_a)\vec{J}(\vec{r},t) \qquad (2.9)$$

where $\mu_s' \equiv (1-g)\mu_s$ and is called the reduced scattering coefficient.

We can now get the photon diffusion equation for the photon fluence rate by substituting (2.9)(2.18) into (2.7) yielding:

$$\nabla \cdot (D(\vec{r})\nabla\Phi(\vec{r},t) - v\mu_a(\vec{r})\Phi(\vec{r},t) - \frac{\partial\Phi(\vec{r},t)}{\partial t} = -vS(\vec{r},t)\,. \qquad (2.10)$$

$D(\vec{r}) \equiv v/3(\mu_s'(\vec{r}) + \mu_a(\vec{r}))$ is called the photon diffusion coefficient.

Qualitatively, the photon diffusion equation describes a distribution of photons (proportional to the photon concentration in space-time). Each photon moves along a random walk trajectory. In the random walk trajectory, photons move in a straight line until the direction is randomly changed by a scattering event (or the photon is absorbed). The average length that the photon travels before

15

encountering such a direction-randomizing scattering event is called the transport mean free path length, ℓ_{tr}, which is approximately equal to $1/\mu_s'$.

To summarize the approximations, the photon diffusion is valid when the following assumptions hold:

1. RTE is valid.

2. The P₁ approximation is valid. This requires that the light radiance is nearly isotropic ($\Phi \gg |\vec{J}|$), which is typically true when $\mu_s' \gg \mu_a$ and when propagation distances for "measurements" are large compared to ℓ_{tr}. Otherwise, approximations beyond the P₁ are needed.

3. The source is isotropic.

4. The temporal photon flux variations are comparatively slow, i.e., $\frac{v\mu_s'}{\omega} \gg 1$. Where ω is the sinusoidally modulated source frequency.

5. μ_a, μ_s and P are all independent of propagation direction (rotational symmetry).

For biological tissues, all of these assumptions are generally valid in the near-infrared region [30].

2.3.1 Diffuse Photon Density Waves

The work that I present here uses Frequency Domain DOS (FD-DOS). In FD-DOS the source light is intensity modulated, i.e., sinusoidally modulated at frequency ω. This type of source produces a diffusive wave (diffuse photon density wave) in the medium that oscillates in time at the same frequency as the source. The intensity amplitude and phase information are measured by detectors and are used to calculate μ_a and D. The basic principle of this method can be seen in Figure 2.2. In this method, a point source is located at r_s, the source term can be represented by

$$S(\vec{r}, t) = S_{DC}(\vec{r})\, \delta(\vec{r} - r_s) + S_{AC}(\vec{r})e^{i\omega t}\, \delta(\vec{r} - r_s)$$

(2.11)

with S_{DC} as the DC and S_{AC} as the AC components of the source and $\delta(\vec{r} - r_s)$ as the three-dimensional Dirac delta function. The fluence rate (due to this source) in the medium is correspondingly expressed as:

16

$$\Phi(\vec{r}, t) \equiv \Phi_{DC}(\vec{r}) + \Phi_{AC}(\vec{r}) = \Phi_{DC}(\vec{r}) + U(\vec{r})e^{i\omega t} \qquad (2.12)$$
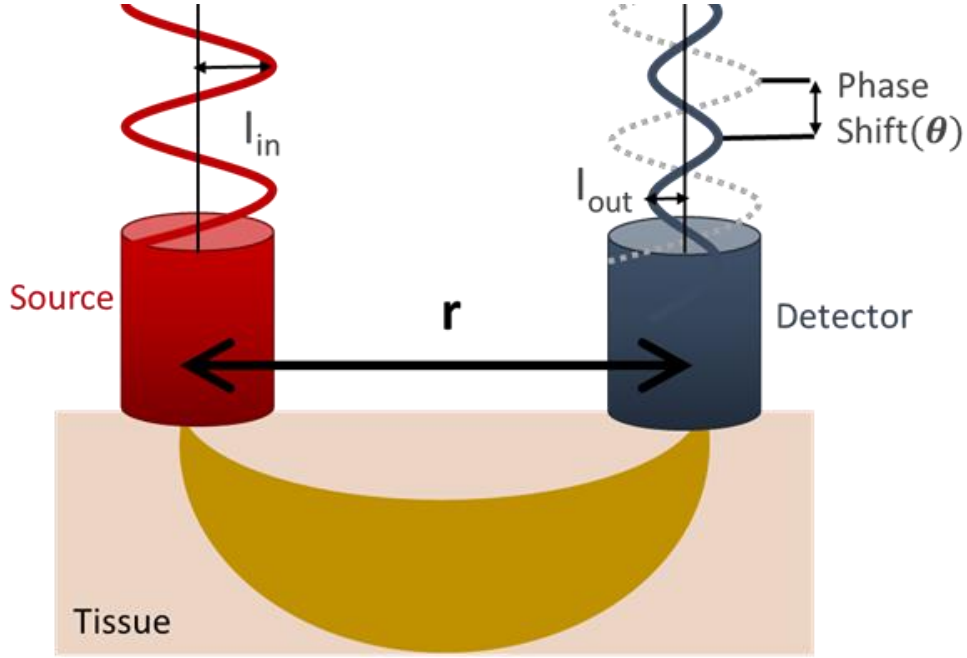
Figure 2.2 Schematic of FD-DOS in reflectance geometry. Light from a source passes through tissue and is attenuated. The measured light thus has a decrease in intensity and a phase shift due to particle interactions within the tissue.

Substituting the AC component (Φ_{AC}) into the photon diffusion equation yields:

$$\nabla \cdot (D(\vec{r})\nabla U(\vec{r})) - (v\mu_a(\vec{r}) - i\omega)U(\vec{r}) = -vS_{AC} \qquad (2.13)$$

For homogenous media, this can be rewritten in Helmholtz equation form to obtain:

$$(\nabla^2 + k^2)U(\vec{r}) = -\frac{v}{D}S_{AC}(\vec{r}) \qquad (2.14)$$

with $k^2 = (i\omega - v\mu_a)/D$.

For an infinite, homogenous medium with a single point source at the origin which is intensity modulated $(S_{AC}(\vec{r} = S_{AC}\delta(\vec{r}))$, the solution is well known. The main boundary condition is that the fluence rate falls to zero at infinity and Eq. (2.14) is solved to give:

$$U(\vec{r}) = \frac{vS_{AC}}{4\pi D} \frac{e^{ikr}}{r} \tag{2.15}$$

where $k = k_r + ik_i = \sqrt{(i\omega - v\mu_a)/D}$ is the complex (scalar) wave vector and $r = |\vec{r}|$ is the distance between the light source and detector [33]. This solution describes an overdamped spherical wave radiating outward from the point source. The real and imaginary components of the wavevector can be expressed as:

$$k_r = \sqrt{\frac{v\mu_a}{2D}} \left[\sqrt{1 + \left(\frac{\omega}{v\mu_a}\right)^2} - 1 \right]^{1/2} \tag{2.16}$$

$$k_i = \sqrt{\frac{v\mu_a}{2D}} \left[\sqrt{1 + \left(\frac{\omega}{v\mu_a}\right)^2} + 1 \right]^{1/2} \tag{2.17}$$

From writing the fluence rate in the form of $U(\vec{r}) = Ae^{i\theta}$ we can use these equations to calculate μ_a and μ_s from measurements of A and θ at known source-detector separations.

2.4 Semi-Infinite Geometry

Tissue is commonly approximated by a semi-infinite medium (Figure 2.3) for most real-world biomedical applications. In this model, the source and detector fibers are placed on the surface of tissue at the boundary of a non-scattering medium (e.g., air) and a diffusive medium (e.g., tissue), imposing boundary conditions on the photon propagation at the interface of the two media.
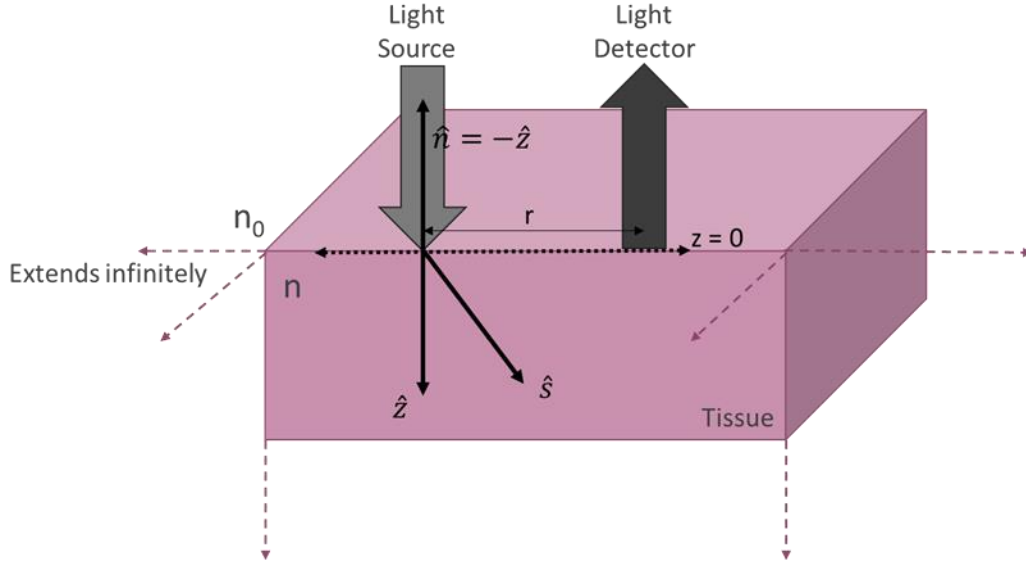
Figure 2.3 Semi-infinite geometry of a homogenous medium.

Since the tissue is highly scattering and the air is non-scattering, once the light exits the tissue into the non-scattering medium, it can be well approximated that the light will never return to the tissue. This total inward radiance at the boundary can be expressed as the integral of the reflected radiance and is due to Fresnel reflections of the radiance in the diffuse medium [34]:

$$E_{in} = \int_0^{2\pi} \int_{\pi/2}^{\pi} R_{Fresnel}(\hat{s})L(\hat{s}) \cdot \hat{n} \sin\theta \, d\theta \, d\phi \qquad (2.18)$$

E_{in} is the total incoming diffuse radiance (total light power per area traveling into the diffusive medium at the interface) and $R_{Fresnel}$ is the Fresnel reflection coefficient and defined as

$$R_{Fresnel}(\theta) = \begin{cases} \frac{1}{2}\left(\frac{n\cos\theta' - n_0\cos\theta}{n\cos\theta' + n_0\cos\theta}\right)^{1/2} + \frac{1}{2}\left(\frac{n\cos\theta - n_0\cos\theta'}{n\cos\theta + n_0\cos\theta'}\right)^{1/2} & 0 < \theta < \theta_c \\ 0 & \theta_c < \theta < \pi/2 \end{cases} \qquad (2.19)$$

where θ' is the refracted angle; θ is the angle of incidence; and θ_c is the critical angle. When this equation is evaluated using the nearly isotropic radiance for the inward radiance we get the partial-flux boundary condition of [34]:

$$\phi = \frac{1 + R_j}{1 - R_\phi}(-2j_z) \qquad (2.20)$$

19

where j_z is the magnitude of the photon flux in the $\hat{z}$ direction and

$$R_\Phi \equiv \int_0^{\pi/2} 2sin\theta cos\theta R_{Fresnel}(\theta)d\theta \; ; \tag{2.21}$$

$$R_j \equiv \int_0^{\pi/2} 3sin\theta \, cos^2 \, \theta \, R_{Fresnel}(\theta)d\theta. \tag{2.22}$$

At the tissue surface, where $z = 0$, the partial-flux boundary condition becomes:

$$\phi = 2D \frac{1 + R_{eff}}{1 - R_{eff}} \frac{d\phi}{dz} \tag{2.23}$$

where $R_{eff} = (R_\phi + R_j)/(2 - R_\phi + R_j)$ and is the effective reflection coefficient to account for the mismatch in index of refraction between tissue and air.

The partial-flux boundary condition is an exact solution; however, it is difficult to use in practice. Instead, we can use a simpler boundary condition where we approximate with the extrapolated-zero boundary condition. Here the fluence rate falls to zero at a point z_b outside of the tissue (on the air side of the boundary) as seen in Figure 2.4, written as

$$\Phi(z = -z_b) = 0 \tag{2.24}$$

with $z_b = -\frac{2}{3\mu_s'}$ [34]. This approximates the exact partial=flux boundary condition well [34,35].
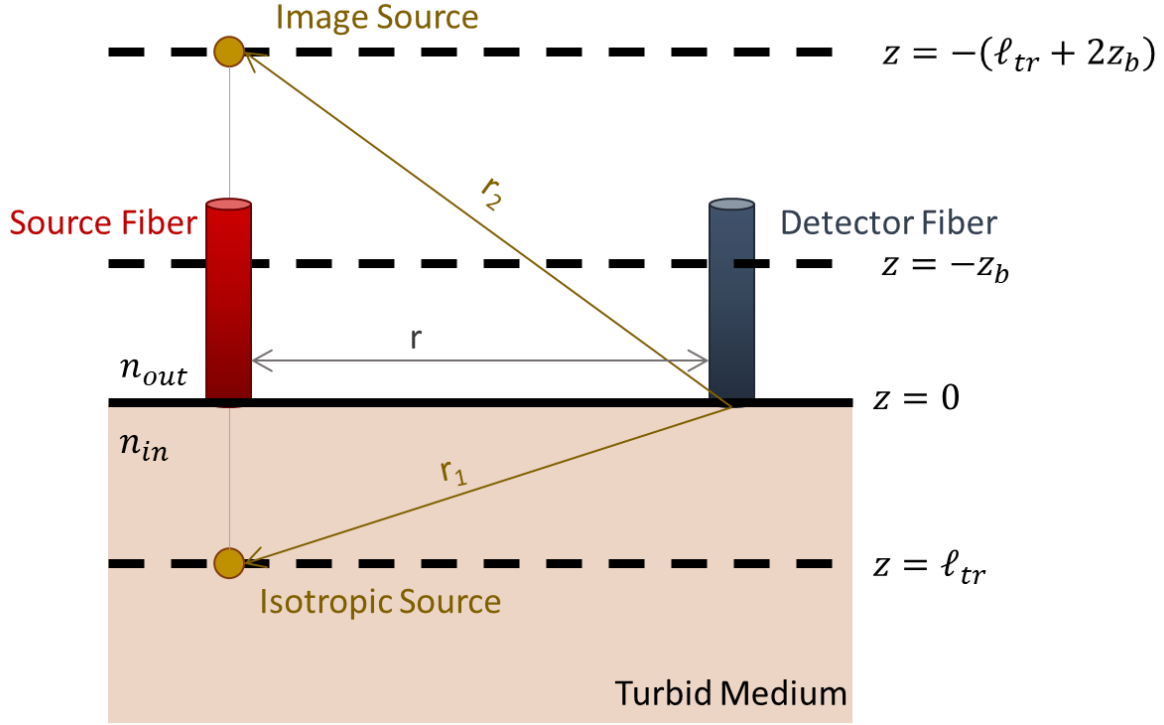
Figure 2.4. A diagram for the extrapolated boundary condition in the semi-infinite geometry.

The method of images can be employed to solve the diffusion equation with the extrapolated-zero boundary condition [30,36]. As shown in Figure 2.4, the extrapolated-zero boundary condition can be met with a negative image point source at $z_s = -2z_b + \ell_{tr}$ for a source at $z_b = \ell_{tr}$. Thus, the diffusion equation solution is

$$\Phi(\vec{r}) = \frac{vS_{AC}}{4\pi D} \left[\frac{e^{ikr_1}}{r_1} - \frac{e^{ikr_2}}{r_2} \right] \tag{2.25}$$

where $r_1 = \sqrt{r^2 + (z - \ell_{tr})^2}$ and $\sqrt{r^2 + (z - \ell_{tr})^2}$. For a large enough source detector separation ($r = |\vec{r}| \gg \ell_{tr}$), this can be simplified to:

$$\Phi(\vec{r}) = \frac{vS_{AC}}{4\pi D} \frac{e^{-kr}}{r^2} \left[2k(\ell_{tr}z_b + z_b^2) \right] = A(r)e^{i\theta(r)} \tag{2.26}$$

with $A(r)$ as the amplitude and $\theta(r)$ as the phase of the detected light [37,38]. From this equation, we can get two linear relationships:

$$\ln(A(\vec{r})r^2) = -k_i r + A_0 \tag{2.27}$$

$$\theta(\vec{r}) = k_r r + \theta_0 \tag{2.28}$$

with k_i and k_r properties of the medium defined in Eqs. (2.16) and (2.17). The slope from Eq. (2.27) gives $-k_i$ and the slope from Eq. (2.28) gives k_r. Thus, k_i and k_r can be extracted from measurements of amplitude and phase at multiple source detector separations (e.g., Figure 2.5), from which the tissue optical properties can be derived:

$$\mu_a = \frac{\pi f}{v}\left(\frac{k_i}{k_r} - \frac{k_r}{k_i}\right) \tag{2.29}$$

$$\mu_s' = \left(\frac{v}{3\pi f}\right)k_r k_i \tag{2.30}$$

with f as the modulation frequency of the source and v as the speed of light in tissue.

$$\ln(A(\vec{r})r^2) = -k_i r + A_0$$

$$\theta(\vec{r}) = k_r r + \theta_0$$

Source-Detector Separation, r (cm)
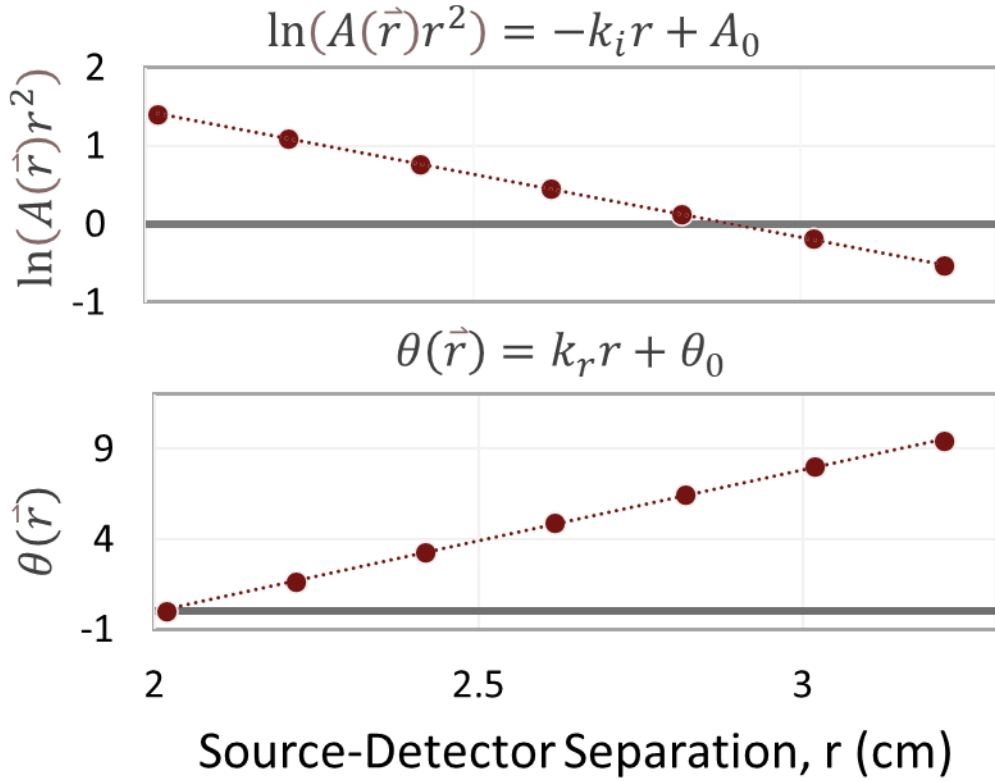
Figure 2.5 Linear relationships to calculate k_i and k_r. This data was collected and discussed in Section 3.3.2.

2.5 Calculation of Physiological Parameters

The absorption in tissue is linearly dependent on the concentrations of each chromophore present, i.e.,

$$\mu_a(\lambda) = \sum_i \varepsilon_i(\lambda)c_i \tag{2.31}$$

where ε_i is the wavelength-dependent extinction coefficient for the ith chromophore and c_i is the concentration. Using the equations developed in the previous section, I calculated the scattering and absorption properties of the tissue for each wavelength separately. I then generated a system of equations that relates the multispectral measurements of tissue absorption to the chromophore concentrations (i.e., Equation 2.31; one equation for each wavelength).

23

I will be employing FD-DOS to measure oxygenated and deoxygenated hemoglobin; thus, I need at least two wavelengths, although in practice I use three to four wavelengths (690, 725, 785, and 830 nm; 785 was often filtered out due to cross contamination with another optical technique) to improve accuracy. Water is also a chromophore in the brain, and while I do not measure water, I assume the brain is 75% water [39]. Note, water has relatively low absorption in the NIR range compared to oxy- and deoxyhemoglobin. The extinction coefficients for water, oxy- and deoxyhemoglobin have all been previously reported [8,39]. Once the concentration of oxy- and deoxyhemoglobin ([HbO$_2$] and [Hb] respectfully) have been calculated, the total hemoglobin concentration (THC) and tissue oxygen saturation (StO$_2$) can be determined:

$$THC = [Hb] + [HbO_2]$$
(2.32)

$$StO_2(\%) = \frac{[HbO_2]}{[Hb] + [HbO_2]}$$
(2.33)

2.5.1 Oxygen Extraction Fraction (OEF)

We can also get an optical measurement of metabolism by looking at the oxygen extraction fraction (OEF). This is the fraction of oxygen that is being extracted by the tissue for metabolism; it is represented as:

$$OEF = \frac{CaO_2 - CvO_2}{CaO_2} \approx \frac{SaO_2 - SvO_2}{SaO_2}$$
(2.34)

where CaO_2 is the "input" arterial oxygen concentration (units of: mLO$_2$/dL), CvO_2 is the "output" venous oxygen concentration, SaO_2 is the arterial oxygen saturation (% hemoglobin carrying oxygen), and SvO_2 is the venous oxygen saturation. The approximation using oxygen saturation instead of oxygen concentration is a good when hemoglobin concentration and dissolved oxygen in the blood remain fairly constant. This assumption can break down during the cardiopulmonary bypass studies because the amount of hemoglobin and dissolved oxygen are both significant (this will be further discussed in Section 4.3).

If we assume the fraction of cerebral blood volume contained in the venous compartment of the tissue being measured is γ (typically γ is approximately 0.75), then we can then write the tissue oxygen saturation as:

$$StO_2 = SaO_2(1-\gamma) + \gamma SvO_2 \ .$$

(2.35)

We can then rearrange to get $SvO_2 = SaO_2(1-1/\gamma) + StO_2/\gamma$. Plugging this into Eq. (2.34) yields:

$$OEF = \frac{SaO_2 - StO_2}{\gamma \times SaO_2} \ .$$

(2.36)

2.5.2 Cerebral Blood Volume (CBV)

Cerebral blood volume (CBV), the total volume of blood that is contained within the cerebral vasculature of the brain, can be calculated as:

$$CBV = \frac{MW_{Hb} \times THC}{\rho_{bt} \times [Hgb_{blood}]} = \frac{MW_{Hb} \times THC \times 32 \ g/dL}{\rho_{bt} \times Hct}$$

(2.37)

where MW_{Hb} is the molecular weight of hemoglobin (6.45×10^4 g/moles); ρ_{bt} is the density of brain tissue (1.05 g/mL) [40]; $[Hgb_{blood}]$ is the concentration of hemoglobin in blood and is equivalent to $Hct/(32 \ gdL^{-1})$.

2.6 Diffuse Correlation Spectroscopy

Diffuse correlation spectroscopy (DCS) is a diffuse optical technique that uses temporal fluctuations (or spatial fluctuations) of light intensity to calculate a blood flow index (BFI, cm^2/s). Typically, DCS uses the same measurement geometry as DOS; near infrared light is launched into tissue at a source position, then travels diffusively through tissue to a detector fiber located at position different from the source on the tissue surface. The detected light field is built from a sum of many light pathlengths through the tissue (which can constructively or destructively interfere with one another at the detector). When there is motion within the tissue, then each photon pathlength is slightly changed, and the phases of the light fields associated with different paths change. This effect due to scatterer motion causes the light field and

light intensity to vary. Since red blood cells account for the major motions of scatterers in tissue, the intensity fluctuations are readily attributed to blood flow, with higher blood flow corresponding to faster (more rapid) intensity fluctuations. There has been a great deal of research validating DCS blood flow metrics (BFI) against other technologies and across a wide range of tissues [30,41-43].

2.6.1 Dynamic Light Scattering

As a background, we first discuss the traditional Dynamic Light Scattering (DLS) technique which works in the single-scattering regime. DLS is an optical technique commonly used for measuring motion of particles in a suspension using scattered light [30]. In the single-scattering limit, the sample is assumed to be dilute enough that light is scattered once or not at all as it traverses the sample (Figure 2.6). As seen in Figure 2.6, the incident electric field ($\vec{k}_{in}$) is scattered by an angle, resulting in a momentum transfer of: $\boldsymbol{q} = \vec{k}_{out} - \vec{k}_{in}$. As the particles move, the scattering of light from different particles creates destructive and constructive interference patterns in the electric field at the detector ($\boldsymbol{E}(t)$); it changes over time because the particles move and their scattered fields acquire different phase-shifts. For independent particles with isotropic dynamics, the detected fluctuations are described by the normalized electric field temporal auto-correlation function (g_1) at the detector as [30,44-46]:

$$g_1(\tau) = \frac{\langle \boldsymbol{E}^*(t) \cdot \boldsymbol{E}(t+\tau) \rangle}{\langle \boldsymbol{E}(t) \rangle^2} = e^{i2\pi f \tau} e^{-q^2 \langle \Delta r^2(\tau) \rangle / 6} \tag{2.38}$$

Here, f is the frequency of the incident light, $\boldsymbol{q}$ is the scattered wave-vector (the difference between the output and input beam wave-vectors), $\langle \Delta r^2(\tau) \rangle$ is the mean-square particle displacement in time τ, and the brackets $\langle \rangle$ represent time-averages or ensemble averages. Through this relationship, it can be seen that the decay of the correlation function of the temporal fluctuations of the scattered light gives quantitative information about the particle motions. For diffusion (e.g., Brownian motion), $\langle \Delta r^2(\tau) \rangle = 6 D_b \tau$ (D_b as the particle diffusion coefficient); for convection (random but ballistic motion), $\langle \Delta r^2(\tau) \rangle = \langle V^2 \rangle \tau^2$ with $\langle V^2 \rangle$ as the second moment of the particle speed distribution [30,47].

26
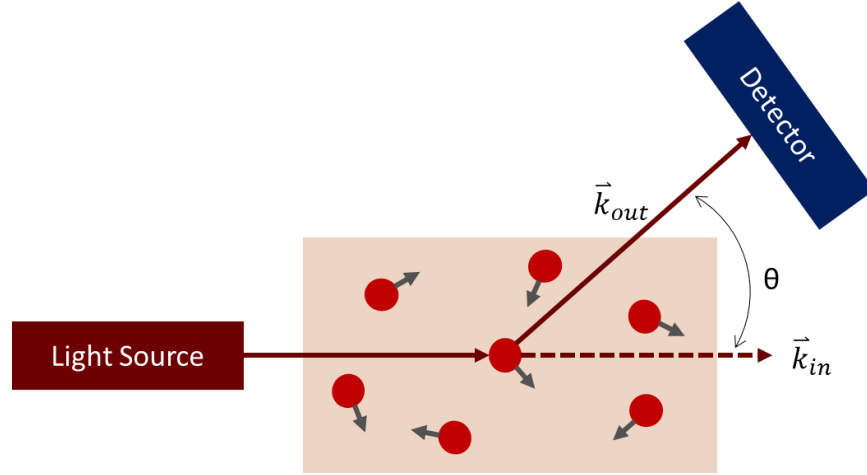
Figure 2.6 Illustration of a single scattering dynamic light scattering experiment.

Experimentally, the light-intensity is more easily measured. Thus, the light intensity auto-correlation function, $g_2(\tau)$, is typically used. The normalized intensity autocorrelation function is defined as:

$$g_2(\tau) \equiv \frac{\langle I(t)I(t+\tau)\rangle}{\langle I(t)\rangle^2}, \tag{2.39}$$

with detected light intensity $I(t) = |E(t)|^2$ at time t; the brackets $\langle\rangle$ represent time-averages or ensemble averages [30,47-49]. For Gaussian light sources, such as arise when laser light is scattered by a sample of random moving scatterers, $g_2(\tau)$ is related to $g_1(\tau)$ by the Siegert relation [49,50]:

$$g_2(\tau) = 1 + \beta|g_1(\tau)|^2, \tag{2.40}$$

with β inversely proportional to the number of independent speckle intensities detected. β is a constant set by the collection optics of the experiment (e.g., by the laser coherence length, stability of the laser, measurement geometry, etc.).

2.6.2 Correlation Diffusion Equation

In the previous section, I focused solely on the single-scattering limit of DLS. However, in samples such as tissue, the incident light is multiple scattered. In the case of a highly scattering medium, the temporal

27

fluctuations in the sample are impressed upon the (unnormalized) electric field auto-correlation function as it traverses the sample:

$$G_1(\vec{r}, \widehat{\Omega}, t, \tau) = \langle \mathbf{E}(\vec{r}, \widehat{\Omega}, t) \cdot \mathbf{E}^*(\vec{r}, \widehat{\Omega}, t + \tau) \rangle \tag{2.41}$$

Here the brackets $\langle \rangle$ represent time-averages or ensemble averages similar to above, and $\mathbf{E}(\vec{r}, \widehat{\Omega}, t)$ is the electric field at position $\vec{r}$ and time t propagating in the $\widehat{\Omega}$ direction. Ackerson et al first suggested that G_1^T is analogous to the radiance, L, defined in Eq. (2.5), and should follow a similar "correlation" transport equation [51,52]:

$$\nabla \cdot G_1^T(\vec{r}, \widehat{\Omega}, \tau) + \mu_t G_1^T(\vec{r}, \widehat{\Omega}, \tau) = Q(\vec{r}, \widehat{\Omega}) + \mu_s \int G_1^T(\vec{r}, \widehat{\Omega'}, \tau) \, g_1^s(\widehat{\Omega}, \widehat{\Omega'}, \tau) f(\widehat{\Omega}, \widehat{\Omega'}) d\Omega' \tag{2.42}$$

with $\mu_t = \mu_a + \mu_s$; $g_1^s(\widehat{\Omega}, \widehat{\Omega'}, \tau)$ as a normalized temporal field auto-correlation function for a single scattering cross section Eq.(2.39); $f(\widehat{\Omega}, \widehat{\Omega'})$ is the normalized differential single scattering cross-section; and $Q(\vec{r}, \widehat{\Omega})$ is the light source distribution. Notice that in the limit that τ goes to zero, we recover the transport equation for radiance.

As we did for the photon transport, Equation (2.42) can be reduced to a "correlation" diffusion equation as was done by Boas et al. (using the P$_1$ approximation identical to the steps used to derive the diffusion equation from the RTE) yielding [48,53]:

$$\left[\nabla \cdot (D(\vec{r})\nabla) - v\mu_a(\vec{r}) - \frac{\alpha}{3} v\mu_s' \kappa_0^2 \langle \Delta r^2(\tau) \rangle \right] G_1(\vec{r}, \tau) = -vS(\vec{r}) \tag{2.43}$$

Here, μ_a, μ_s', D and v are the same as from the photon diffusion equation from Section 2.3; α is the fraction of scattering events that occur from moving particles in the tissue (i.e., $\alpha = \mu_s'(moving)/(\mu_s'(moving) + \mu_s'(static))$); $\kappa_0 = 2\pi/\lambda$ is the wavenumber of light diffusion through the medium; $\langle \Delta r^2(\tau) \rangle$ is the mean square displacement in time τ of the scattering particles (i.e., the red blood cells in tissue). Several assumptions are made in the derivation of Eq. (2.43) and have been outlined in depth previously [26,30]. For example, this equation assumes that the medium is highly scattering and isotropic,

that the scatters are randomly oriented within the medium and have isotropic dynamics, and that

$\kappa_0^2 \langle \Delta r^2(\tau) \rangle \ll 1$.

Since the correlation diffusion equation (Eq. (2.43)) has the same form as the photon diffusion equation (Eq. (2.10)), the solutions for the correlation diffusion equation are formally the same as for the photon diffusion equation. Again, assuming a semi-infinite homogenous medium with a tissue-to-probe interface and an extrapolated boundary condition of $G_1(\rho, z = -z_b, \tau) = 0$, the Green's function solution is:

$$G_1(\rho, z, \tau) = \frac{v}{4\pi D} \left[\frac{\exp(-K(\tau)r_1)}{r_1} - \frac{\exp(-K(\tau)r_b)}{r_b} \right] \tag{2.44}$$

where

$$K(\tau) = \sqrt{\frac{v}{D}\left(\mu_a + \frac{\alpha}{3}\mu_s'\kappa_0^2\langle \Delta r^2(\tau)\rangle\right)} \tag{2.45}$$

and $r_1 = \sqrt{r^2 + (z - \ell_{tr})^2}$, $r_b = \sqrt{r^2 + (z + \ell_{tr} + 2z_b)^2}$ and $\ell_{tr} = 1/\mu_s'$, as before. The parameters α and $\langle \Delta r^2(\tau) \rangle$ are dependent on the scatterer dynamics (i.e., blood flow), and since these reside in the decay constant, $K(\tau)$, this is where the dynamical information to derive blood flow resides.

Like single-scattering DLS, the "multiply" scattered $G_2(\vec{r}, \tau) = \langle I(\vec{r}, t)I(\vec{r}, t + \tau) \rangle$ is typically measured from the intensity fluctuations where $I(\vec{r}, t) = |\vec{E}(\vec{r}, t)|^2$, and the Siegert relation (Eq.(2.40)) is used to relate the intensity auto-correlation function with the field auto-correlation function.

2.6.3 Blood Flow and Blood Flow Index

To understand the decay constant in the equation, we must understand the motion of the red blood cells in the tissue more deeply. Since diffusing light is almost completely absorbed when traversing through large arteries of veins, DCS is most sensitive to red blood cell motion in the microvasculature, i.e., in the arterioles, venules, and capillaries. The microvasculature is highly complex; thus, it should be expected that the distributions of velocity directions sampled would be nearly isotropic. Superficially, one might

29

expect the random flow model (i.e., $\langle \Delta r^2(\tau) \rangle = \langle V^2 \rangle \tau^2$) to apply [30]. However, many experiments from

our lab, and from other labs, have found that the observed auto-correlation function has the same form

as in Brownian motion (i.e., $\langle \Delta r^2(\tau) \rangle = 6D_b\tau$), except that the diffusion coefficient is not the Einstein

diffusion coefficient [42,54-56]. (The reason for this Brownian form derives from spatially dependent shear

stresses in the blood vessels (especially the arterioles); this shear causes the red blood cells to diffuse in

the direction transverse to the flow direction and is discussed in detail below.) Thus, the decay constant

becomes:

$$K(\tau) = \sqrt{\frac{v}{D}(\mu_a + 2\alpha\mu'_s\kappa_0^2 D_b\tau)} \tag{2.46}$$

where αD_b is dependent on the tissue dynamics where D_b is an "effective" diffusion coefficient. Both μ_a

and μ'_s are concurrently measured using the DOS instrumentation. Thus, a blood flow index is defined as:

$$BFI \equiv \alpha D_b \tag{2.47}$$

A typical value for BFI in human brain tissue is on the order of 1×10^{-8} cm^2/s.

An example of how the detected intensity values can be related to a calculated BFI is depicted in

Figure 2.7. The difference in the decay rates of the g_2 curves, which characterize the changes in intensity,

are thus shown to measure different BFI, and thus cerebral blood flow. By fitting to the intensity

autocorrelation functions, BFI is extracted.
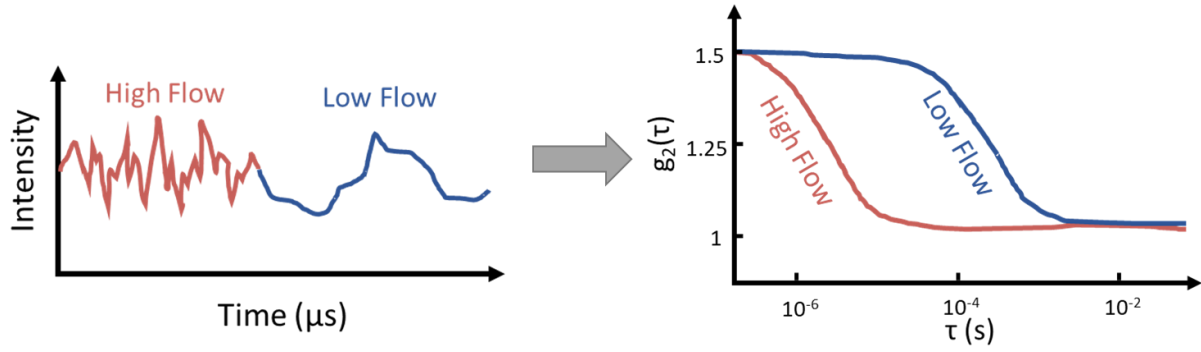
Figure 2.7 Example of DCS quantification of blood flow index from measurements of light intensity using an autocorrelation function.

2.6.4 Cerebral Blood Flow and Blood Flow Index

As a note, typical units for blood flow are mL/min/100g while BFI is measured in cm^2/s. Thus, although there has been some work done to calibrate BFI in absolute units [30,41-43], most of the clinical studies have used relative changes of blood flow compared to some baseline condition (or in another comparative way). This metric of relative cerebral blood flow ($rCBF$) is defined as:

$$rCBF = \frac{BFI}{BFI_0} \times 100\% \qquad (2.48)$$

with BFI_0 as the BFI measured during a baseline period.

2.6.5 Correction including Hematocrit Factor

Since red blood cells account for the majority of moving scatters in DCS measurements, one might expect that an increase in hematocrit (a measure of volume fraction of red blood cells in the blood) would impact DCS measurements [30]. Larger hematocrit implies more moving blood cells and faster autocorrelation function decay. This is an important feature of my thesis work, because hematocrit can change during CPB as well as in other scenarios (e.g., during blood transfusions, anemia (blood loss), severe dehydration, sickle cell disease or extracorporeal membrane oxygenation). I next discuss how to incorporate hematocrit variation into the analysis.

My derivation showing the dependence of CBF on hematocrit builds on the theoretical work done by Boas et. al. They determined a relationship between the signal (BFI) obtained from DCS measurements and absolute blood flow; although they didn't derive it explicitly, the relationship depends on hematocrit. It also depends on average vessel diameter in the interrogated volume of tissue [23]. My work, presented in Section 6.3, is a novel application of this theory in an in vivo study; previously all other work has been done with computational models or in vitro experiments.

To understand the model, following Boas et al, we first define a tissue geometry consisting of a homogenous tissue with evenly dispersed blood vessel of radius R spaced h_{space} apart. Clearly this model is not perfect, but it roughly captures the main features of the problem. The vessels have different optical properties from their surrounding tissue and specified internal flow profiles as shown in Figure 2.8.
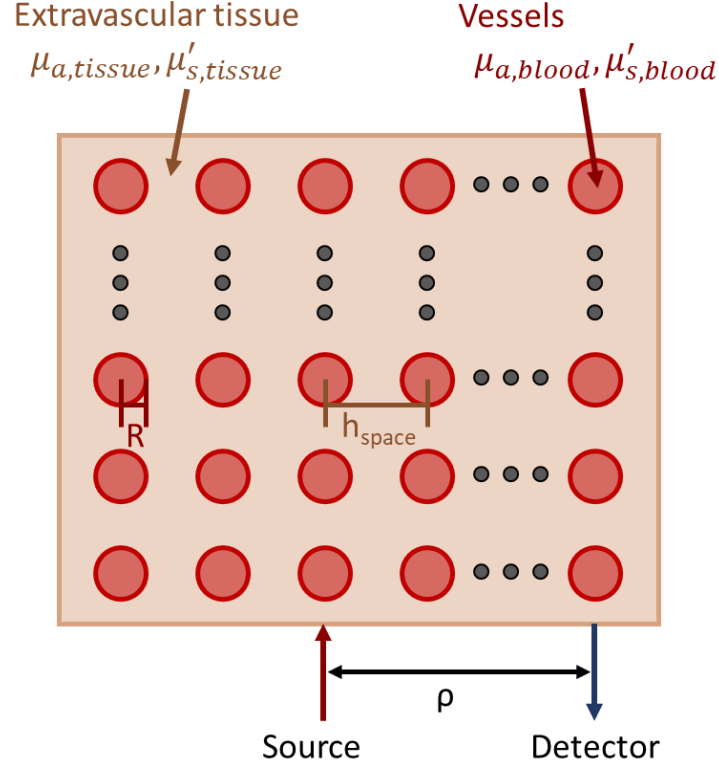
Figure 2.8 Tissue geometry used in this derivation. This is the (x,z) plane with the y-axis being parallel

with the vessels. This figure is adapted from Boas et.al. [23].

Within each vessel, the velocity profile is assumed to be of the form below, in terms of the radial

variable, r, which is zero at vessel center (the velocity and shear profile are depicted in Figure 2.9):

$$v_{RBC}(r) = v_{max}\left\{1 - \left[a\left(\frac{r}{R}\right)\right]^k\right\}. \tag{2.49}$$

Here v_{max} is the maximum speed at the center of vessel; a as a scaling factor, allowing for nonzero

velocity at the vessel wall; and the exponent k is a metric of the 'bluntness' of the profile. For small

channels of slowly moving, viscous fluids, laminar flow can be assumed (blood is one of the classic

examples of laminar flow). Thus, $a \approx 1$ and $k \approx 2$, so $v_{RBC}(r)$ can be written with good approximation

as:

$$v_{RBC}(r) = v_{max}\left\{1 - \left(\frac{r}{R}\right)^2\right\}.$$
(2.50)

Since the velocity of the red blood cell will be impacted by the shear flow due to interparticle interactions, it is important to consider the shear rate. The shear rate quantifies the velocity gradient within the fluid, indicating the change in velocity with respect to distance from the vessel wall (shown in Figure 2.9). Previous publications have examined the relationship between the velocity profile of a red blood cell and shear, specifically how DCS measurements may also be sensitive to the shear-induced diffusion of red blood cells in blood flow [57,58]. These studies noted that the diffusion coefficient its proportional to the flow shear rate [23]. The relationship between sheer and red blood cell movement is further discussed in Appendix 2.7.
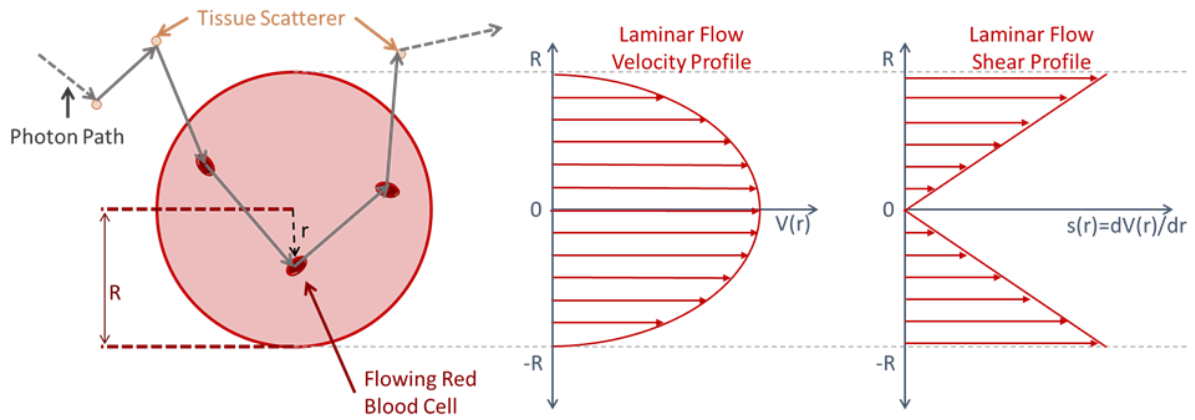
Figure 2.9 Impacts of photon tracking from location of scatterer. Each scattering event within a vessel must consider the location as the velocity and shear profile are dependent on the radial position. This image shows that the blood flow at the center of the vessel is faster than the flow at the vessel walls, where the flow has essentially zero velocity. This figure is adapted from Boas et.al. [23].

Importantly, previous experimental studies have carefully examined the relationship between the red blood cell transverse diffusion coefficient, $D(r)$, and the shear rate, $s(r)$ [59-61]. Specifically, it was found that

$$D(r) = \alpha_{sheer} s(r) = \alpha_{sheer} \left| \frac{\partial v_{RBC}}{\partial r} \right| = 2 \alpha_{sheer} \frac{v_{max} \, r}{R^2} . \tag{2.51}$$

Here α_{sheer} is defined by Goldsmith and Marlow and measured to be $\alpha_{sheer} \approx 10^{-6} \text{mm}^2$ [59]. Given a parabolic laminar profile and uniform photon sampling of the blood vessel, the spatially weighted average of the red blood cell transverse diffusion coefficient can be written as

$$\langle D(r) \rangle = \alpha_{sheer} \frac{4 \, v_{max}}{3 \, R} . \tag{2.52}$$

To relate all of this to the DCS-measured blood flow index, Boas et. al. defined BFI in terms of the probability of photon scattering from a red blood cell, P_{RBC}. For a diffusive model of blood cell motion, this can be written as

$$BFI = P_{RBC} \langle D(r) \rangle . \tag{2.53}$$

The P_{RBC} is the product of the volume fraction of blood ($f_{blood} = \pi R^2 / h_{space}^2$) and ratio of the blood reduced scattering coefficient to the average tissue reduced scattering coefficient:

$$P_{RBC} = \frac{\pi R^2}{h_{space}^2} \frac{\mu'_{s,blood}}{\mu'_{s,avg}} . \tag{2.54}$$

Here $\mu'_{s, avg} = f_{blood} \times \mu'_{s, blood} + (1 - f_{blood}) \times \mu'_{s, tissue}$. Thus,

$$BFI = \frac{\pi R^2}{h_{space}^2} \frac{\mu'_{s, blood}}{\mu'_{s, avg}} \alpha_{sheer} \frac{4 \, v_{max}}{3 \, R} = \frac{4 \, \pi \, \alpha_{sheer} \, v_{max} \, R}{h_{space}^2} \frac{\mu'_{s, blood}}{\mu'_{s, avg}} . \tag{2.55}$$

Using this geometry, we define an absolute blood flow: $CBF = \frac{1}{2} \pi R^2 v_{max} n_{vessels}$ with $n_{vessels} = \frac{\# \, vessels}{unit \, volume} = \frac{1 vessel}{h_{space}^2}$. Plugging this into the equation for BFI yields the relationship:

$$BFI = \frac{8 \, \pi \alpha_{sheer}}{3 \, R} \frac{\mu'_{s, blood}}{\mu'_{s, avg}} CBF , \tag{2.56}$$

which can be rewritten as

35

$$CBF = \frac{3\,R\,\mu'_{s,avg}}{8\,\pi\,\alpha_{shear}\,\mu'_{s,blood}} \times BFI \ . \tag{2.57}$$

The equation requires determination of $\mu'_{s,blood}$, the reduced scattering coefficient of blood. To do this, I employ the commonly used approximation by Twersky of [21,62]

$$\mu_{s,blood} = \frac{Hct\,(1-Hct)}{vol_{RBC}} \times \sigma_{RBC} \ . \tag{2.58}$$

Here vol_{RBC} as the average volume in a single red blood cell, σ_{RBC} as the elastic light scattering total cross-section of a single red blood cell, and Hct (hematocrit) is the volume fraction of red blood cells in the blood. I assume that vol_{RBC} and σ_{RBC} are constant; if they change at all, they will certainly change by a much smaller percentage than Hct. Since $\mu'_s = \mu_s(1-g)$, and keeping only first order terms, it follows that

$$CBF \approx \frac{3\,vol_{RBC} \times \mu'_{s,avg} \times R}{8\,\alpha_{shear} \times Hct \times \sigma_{RBC} \times (1-g)} \times BFI \ . \tag{2.59}$$

Moreover, if we are interested in relative CBF, as we often are, then most of the other variables will cancel out

$$rCBF \approx \frac{\mu'_{s,avg}}{Hct} \times BFI \ . \tag{2.60}$$

2.6.6 Limitations of Model

While this is likely a good first order correction, there were several assumptions made in the application of this equation. First, we have assumed that R remains constant during hematocrit-induced changes in $\mu'_{s,avg}$ and $\mu'_{s,blood}$. Vasoconstriction (shrinking of the blood vessels, i.e., a reduction in R) is likely when CO_2 production decreases, which commonly decreases during hypothermia as metabolism is decreased and oxygen consumption goes down [63-65]. It was previously found that while ischemia on its own did not impact pial arteriolar diameter in piglets, it did restrict the ability to vasodilate in response to hypotension. The average diameters measured in that study ranged from 111-206μm [65]. Unfortunately, the vessel radius can be impacted by a multitude of factors and is coupled with blood flow, making this a

difficult parameter to account for. This is a gap in the current knowledge that will need to be accounted for in future studies. The formulation from Boas et al., Eq. (2.57), assumes a common vessel diameter ranging from 60-200μm, however it is hypothesized that the formula should still hold if an effective vessel radius is used instead [48].

We also assume that α_{shear} remains constant in Eq. (2.57). This is also an oversimplification of the problem. Instead, it is expected that α_{shear} is linearly proportional to hematocrit from 5-45%, on the order of 10^{-9} mm^2 per % hematocrit change [66]. Since we observed a 10% change in hematocrit due to CPB support, this would be about 1% error, and was thus deemed negligible for the first order correction.

Nevertheless, this equation outlining the relationship between absolute cerebral blood flow and the optically measured BFI could have wide-reaching implications. Not only is this important for the analysis I will do in Section 6.4.2 when hematocrit is found to significantly change during cardiopulmonary bypass, but when there is any change in hematocrit. Other examples of this could include something as common as severe dehydration, which would increase the concentration of hemoglobin in the blood as the total volume would decrease. It would also be important to include this correction during blood transfusions or if there has been significant blood loss.

2.6.7 Quantification of Cerebral Metabolic Rate of Oxygen

Cerebral metabolic rate of oxygen ($CMRO_2$) is the rate at which oxygen is metabolized by the brain. It's quantification with optics is thus a promising metric of metabolic distress that can result in neurologic injury. Assuming steady state conditions, we estimated CMRO$_2$ via Fick's law, *i.e.,*

$$CMRO_2 = CaO_2 \times OEF \times CBF,$$

(2.61)

where CaO_2 is the arterial concentration of oxygen (mL O$_2$/dL blood), OEF is the oxygen extraction fraction, and CBF is absolute cerebral blood flow [30]. The product of CaO$_2$ and CBF is the rate of oxygen

37

delivery to the brain. OEF is the fraction of oxygen in the arterial blood extracted by the tissue. We then

used Equation (2) to compute fractional changes in CMRO₂ from baseline:

$$rCMRO_2 \equiv \frac{CMRO_2}{CMRO_{2,0}} = \frac{CaO_2}{CaO_{2,0}} \times \frac{OEF}{OEF_0} \times \frac{CBF}{CBF_0},$$

(2.62)

where the subscript "0" denotes the mean of the parameter across the baseline period (see Fig. 1).

2.7 Appendix: Relationship Between Vessel Shear, Blood Flow, and the Blood Flow Index

Shear rate and blood flow are closely intertwined in the context of the fluid dynamics within blood vessels.

The shear rate refers to the rate at which adjacent layers of blood move relative to one another, while the

blood flow refers to the volume of blood that passes through a given point in a blood vessel per unit time.

In general, the shear rate within a blood vessel is directly proportional to the blood flow velocity. When

blood flows through a vessel, it experiences different velocities across its cross-sectional area. The blood

flow at the center of the vessel tends to be faster than the blood flow at the vessel walls due to the no-

slip condition, where the blood in direct contact with the vessel wall has zero velocity (shown in Figure

2.9). This velocity gradient across the vessel leads to shear between adjacent layers of blood. This type of

flow can be well described with Poiseuille's law and has been previously described for red blood cells by

Goldsmith and Marlow [67]. This study was then expanded to measure the shear rate experienced by red

blood cells within a vessel [59].

The fluid dynamics experienced by red blood cells while flowing within a vessel have been

previously documented both *ex vivo* using video microscopy in microchannels as well as *in vivo* [59-61].

From these studies we can use Equation (2.51) to describe the diffusion coefficient, showing that shear

induces a diffusive behavior in red blood cells where the diffusion coefficient is proportional to the shear

rate [23].

The estimated proportionality between the diffusion coefficient and the sheer rate, α_{sheer}, used

within this thesis, was defined by Goldsmith and Marlow and measured to be $\alpha_{sheer} \approx 10^{-6} \text{mm}^2$ [59].

38

This measurement was done *ex vivo* under a microscope in a transparent suspensions of red cell ghosts (a good model for whole blood). A range of radii (32 to 80 μm) and volume concentrations (40-47%) were used. The dispersion coefficient was calculated based off of the change in radial distance from the tube axis over a period of 0.5 sec. This was then plotted against the shear rate at the mean radial position of the cell path. The proportionality α_{sheer} was then defined as the slope of this line.

There are several assumptions made within this model that could lead to inaccuracies with our equation for absolute cerebral blood flow. We do go below the concentration of red blood cells used in this study (we were measuring around 25% Hct while they were around 40%). And as always, there are limitations in an ex vivo study such as mimicking the compliance properties of the vessel walls. These are all deficits in the current model that would need to be improved upon in future studies and validated against absolute measures of blood flow.

CHAPTER 3

INSTRUMENTATION

3.1 DOS Instrumentation

The FD-DOS instrument used in this work was a custom designed Imagent system (ISS Inc, Champaign, IL, USA). The instrument has 16 sources that can be coupled to optical fibers through an SMA coupler. The 16 sources are distributed evenly across four different light wavelengths (690nm, 725nm, 780nm and 830nm; 4 sources for each wavelength). A radiofrequency (RF) oscillator modulates the light sources at 110MHz as discussed in 2.3.1 (Eq. (2.11)) to produce diffuse photon density waves in tissue. To enable the separation of the source wavelengths and positions in the detected signals, switched-source; the sources switch on and off in sequence such that only one source is on at a time. Approximately 0.1 seconds is required to switch through all 16 sources, and source output powers on the tissue are ~5 to 10 mW. The sources need about 30 minutes to warm up before a measurement to ensure accuracy and stability.

The Imagent contains two photomultiplier tubes (PMT) for light detection. The PMTs are sensitive in the visible and NIR wavelength range (up to 850nm) and have a large linear range for light detection. Heterodyne detection is employed to measure the amplitude and phase of the diffuse photon density wave from each source. Specifically, the gain of the PMT is modulated at 100 MHz +5kHz. The mixing of the PMT gain modulation with the detected diffuse photon density wave emerging from the tissue (modulation at 100 MHz) results in an electronic output signal from the detector oscillating at the 5 kHz beat frequency. The amplitude and phase of this signal is proportional to the amplitude and phase of the diffuse photon density wave. Further, the phase of the 5 KHz beat frequency signal is easier to measure than the phase of the 100 MHz diffuse photon density wave. The beat frequency signal is directly sampled using a high-speed analog to digital converter, and a fast Fourier transform (FFT) is performed to determine the amplitude and phase. In practice, to help reduce drift, a FFT is also performed on a

reference signal (*e.g.,* the detected signal from one of the 16 sources), and the difference between the phase of each detected signal and the phase of this reference signal is used for analysis.

3.2 DCS Instrumentation

The DCS instrumentation (Figure 3.1) is comprised of one long-coherence length (>10m) 785 nm laser (Custom iBeam smart WS, TOPTICA), as well as eight single photon counting avalanche photodiodes (APDs, SPCM-AQ4C; Excelitas Technologies, Corp., Waltham, MA, USA) to detect and temporally resolve the arrival of photons. The stream of digital pulses generated by the photon counting APD (each pulse corresponds to the arrival of a photon) is sent to an edge-detecting counter on the PCIe6612 data acquisition board, and the accumulated counts from the board in 1 μs time-intervals are used for real-time computation of the intensity temporal autocorrelation function in software [68]. The autocorrelation function is computed for delay times ranging from 1 μs to 250 μs. This autocorrelation function is fit to derive/compute a BFI (Blood Flow Index) as described in Chapter 2. I used the FD-DOS estimates of tissue optical properties at the DCS wavelength as inputs in the fit to derive BFI.
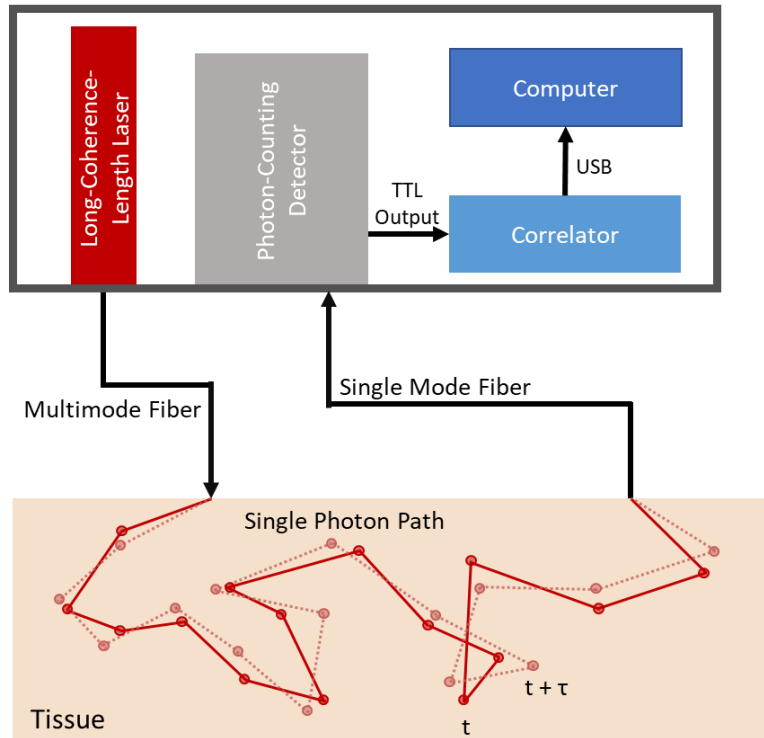
Figure 3.1 Schematic of typical DCS Instrumentation. The DCS instrument consists of a long-coherence-length laser coupled to the tissue through a multimode optical fiber. Eight single mode fibers couple the tissue to eight single photon counting avalanche photodiodes.

A 400 µm diameter multimode fiber (in the ray-picture, each angle of propagation corresponds to a different fiber mode, Figure 3.2) was used to couple the laser to the tissue. The use of the multimode fiber ensures good transmission of the laser light to the tissue, though the different time delays experienced by the different light modes that propagate through the fiber results in some loss in source coherence. The long coherence length (> about 5-10m) of the light source, however, helps ensure that the coherence length of the output light emerging from the source fiber is substantially greater than the spread of light pathlengths through tissue (< 1 m). This latter condition must be met to measure speckle intensity fluctuations induced by red blood cell motion.
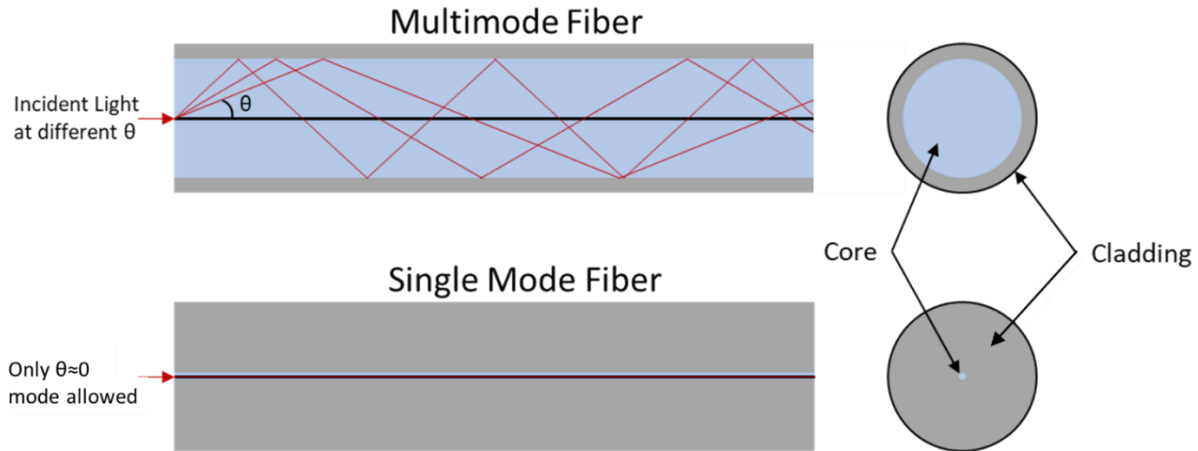
Figure 3.2. Ray-optics schematic of modes in Multimode vs Single Mode fibers. The core diameter of a

multimode fiber is around 50 μm while the core diameter of a single mode fiber is

approximately 9 μm.

By contrast, single mode fibers were used to couple the detectors to tissue to optimize signal-to-noise ratio for BFI [49]. Single mode fibers are necessary for sensitive detection of blood flow-induced speckle intensity fluctuations, but their small core diameter size (5 μm) results in low light collection from the tissue. Single-mode detection is challenging, as it can be difficult to measure adequate signal through hair or at long source-detector distances (> 3 cm) [49,69].

3.3 Phantom Calibrations

In order to use FD-DOS data obtained at multiple source detector separations (SDS) to accurately determine absolute $[HbO_2]$ and $[Hb]$, a calibration must be performed [70]. The tissue optical properties influence the amplitude and phase of the multi-SDS FD-DOS measurements, but there are also undesired influences from other factors such as wavelength-dependent fiber transmission. The effects from these other factors are combined via the use of a light coupling coefficient. Each source and each detector has a different light coupling coefficient to tissue, and the measured fluence rate for a given source-detector pair is equal to the product of the true fluence rate with the pair's coupling coefficients. To determine the

coupling coefficients, tissue-mimicking phantoms with known optical properties are used before and/or after the tissue measurement (it is typically assumed that light coupling coefficients remain constant during the measurement). Since calibration usually needs to be performed with every measurement, most groups, ours included, use a solid phantom with similar optical properties to that of tissue. Solid phantoms have the benefit of being permanent and stable for continued use.

3.3.1 Phantom Properties

To accurately employ calibration measurements, $\mu_{a,cal}$ and $\mu'_{s,cal}$ for the phantom must be known. We use solid phantoms purchased from ISS Inc. (Champaign, IL, USA) composed of room temperature vulcanized (RTV) 615 silicone resin, titanium dioxide (rutile, 1–2-micron sized particles) for scattering and carbon black for absorption. These materials are commonly used in tissue mimicking phantoms [70,71].

Silicone is used as the base material for the phantom because it is moldable, transparent, and has a refractive index of about 1.4 [72-75]. This is similar to the refractive index of tissue which is around 1.35-1.5 [72]. It's soft rubber texture mimics a stiff tissue and can be molded into a variety of shapes and sizes to model different tissue and organ shapes. It also offers the possibility to include nonorganic scatters and chromophores [72,76]. To create these tissue phantoms, ISS used an RTV615 silicone with negligible optical scattering and absorption in the near-infrared. Thus, additional materials need to be added to the silicone to control the phantom's absorption and scattering [72-75]. Carbon black is commonly used to increase absorption [70,71,76-78]. Carbon black has very little contribution to scattering and has a relatively constant absorption spectra over the 630-870 nm range [77,78]. The amount of carbon black added was titrated by ISS to obtain absorption properties similar to tissue [71,78].

To increase scattering, titanium dioxide (TiO_2) is commonly used. TiO_2 is the main pigment in white paint, and thus readily available [73,79]. The TiO_2 absorption is even less than that of silicone and the scattering strength versus wavelength is relatively constant. The index of refraction is around 2.4-2.9, thus

the scattering anisotropy value g is lower than that in tissue, and additional scattering particles are often added to mimic the tissue's reduced scattering coefficient [73,79]. TiO_2 is stable in a silicone phantom and comes in a variety of well-controlled formulations, thus making for a simple, permanent phantom that can be easily used for daily calibration of an instrument [71].

3.3.2 Measuring Phantom Properties

While the approximate optical properties can be estimated from the concentrations of carbon black and TiO_2 added to silicone, the exact optical properties are needed for FD-DOS calibration. Thus, the phantom's optical properties need to be precisely measured. One way to measure the phantom's properties is to acquire multiple SDS data on the phantom with a single source and a single detector. By using a single source and detector, the coupling coefficient is the same for all SDS.

I used this method to measure the optical properties of the phantom at 727, 750, 800, and 827 nm. Optical properties at each wavelength were measured separately. A multimode source fiber (*e.g.,* described above) was mounted to coupled vertical and horizontal translational stages (NRT100, Thor Labs, Newton, NJ) as shown in Figure 3.3. The positions of the vertical and horizontal translational stages are adjusted via computer control with a precision of 1µm. This allows for the source to be incrementally positioned further away from the detector to achieve multiple SDS. The detector fiber was secured to an optical table using a post and a right-angle post clamp. The detector fiber was placed at least 2 cm from the edge of the phantom such that the semi-infinite boundary condition could be utilized. A reference source of the same wavelength was used to calculate the change in phase. This was secured in the same manner as the detector fiber and positioned 2.9 cm away.
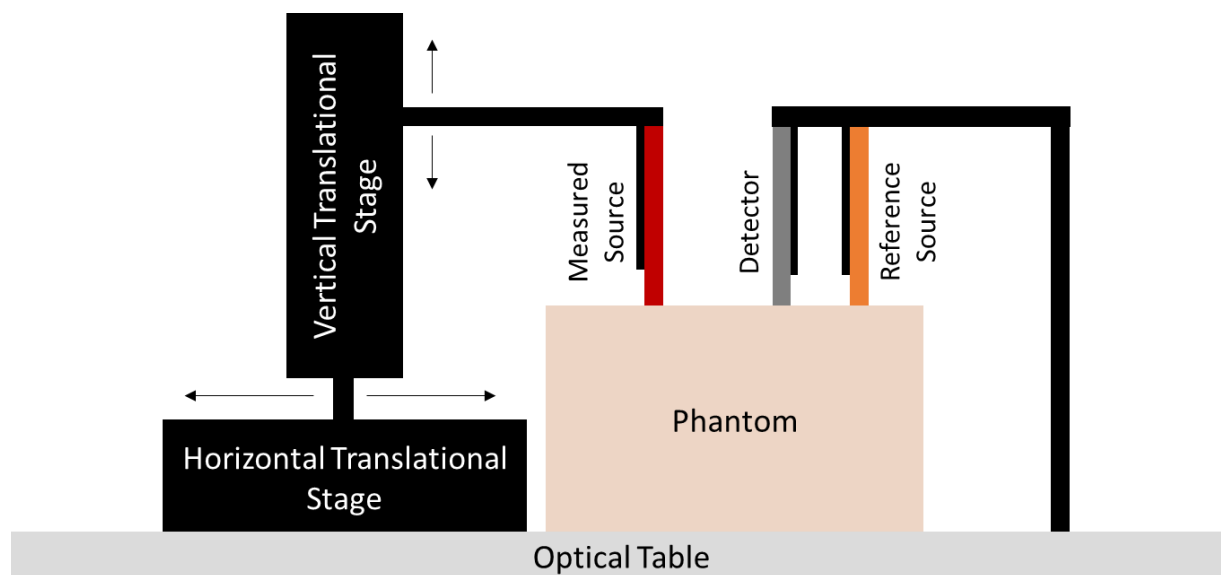
Figure 3.3 Schematic of setup used to measure optical parameters of a phantom used for instrument

calibration.

Since these are precise measurements, extra precautions were taken to remove any ambient light

that may interfere with the measurement. The phantom was wrapped in a black cloth and the top of the

phantom that was not being measured was covered in black electrical tape. Black rubber was fitted around

the detector fiber and the reference fiber. All reflective surfaces were covered with black tape and the

room lights were turned off.

A single measurement consisted of two parts, 1) setting the SDS by moving the measured source

fiber with the translational stages and 2) collecting intensity and phase data at that location. For each

source, the initial SDS was set at approximately 1.4 cm (and measured precisely with a calipers) and the

source was set to just be contacting the phantom. After a measurement was completed, the vertical

translational stage raised the fiber off the surface of the phantom by 0.5 mm to ensure neither the fiber

nor the phantom was damaged during the translational. The horizontal stage then moved the source fiber

2 mm further away from the detector fiber before the vertical stage lowered it back down 0.5 mm to be

contacting the phantom again.

A measurement of intensity and phase was taken at each location. I waited until there were at least 1300 measurements (approx. 3 min) at the location and the calculated the mean and standard deviation of both intensity and phase at that location. This was done from 1.4 cm to 3.2 cm. We were limited by the size of the phantom for the furthest data point as getting within 2 cm of the phantom edge could cause break down of the semi-infinite boundary condition. Once intensity and phase data were collected for all positions (Figure 3.4), Eqs. (2.27), (2.28), (2.29), and (2.30) were used to calculate μ_a and μ_s' for each wavelength (Figure 3.5). These measurements were then used to calibrate the FD-DOS instrument for measurements.
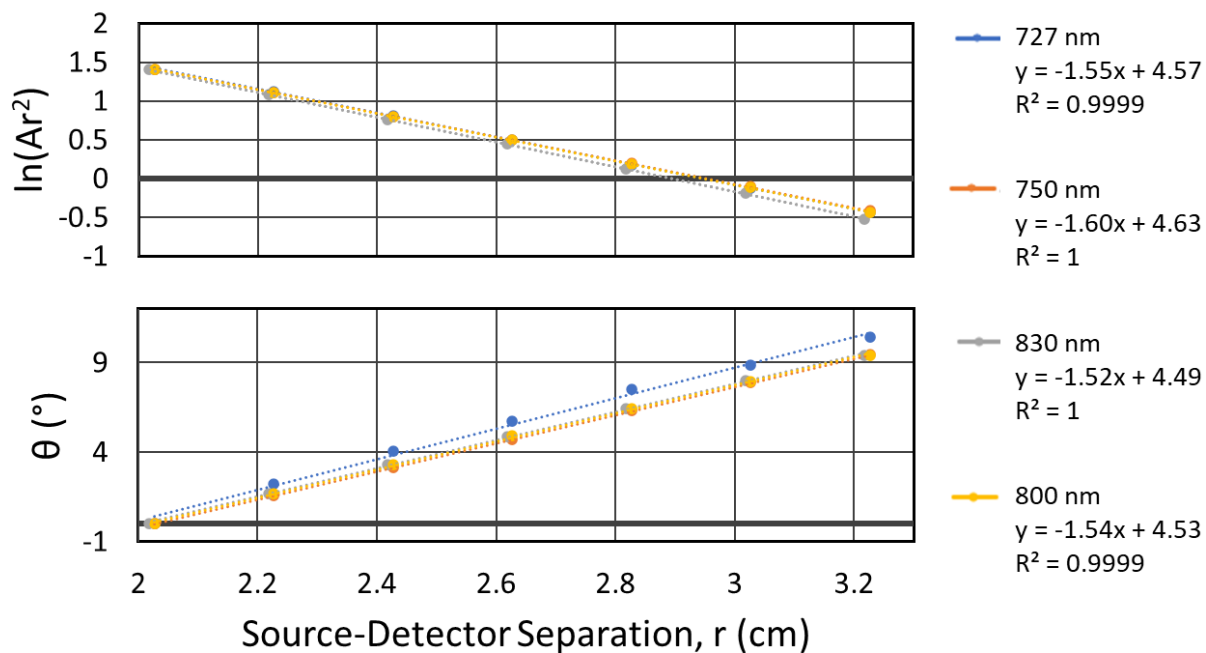
Figure 3.4 Linear relationships for phase-shift and adjusted amplitude *at four wavelengths* to calculate

k_i and k_r needed for calibration.

λ (nm)	μ_a (cm⁻¹)	μ_s' (cm⁻¹)
727	0.166	4.777
750	0.187	4.539
800	0.180	4.354
827	0.177	4.325
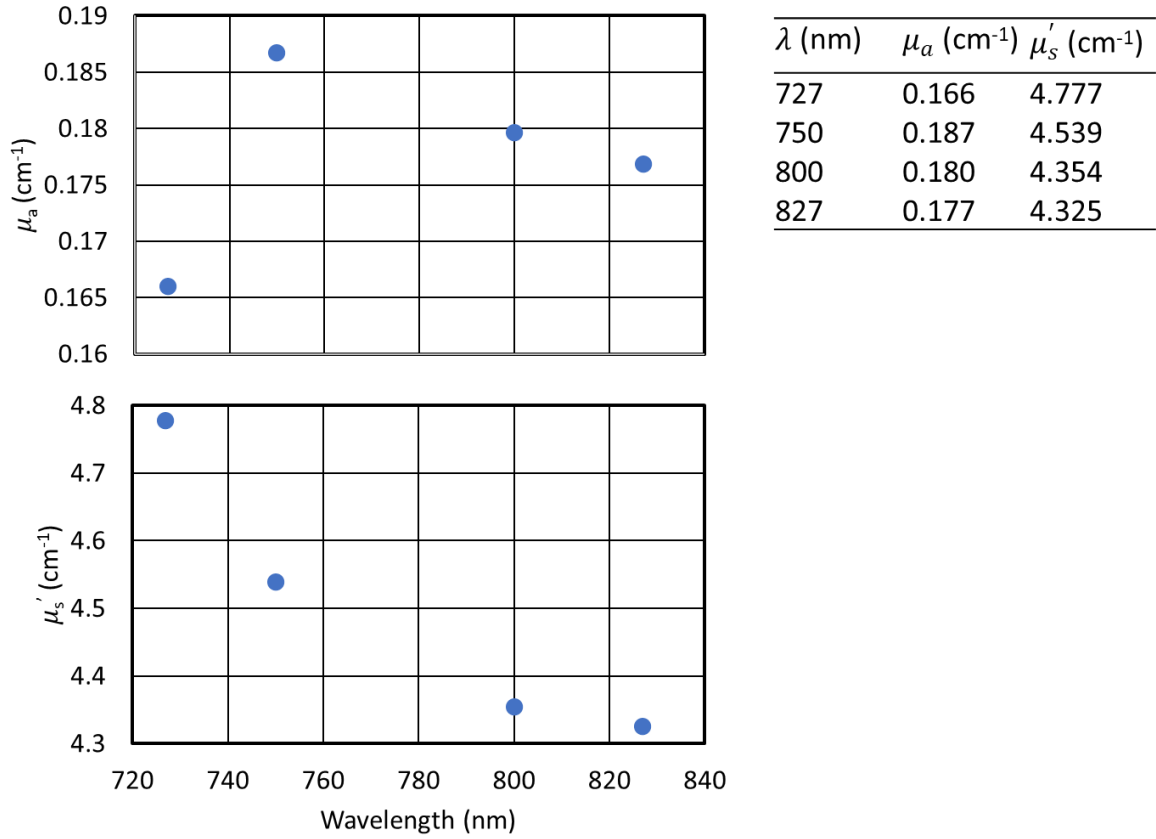
Figure 3.5 Calculated Optical Properties for Four Wavelengths. Calculated absorption and scattering

coefficients for a silicone phantom.

3.3.3 Measuring and Applying the Calibration Coefficients

Once the optical properties of the phantom are well known, the calibration coefficients are calculated for

each wavelength and each source-detector pair (shown in Figure 3.6). To do this, we start by calculating

the amplitude and phase predicted by the photon diffusion model based on the known phantom optical

properties that I measured, $\mu_{a,cal}$ and $\mu_{s,cal}'$. I specifically used the long source-detector separation limit

of the semi-infinite photon diffusion solution to calculate the "wavevectors" $k_{i,cal}$ and $k_{r,cal}$ via Equations

(2.16) and (2.17). Thus, the true amplitude (A^P) and phase (θ^P) for the phantom predicted by the photon

diffusion model as a function of source-detector separation (r) are:

$$A^P(r) = A_0^P \left(\frac{e^{-k_{i,cal}r}}{r^2} \right) ; \qquad (3.1)$$

$$\theta^P(r) = k_{r,cal}r + \theta_0^P . \qquad (3.2)$$

Here A_0^P and θ_0^P are constants.
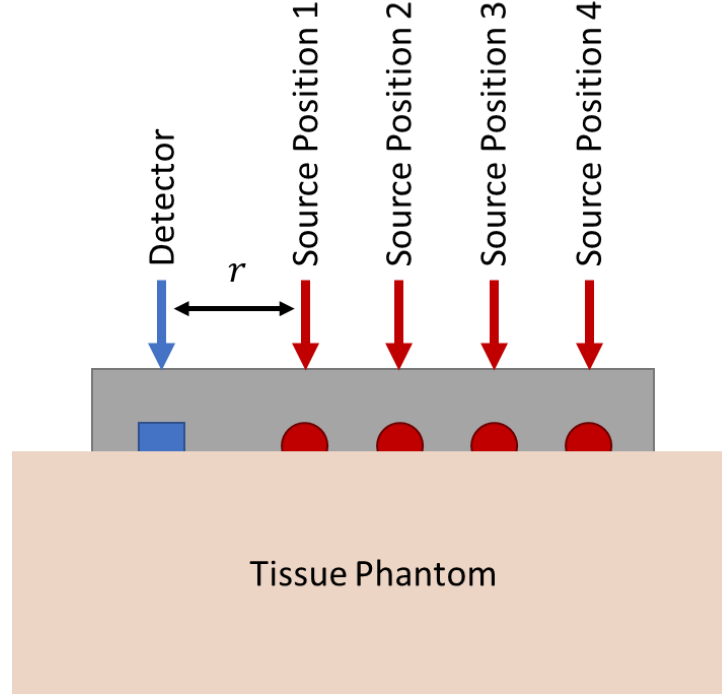
Figure 3.6 Schematic of multiple source detector positions. Calibration coefficients must be calculated

for each wavelength and each source detector pair. This is done by measuring $A(r)$ and $\theta(r)$ for

each r (the distance between the detector and source position).

The next step is to estimate the optical coupling coefficients, C, from the true amplitude and

phase computed from the known optical properties. To distinguish the true fluence rate from the

measured fluence rate, I will denote the measured fluence rate as $I = |I|e^{-ip}$, where $|I|$ and p are the

measured amplitude and phase. I is proportional to the true fluence rate (Φ) via the coupling coefficient,

i.e., $I = C \cdot \Phi$. Here, C is a complex number with its own amplitude (C_a) and phase (C_p) components, *i.e.,*

$C = C_a e^{-iC_p}$. Let's now consider the measurement for source i and detector j on the calibration phantom (source-detector separation is r_{ij}). The measured fluence is

$$I_{i,j}^P = |I_{ij}^P|e^{-ip_{ij}^P} = C_{a,i}C_{a,j}e^{-i(C_{p,i}+C_{p,i})}A^P(r_{ij})e^{-i\theta^P(r_{ij})}. \tag{3.3}$$

Recall that A^P and θ^P are given by Equations 0.1 and 0.2, respectively. Equation 0.3 is a system of two equations:

$$C_{a,i}C_{a,j} = |I_{ij}^P|/A^P(r_{ij}); \tag{3.4}$$

$$C_{p,i} + C_{p,j} = p_{ij}^P - \theta^P(r_{ij}). \tag{3.5}$$

After the calibration phantom measurements, the probe is then place on the tissue of interest. The amplitude and phase measured on the tissue are given by:

$$|I_{ij}| = C_{a,i}C_{a,j}A(r_{ij}); \tag{3.6}$$

$$p_{ij} = C_{p,i} + C_{p,j} + \theta(r_{ij}). \tag{3.7}$$

The true tissue amplitude and phase are obtained by substituting Eqs. (3.4) and (3.5) into Eqs. (3.6) and (3.7):

$$A(r_{ij}) = \frac{A^P(r_{ij})}{|I_{ij}^P|}|I_{ij}|; \tag{3.8}$$

$$\theta(r_{ij}) = p_{ij} - \left(p_{ij}^P - \theta^P(r_{ij})\right). \tag{3.9}$$

Again, $A^P(r_{ij})$ and $\theta^P(r_{ij})$ are given by Equations (3.1) and (3.2). Note that the constants A_0^P and θ_0^P in Equation (3.1) and (3.2) are unknown, but these will be the same for all source-detector pairs. Thus, the multi-distance fitting to the photon diffusion model can be used to derive tissue optical properties (*e.g.,* as shown in Figure 3.4 and Figure 3.5).

PHYSIOLOGIC METRICS OF CEREBRAL METABOLIC HEALTH

4.1 Introduction and Biology

A major focus of my thesis is to improve understanding of the effects of cardiopulmonary bypass (CPB) on cerebral metabolism. Here, the word metabolism refers to the consumption of glucose and oxygen to produce energy in cells. Non-invasive, optical measurement of cerebral oxygen metabolism provides a window into the mitochondrial health of cells and holds promise as an early indicator of adverse physiology that could result in irreversible injury. Several physiologic metrics of cerebral metabolic health were concurrently acquired alongside optical measurements to help elucidate potential indicators. Before explaining the different metrics, I will give a brief overview of the basic metabolic pathways.

4.1.1 Aerobic Respiration

The primary method employed by cells to generate energy (ATP, adenosine triphosphate) from glucose is aerobic respiration, which occurs in the presence of oxygen (**Error! Reference source not found.**). This process is composed of several metabolic processes: glycolysis, pyruvate decarboxylation, the citric acid cycle (commonly called the Krebs cycle), and the electron transport chain [80]. All together these processes have the potential to produce a maximum of 38 ATP. The global reaction is:

$$C_6H_{12}O_6(s) + 6\ O_2\ (g) \rightarrow 6\ CO_2\ (g) + 6\ H_2O\ (l) + 38\ ATP\ . \qquad (4.1)$$
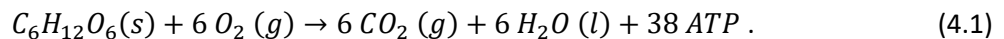
This reaction is exothermic, and thus it can occur spontaneously. While aerobic respiration has the potential of producing up to 38 ATP, as a result of the complexities of the respiratory chain, aerobic respiration often only produces around 30 ATP per glucose due to factors such as membrane semi-permeability [80], etc. Nevertheless, aerobic metabolism is up to 15 times more efficient than its counterpart anaerobic respiration, occurring in the absence of oxygen.

The first step in both aerobic and anaerobic respiration is glycolysis. Glycolysis occurs both in the presence and absence of oxygen. It is the production of pyruvate from glucose, occurring in the cytosol of the cell with the overall reaction:

$$Glucose + 2\,NAD^+ + 2\,ADP + 2\,P_i \rightarrow 2\,Pyruvate + 2\,NADH + 2\,H^+ + 2\,ATP + 2\,H_2O. \qquad (4.2)$$
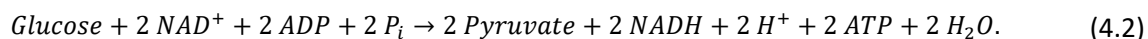
Here $Glucose$ is ($C_6H_{12}O_6$); NAD^+ and $NADH$ are the oxidized and reduced forms of nicotinamide adeine dinulcleotide; ADP is adenosine triphosphate; ATP is adenosine diphosphate; P_i is a phosphate group; and H^+ is a hydrogen ion [81]. If there is oxygen present, then pyruvate is transported into the mitochondrial matrix, converted to acetyl-CoA (which releases CO_2), and goes through the citric acid cycle as a part of aerobic metabolism. Otherwise, the pyruvate molecule is subsequently converted to lactate in the anaerobic pathway.

Per aerobic metabolism, once the acetyl-CoA is produced within the mitochondrial matrix, the molecule enters the citric acid cycle which oxidizes the acetyl-CoA to CO_2 and reduces NAD^+ to $NADH$ and results in the production of two ATP per glucose. $NADH$ can then be used in the final stage of aerobic respiration: oxidative phosphorylation (OXPHOS). This involves the transfer of electrons from $NADH$ to the electron transport chain. As the electrons pass through the electron transport chain a proton gradient is established over the mitochondrial membrane. ATP synthase (an enzyme at the end of the electron transport chain) utilizes this proton gradient to generate ATP via chemiosmosis. The electron transport chain is an important topic for both respirometry measurements (discussed further in section 4.4) and for diffuse optical broadband measurements which can probe cytochrome C oxidase.

4.1.2 Anaerobic Respiration

Anaerobic respiration is respiration that occurs in the absence of oxygen. Anaerobic respiration must use an electron acceptor different from oxygen. As noted above, it starts the same way as aerobic respiration, with glucose going through glycolysis to form pyruvate. However, in the absence of NAD^+ in the

53

mitochondria, which is re-generated from NADH during oxidative phosphorylation, both pyruvate and NADH remain in the cellular cytoplasm. To generate additional NAD$^+$ for continued anaerobic glycolysis, pyruvate is reduced to lactate, regenerating NAD^+ from $NADH$, and allowing for the continuation of glycolysis (Eq.(4.2)) by forming the necessary NAD^+ [82]. As previously mentioned, anaerobic respiration provides less ATP per glucose molecule compared to aerobic respiration, making it an inefficient method of energy production. However, it is much faster than the oxidative phosphorylation used in aerobic respiration and does not require oxygen, making it a quicker means of reaching energy demands when the cell is under stress.

Since lactate is an end byproduct of anaerobic glycolysis, monitoring the concentration of lactate provides a surrogate measure for anaerobic metabolism. In practice, lactate concentration is a useful metric for directing care for severe sepsis, shock, blood loss, anemia and heart failures [82]. In our case, it provides a metric of metabolic stress which may be compared to optical metrics of metabolism and oxygen delivery. Since anaerobic glycolysis produces less energy (ATP) per molecule of pyruvate, to generate comparable ATP, a significantly greater consumption of pyruvate is necessary compared to aerobic respiration. Thus, pyruvate represents glycolytic capacity and is a function of glucose delivery, NAD^+ availability and pyruvate consumption. The concentration of pyruvate should therefore decrease as a result of switching to anaerobic respiration. As a result, during anaerobic respiration, the concentrations of lactate and pyruvate are anti-correlated. Therefore, by looking at the ratio of lactate to pyruvate (LPR), we can obtain a sensitive metric of anaerobic metabolism.
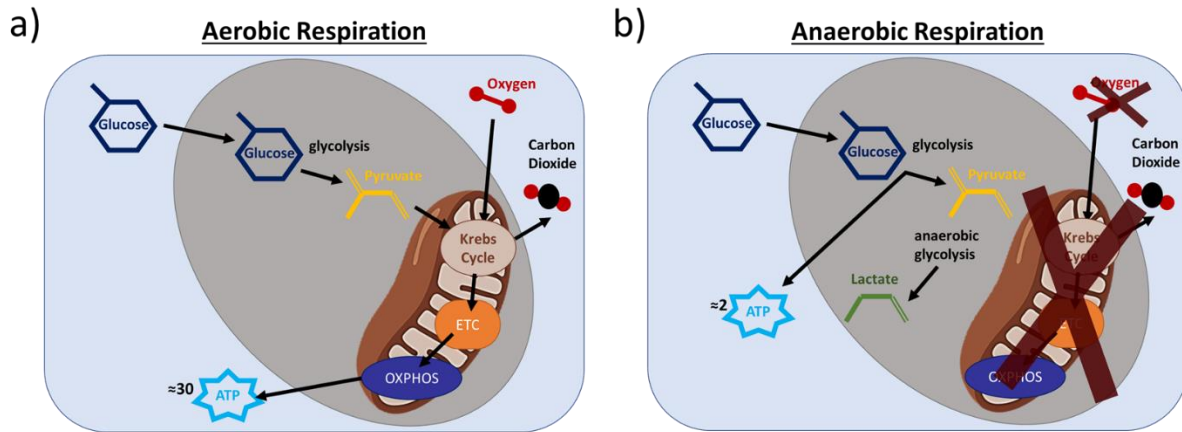
Figure 4.1 Schematics of the metabolic pathways for a) aerobic respiration and b) anaerobic respiration.

4.2 Microdialysis

Microdialysis is an invasive monitoring technique that directly samples metabolites from the interstitial fluid in the brain parenchyma [83-85]. Micetcrodialysis is primarily used clinically to assess anaerobic conditions that lead to metabolic stress, and which could lead to secondary brain insults. Unfortunately, this invasive technique requires either drilling a small hole through the skull for catheter placement or placement of the catheter through an existing craniotomy. As a result, microdialysis is only used in cases of severe brain injury, or when other neurocritical care metrics are already being collected (e.g., metrics such as intracranial pressure or brain tissue oxygen tension). Microdialysate is a continuously collected; saline (0.9% NaCl in water) is continuously perfused through the catheter by a battery-powered pump, collecting substrates through the microdialysis membrane. The resulting microdialysate fluid is collected in microvials which provide an average measurement of substrate concentration over the vial collection time. This collection procedure is necessary because a minimum volume is needed to accurately measure the concentration of the substrates within the dialysate.
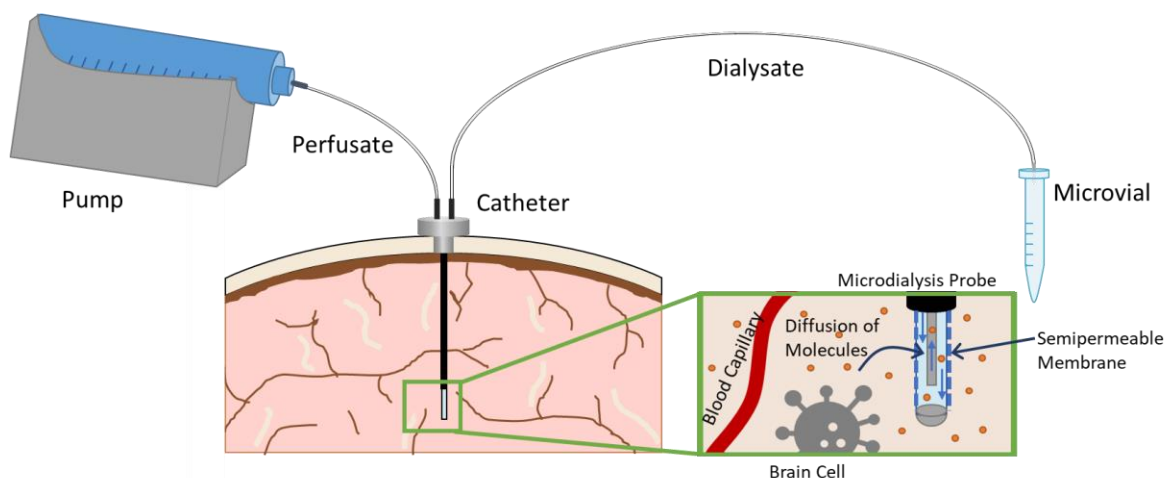
Figure 4.2 Diagram of microdialysis catheter placement and setup.

By increasing the flow rate of the perfusate, it is possible to increase the frequency of measurements. However, this approach reduces the accuracy of the measurement as the substrates are more dilute in the dialysate. In clinical practice, a flow rate of 0.3 μL/min is most typically used with hourly sampling [83]. To allow for shorter sampling periods, our lab often uses a perfusion rate of 1 μL/min, permitting sampling every 20 or 30 min [86].

Additionally, the time it takes to travel from the point of collection at the catheter to the microvial must be accounted for. This time delay can be calculated from the rate of perfusion, the length of tubing from the catheter to the microvial (ours is 220 mm), and the inner diameter of the tubing (0.15 mm) [87]. This travel-time causes a shift in timing when comparing to optical data, etc.; for our studies, we calculated the delay to be a minimum of 4 minutes, but it can be longer due to variance in the microdialysis catheter tip ([87]). While this time-delay is important to consider, it is perhaps even more important to consider the delay time for the biomarkers to make it from the cells to the microdialysis catheter. These delay times have been previously examined and empirically calculated through a comparison with microdialysis data [86].

A recent study from our lab studied these delay times and found that there was roughly a 30-60 minute delay (depending on the biomarker used) with respect to when the optical metrics first showed signs of injury [86]. This suggests that the biological processes involved in producing the biomarkers and then having them diffuse into the interstitial space where they are collected by the microdialysis catheter, occurs on comparatively long timescales following the initial hypoxic-ischemic insult detected by optical biomarkers.

Five substrates are typically measured using microdialysis; these metabolites are listed in Table 4.1, and Figure 4.3 shows the pathways by which these biomarkers can be produced. As mentioned in the previous section, lactate and pyruvate concentrations in the interstitial space are used to examine anaerobic metabolism. When they are investigated as a ratio, i.e., the lactate-pyruvate ratio (LPR), they offer a strong predictor of anaerobic metabolism and, when elevated, metabolic stress. In the same vein, we expect glucose levels to decrease rapidly with a switch to anaerobic metabolism. However, glucose levels can also be influenced by supply from blood flow and other confounding factors such as breakdown of intracellular transport mechanisms. As such, glucose is a non-specific biomarker and will not be discussed further.

Table 4.1 Summary of Microdialysis Metrics

Microdialysis Metric	Assessing
Glucose	Brain metabolism
Pyruvate	Extent of glycolysis
Lactate	Anaerobic metabolism; oxygen supply/demand mismatch
Lactate Pyruvate Ratio (LPR)	Stronger indicator of anaerobic metabolism
Glycerol	Cell membrane damage

Prolonged Ischemia/Hypoxia
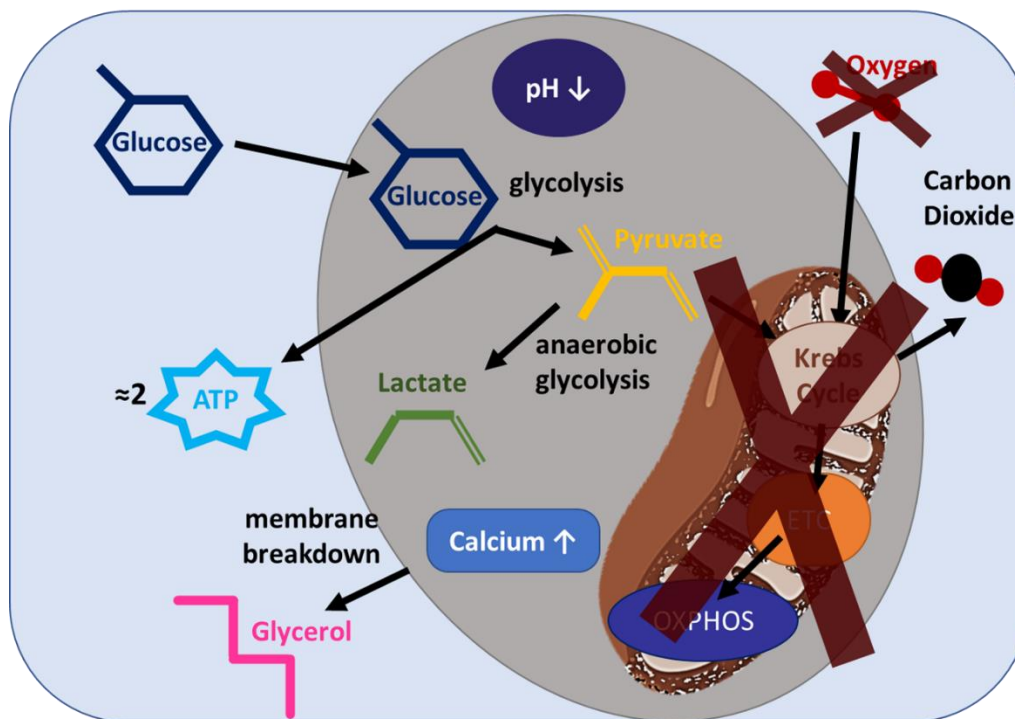
Figure 4.3 Diagram of biomarkers that can result during hypoxic-ischemic conditions. When oxygen is

not present, cellular metabolism switches over to anaerobic metabolism. This causes a

reduction in pyruvate and glucose concentrations, and an increase in lactate concentration.

While not specific to hypoxic-ischemic conditions, an increase in glycerol is seen in cases of cell

death due to injury (potentially caused by hypoxia or inflammation).

The fourth microdialysis biomarker is glycerol. Glycerol levels are known to increase due to

neurological injury due to the degradation of glycerophospholipids during apoptosis [85,88,89]. Elevated

glycerol levels have been used to predict poor neurological outcomes [86,88,89]. Normal cerebral glycerol

concentrations in humans have been reported in the range of 50-100 µM; glycerol concentrations

exceeding 80-150 µM are associated with poor outcomes in TBI patients [90,91]. In order to compare our

values (using a flow rate of 1 µL/min) with those typically reported (with a flow rate of 0.3 µL/min), we must multiply our measured concentrations by 3.3 (ratio of the two flow rates).

4.2.1 Microdialysis Procedure

The cerebral microdialysis probe used in our lab is inserted into the right frontal cortex (CMA 70 Elite, mDialysis, Sweden) at a depth of about 1-1.5 cm into the brain parenchyma. Sterile saline is then perfused at 1 µL/min for at least 30 minutes for equilibration before a baseline collection (allowing for the lines to be fully flushed). After this initial equilibration period, a baseline microdialysis sample is acquired over a time period ranging from 20-60 minutes prior to any experimental interventions. This allows for the quantification of biomarkers at normative conditions which may be compared to data taken at future timepoints. All of our microdialysis vials range in collection time from 20-60 min. The shorter time periods are used when there is expected to be greater variation in the data (i.e., during CPB when the injury insult is starting). Shorter time periods provide increased temporal resolution to identify when an injury has occurred.

An automated ISCUS Flex™ Microdialysis Analyzer (CMA 70 Elite, mDialysis, Stockholm, Sweden) was used to measure the concentrations of pyruvate, lactate, glucose and glycerol. This analyzer has the following detection limits: lactate less than 100 µM or greater than 12,000 µM; pyruvate less than 2 µM or greater than 300 µM; glycerol less than 10 µM or greater than 1500 µM; glucose less than 0.1 mM or greater than 25 mM; thus, if values were outside of this range, they were excluded from the results. This data was processed using the associated LABpilot software.

4.3 Blood Gas Collection

Arterial blood gas measurements of blood-oxygen saturation (SaO_2, %), hematocrit (Hct, %) and partial pressure of oxygen in the arterial blood (PaO_2, mmHg) were used to calculate arterial oxygen content (CaO_2, mL O_2/dL blood):

$$CaO_2 = \left(1.39\frac{mL\ O_2}{g\ Hgb}\right) \times SaO_2 \times \left(32.2\ \frac{g\ Hgb}{dL\ blood}\right) \times Hct\ +\ 0.003\left(\frac{mL\ O_2}{dL\ blood \times mmHg}\right) \times PaO_2. \quad (4.3)$$

Note, this formula considers both hemoglobin-bound oxygen (using SaO$_2$) and free dissolved oxygen (using PaO$_2$). Further, note that we explicitly converted hemoglobin (Hgb) concentration to hematocrit (i.e., $Hgb\ =\ 32.2\ Hct$). Given an expected shift from room-air PaO$_2$ values (< 100 mmHg at baseline) to PaO$_2$ > 250 mmHg during CPB support, there is a potential ~5% error in CaO$_2$ quantification when ignoring the free dissolved oxygen content.

By contrast, the partial pressure of oxygen in mixed venous blood (PvO$_2$) does not exceed 100 mmHg, even when PaO2 > 250 mmHg. Additionally, cerebral PvO$_2$ is challenging to measure accurately, tends to be well maintained through autoregulation and is significantly lower than systemic mixed venous oxygen content due to the high metabolic demand of the brain [92-94]. Thus, calculation of CvO_2 can be accurately obtained from the following formula (which does not account for free dissolved oxygen):

$$CvO_2 = \left(1.39\frac{mL\ O_2}{g\ Hgb}\right) \times SvO_2 \times \left(32.2\ \frac{g\ Hgb}{mL\ blood}\right) \times Hct. \quad (4.4)$$

The measurements of both CvO_2 and CaO_2 are used to provide an accurate measurement of oxygen extraction fraction (OEF) discussed previously in Section 2.5 as we are now accounting for the increase in dissolved oxygen. In order to give an optically measured CvO_2, we make the same approximation from Eq (2.35) and can now write CvO_2 as

$$CvO_2 = \left(44.8\frac{mL\ O_2}{dL\ blood}\right) \times Hct \times \frac{1}{\gamma}(StO_2 - (1-\gamma) \times SaO_2). \quad (4.5)$$

Using Eqs.**Error! Reference source not found.** (4.3), (4.5) and the non-approximated form of OEF (Eq. (2.34)) we can get a form of OEF which solely relies on the optically measured StO_2 and parameters measured using an arterial blood gas. This can then be written as:

$$OEF = \frac{CaO_2 - CvO_2}{CaO_2} \tag{4.6}$$

$$= \frac{CaO_2 - \left(44.8 \frac{mL\ O_2}{dL\ blood}\right) \times Hct \times \frac{1}{\gamma}(StO_2 - (1-\gamma) \times SaO_2}{CaO_2}.$$

4.4 Mitochondrial Respirometry and Reactive Oxygen Species

Mitochondrial respirometry examines the relationship between how much energy is produced from the cells compared to the consumption of oxygen. During mitochondrial respiration, water is formed when electrons, passed down the electron transport chain (ETC), reduce oxygen molecules which are the terminal electron acceptor. This permits the generation of a high proton gradient across the inner mitochondrial membrane which powers the phosphorylation of ADP by ATP synthase. The combination of these redox reactions are referred to as oxidative phosphorylation (OXPHOS). During high-resolution mitochondrial respirometry, a homogenized tissue sample is sealed within a chamber. Oxygen and specific intermediate metabolic substrates are introduced to the chamber to measure the associated respiratory capacity of individual and convergent electron flux through the ETC by monitoring the oxygen concentration present over time. We are then able to calculate the slope of the oxygen concentration to obtain the oxygen consumption. If the mitochondria is functioning properly, the oxygen concentration in the chamber should decrease. This allows for the detection of dysfunctional or damaged mitochondria as they may have an impaired ability to utilize oxygen. Mitochondria dysfunction can occur through a variety of pathways including oxidative stress, wherein excessive amounts of reactive oxygen species overwhelm the mitochondria and lead to oxidative damage. Respirometry is able to isolate individual elements of the ETC, clarifying where the breakdown in the ETC is occurring, elucidating the cause of mitochondrial dysfunction.

An Oroboros O2k FluoRespirometer was used for the measurement of respirometry data. The samples for this test were collected from the left cortex immediately after subjects were euthanized. While several different reagents are used to test mitochondrial function, I will detail three with greatest relevance to the assessment of overall mitochondrial respiratory capacity: glutamate, succinate and oligomycin, which I will talk about individually.

The addition of glutamate to the chamber tests the OXPHOS capacity supported by complex I of the ETC. Glutamate does this by indirectly supplying electrons to complex I, shown in Figure 4.4. This means that the only limitation to respiration is the rate at which ATP-synthase can transport protons back into the mitochondrial matrix. Thus, this state is defined as complex I-supported OXPHOS capacity ($OXPHOS_{CI}$).
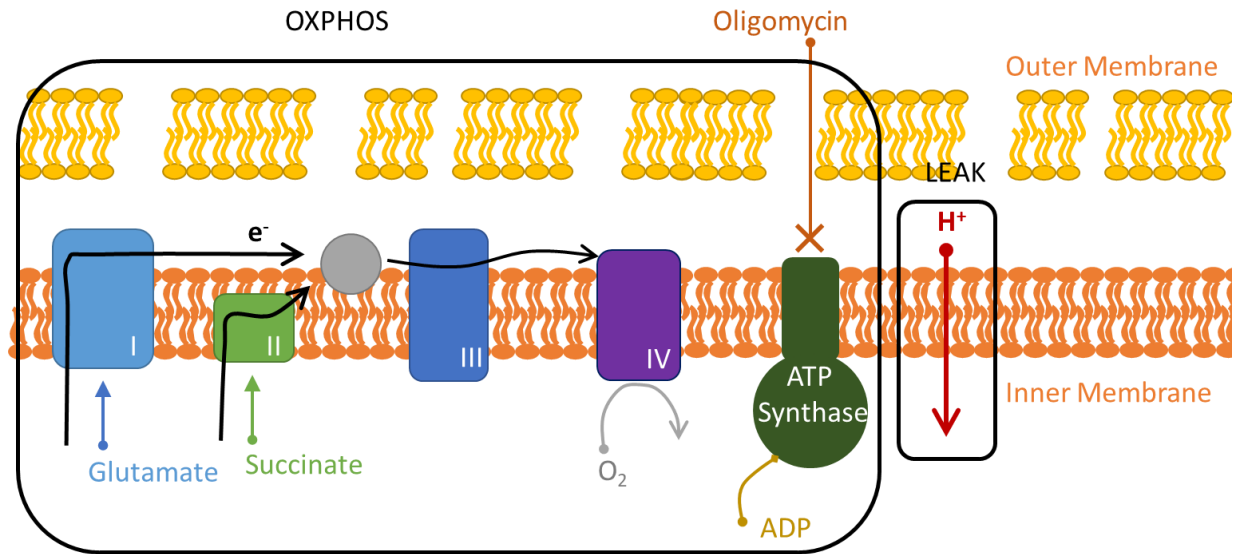
Figure 4.4 Diagram of electron transport chain capacity showing the different complexes (I – IV) and

more. OXPHOS (oxidative phosphorylation) is measured by providing first glutamate and then

succinate to the sample to determine capacity of first complex I supported OXPHOS and then

complex I + II supported OXPHOS. To measure the LEAK (amount of protons leaking through the

membrane to support respiration), oligomycin is added to shut down ATP synthase.

The next step is to add succinate to the chamber to measure convergent complex I and complex

II-supported OXPHOS capacity (shown in Figure 4.4). Complex II of the ETC is responsible for oxidizing

succinate, which supplies additional electrons to the ETC. This is measured after already supplying

glutamate, thus respiration is now only limited by the rate which ATP-synthase can transport photons

back to the mitochondrial matrix. This means that we are measuring the OXPHOS capacity supported by

both complex I and II ($OXPHOS_{CI+CII}$).

We now block ATP-synthase by adding oligomycin. This state is referred to as LEAK as no protons

can enter the mitochondrial matrix through ATP-synthase. Oxygen is only consumed to balance the

leakage of protons through the mitochondrial membrane back to the mitochondrial matrix. In this state

the oxygen consumption rate should be significantly reduced. This provides an assessment of the

efficiency of oxygen consumption to generate ATP versus to balance proton leak (i.e., energy dissipated as heat).

In order to compare the samples measured with respirometry, it is necessary to know the number of mitochondria present. This is done by utilizing citrate synthase which is a mitochondrial enzyme routinely used to measure the number of mitochondria in the tissue [95]. Citrate synthase is a reliable indicator of mitochondrial content as there is an abundance of citrate synthase in the mitochondria and it is not influenced by acute changes in the cellular conditions. Citrate synthase activity (nmol/mg/min) was measured in cortical homogenates using a commercially available kit (Citrate Synthase Assay Kit, CS0720, Sigma-Aldrich, St Louis, MO, USA) according to the manufacturer's instructions. Mitochondrial respiration was measured in left cortex homogenates (1 mg/mL) using the same instruments and substrate–uncoupler–inhibitor titration (SUIT) protocol as previously described [96-98].

Cerebral mitochondrial reactive oxygen species (ROS) generation can be measured simultaneously with the respirometry measurements using the O2k-Fluorescence LED2-Module (Oxygraph-2k, Oroboros Instruments, Innsbruck, Austria) as described previously [99]. ROS are generated when the mitochondria reduces the oxygen with only a single electron to form O_2^- instead of the typically formed water. This occurs for about 1-2% of the reduced O_2 [100]. ROS can also be generated due to inflammation or ischemia-reperfusion injury. An inflammatory process triggers the activation of immune cells (neutrophils and macrophages), which produce ROS as part of their defense mechanisms. Ischemia-reperfusion injury can also lead to excessive ROS generation as the reoxygenation of ischemic tissue can trigger an oxidative burst. It is hypothesized that ROS contributes to brain injury as the brain is sensitive to oxidative damage and can thus cause alterations in redox signaling and oxidative damage to proteins and lipids [99-101]. Previous studies from our group have found that exposure to different types of cardiopulmonary bypass have resulted in a significant increase in ROS formation [12,99]. Thus, it was

important for us to monitor if there is ROS generation as a potential for neurological injury in our models of cardiopulmonary bypass.

4.5 Pathology

Since all of the studies I worked on were terminal pre-clinical models, we were able to harvest the brain after the study was completed, specifically, 5 mm coronal sections of the right hemisphere were collected and fixed for histopathological analysis. This permits pathology to be completed on the brain tissue sample. The two techniques used in the lab examined glial fibrillary acidic protein (GFAP) and ionized calcium-binding adaptor protein-1 (IBA-1) as measures of microglial activation and nodule formation, respectively. The processes used to quantify both of the biomarkers are similar, only using different reagents.

This process starts with staining of the specimen such that only areas with either GFAP or IBA-1 are apparent. This is visualized with a diaminobenzidine (DAB) solution (one of the stains), and a microscope image is taken. Once the image is collected, deconvolution is performed, splitting the image by color with each color representing a stain associated with a biomarker. The images are then fed through a threshold filter, generating a black and white image, with black indicating the presence of the biomarker and white indicating that the biomarker is not present in that location. From this, the number of black and white pixels can be counted and the optical density (OD), which is proportional to the chromophore (biomarker) concentrations [102] can be determined.

GFAP is a protein that is found in the astroglial cytoskeleton and not found outside of the central nervous system. It is only released after cell death or injury and has been associated with increased intercranial pressure and severity of CT-diagnosed head injury [103]. The other marker, IBA-1, is a marker of microglial activation and thus brain injury as it is a protein predominately expressed in the microglia of the brain [104]. Microglia are the primary immune cells in the central nervous system and their activation

occurs when they detect a signal associated with pathogens or injury in the cellular environment. By

monitoring these two biomarkers, we derive a sense of cellular injury and death that was potentially

incurred in the injury model.

STATISTICAL METHODS

My main analyses herein concern changes and significance in time-series data. To assess these changes, I used the Wilcoxen signed-rank test and linear mixed effects modeling. Both are very common techniques used to relate repeated measures within a data set. In this chapter, I briefly introduce their underlying principles.

5.1 Wilcoxon signed-rank test

The Wilcoxon signed-rank test is a non-parametric statistical test for comparing matched (or paired) samples (e.g., comparing whether a parameter changed between two timepoints). In contrast to the t-test, the signed-rank test does not assume that the data is normally distributed. The signed-rank test assumes that the measured data parameter is continuous (e.g., like time) and that the distribution of the differences between the paired datapoints is symmetric. These assumptions are reasonable for the comparisons of paired data I performed in subsequent chapters. I used the function 'signrank' implemented in MATLAB R2022a software (The MathWorks Inc., Natick, MA, USA) to carry out this test.

An important drawback to the Wilcoxon signed-rank test arises if there are more than two repeated measures (*e.g.,* two time-points) to compare, then the test needs to be performed for each pairwise comparison. This results in a so-called multiple comparisons problem; the more inferences made (or comparisons performed), the more likely it is that one of the tests will be significant by chance. A common method to address this problem is to use a Bonferroni corrected significance level. Specifically, to test for significance at a desired significance level of α (typically 0.05), the p-value used to signal significance is α/m, where m is the number of statistical comparisons made. For example, if 20 statistical tests are performed and a significance level of 0.05 is desired, then an individual p-value of 0.05/20 = 0.0025 is used to deem significance. The Bonferroni correction is conservative, and as a result, sometimes impractically large sample sizes are needed to show significance with this method.

To test for trends in time-series data with a large number of timepoints, I thus opted to use another method to account for repeated measures within a subject called the linear mixed-effects models.

5.2 Linear mixed-effects model

Linear mixed effects models (also known as multilevel models or hierarchical models) are an extension of linear models that can account for correlations between multiple repeated measures in the data [105]. They are accordingly a powerful tool for the analysis of grouped data [106]. Linear mixed effects (LME) modeling has been widely used throughout the biomedical diffuse optics community across a diverse range of applications, such as comparing responses of different brain hemispheres [107], determining impact of hematocrit and flow on DCS measurements [22], and examining blood flow responses for multiple occlusions [108].

Just as with simple linear regression, a linear mixed-effects (LME) model linearly relates an outcome variable (*e.g.,* cerebral blood flow) to one or more predictor variables (*e.g.,* time). The relation includes subject-specific random slope and intercept effects to permit variation in the intercept and slope among individuals [109]. A classic example is LME modeling of the growth of children over time. The model separately accounts for variation in height between different children as well as variation in height over time for a single child. The outcome variable, y, is height. The predictor variable, t, is time. There is also a grouping variable, u_j, that is one for subject *j* and zero for all other subjects. The form for the LME model is then:

$$y = \left(a + b_j u_j\right) + \left(\alpha + \beta_j u_j\right)t + \varepsilon. \tag{5.1}$$

Here, a and α are fixed effects regression coefficients that are constant across all subjects; b_j and β_j are random variations from a and α for subject *j*; and ε is the residual. I used the 'fitlme' function implemented in MATLAB 2022a software (The MathWorks Inc., Natick, MA, USA) to perform the LME fit. The inputs in

the fit are the y and t data grouped by subject number. The outputs are the fitted fixed effects coefficients, a and α. In addition, the function calculates a p-value for the comparison of whether the fixed effects coefficients are different from zero. The p-values are calculated based on the assumption that the fit residuals are normally distributed.

For my research, I modeled the variation of cerebral hemodynamic metrics (*e.g.,* cerebral blood flow, oxygen extraction fraction) with time during and after cardiopulmonary bypass. To assess changes in cerebral blood flow (CBF) during cardiopulmonary bypass, for example, I defined

$$\Delta rCBF = \left(\frac{CBF}{CBF_0} - 1\right) \times 100\%, \tag{5.2}$$

where CBF_0 is the baseline value prior to the initiation of cardiopulmonary bypass (CPB). By performing LME analysis of $\Delta rCBF$ (*i.e.,* the outcome variable) versus time on bypass (*i.e.,* the predictor variable), I assessed whether *CBF* at the beginning of bypass was significantly different from baseline (*i.e.,* whether the p-value for the intercept, a, in Equation 0.1 is < 0.05). I further assessed whether CBF was changing with increasing time on bypass (*i.e.,* whether the p-value for the slope, α, in Equation 0.1 is <0.05).

To visualize the LME model, I plotted the linear regression line using the fixed effects slope and intercept, *i.e.,* a and α in Equation 0.1. This linear regression line describes the LME model's prediction of the mean of the outcome variable across the population of subjects as a function of the predictor variable. On the same plot, I also plotted the 95% confidence interval of the mean, *i.e.,* the probability is 95% that the true mean of the outcome variable across the population of subjects lies within this interval. Plotting the 95% confidence interval provides an indication of the spread of the population's outcome variable.

While most of my LME models used time as the predictor variable, I also did some models to assess whether optically measured predictor variables were associated with other neurologic injury outcome variables (e.g., I modeled the microdialysis glycerol metric against the diffuse optical StO_2 metric). For these models, subject remained the grouping variable.

CHAPTER 6

CARDIOPULMONARY BYPASS EXPERIMENTS

Cardiopulmonary bypass (CPB) is the central clinical problem I address in this thesis. In children with severe congenital heart defects who require cardiac surgical interventions in the first weeks of life, CPB is used to provide blood flow and blood oxygenation to the body during cardiac surgery. Surgical and critical care advances in CPB and other treatments in the last three decades have improved survival to adulthood from <20% to >80%, but neurodevelopmental deficits remain common [110-112]. A key barrier hindering development of new therapies to reduce brain injury derives from the fact that the mechanisms causing injury are not fully understood. Prior work has suggested that the brain is at risk of injury during and in the acute periods after CPB [110,111,113-116]. Accordingly, there is great interest in improving CPB management to reduce risk of injury. Some important variables investigated include body temperature management, duration of CPB, and perfusion strategy [12,86,117-119]. Increasing duration of CPB, for example, has been associated with poor neurological outcomes [116]. To better understand the underlying risk factors for CPB-related injury, I have used diffuse optics to quantify cerebral hemodynamic and metabolic trends during and up to 24-hours post-CPB in a neonatal swine model. In addition, since profound changes in blood hematocrit (Hct; the red blood cell volume fraction in blood) commonly occur during and after CPB, my research has also assessed the impact of Hct changes on biomarker quantification with diffuse optical techniques.

Specifically, I used frequency-domain diffuse optical spectroscopy (FD-DOS) and diffuse correlation spectroscopy (DCS) to measure cerebral tissue oxygen saturation (StO_2), cerebral blood flow (CBF), cerebral oxygen extraction fraction (OEF), and cerebral metabolic rate of oxygen ($CMRO_2$) during and after mild hypothermic CPB (wherein body temperature is cooled to 34 °C during CPB). Cooling the body is thought to protect the body from injury caused by reduced oxygen delivery and other adverse

conditions (discussed further below). In prior work, diffuse optics was deployed to quantify $CMRO_2$ reductions associated with *moderate* hypothermic CPB (body temperatures between 26 - 32 °C) and *deep* hypothermic CPB (body temperatures between 18-25 °C) [4,117,120]. Mild hypothermic CPB is an increasingly used alternative to deep hypothermic CPB because it shortens time on CPB (see below). $CMRO_2$ during mild hypothermic CPB has never been monitored. This thesis also addresses knowledge gaps associated with hemodynamic and metabolic trends in the acute period after cessation of CPB, when secondary injury presents. Lastly, I showed that accounting for changing hematocrit is important for accurate diffuse optical quantification of blood flow and oxygen metabolism during/after CPB and in general.

6.1 Background of Cardiopulmonary Bypass

CPB works as extracorporeal support. It is essentially an external heart and lung machine that provides oxygenation, controls blood flow, and diverts flow from the heart so that surgeons can operate on the heart. The CPB circuit is composed of four main parts: the reservoir (which contains additional blood volume), a pump (which controls the rate that blood is given to the patient), a heat exchanger (to manage patient temperature), and an oxygenator (to oxygenate the lungs before the blood is returned to the patient). A diagram of the CPB circuit is given in Figure 6.1.

The patient is connected to the bypass circuit through cannula which are placed in the ascending aorta and the right atrium. In this set-up, the blood enters the arterial cannula and is perfused through the body before returning to the bypass circuit through the venous cannula, thus bypassing the heart and lungs. The cannula is made of polyvinylchloride (PVC) and is reinforced with wire to prevent kinking of the circuit. Since the CPB circuit exposes the patient to exogenous blood products and artificial surfaces, CPB can trigger a cascade of systemic inflammatory responses [121-125]. Plasticizers in the PVC that are used for flexibility are potentially toxic and can leach from the tubing, causing inflammation [126]. Gravity can

be used to drain the blood back into the reservoir; however, vacuum is often applied so that smaller cannula and tubing can be used, thereby reducing circuit volume and artificial surface area.
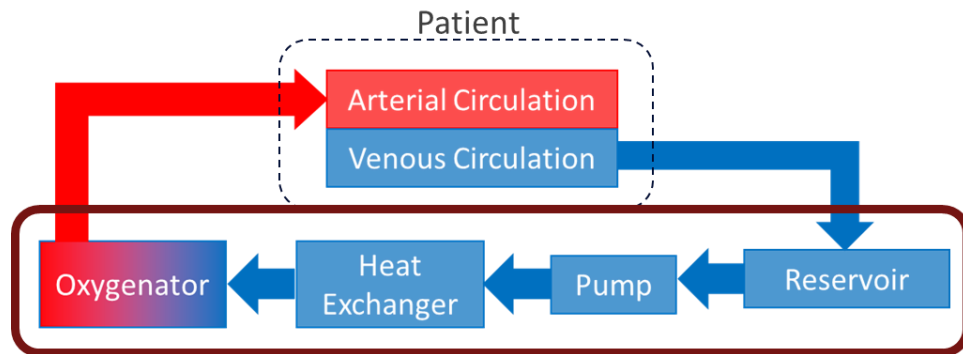
Figure 6.1 CPB Schematic. During CPB, venous blood drains into a reservoir where it is then pumped into the oxygenator through a heat exchanger before returning to the arterial circulation of the patient.

The multiple components of the CPB circuit work in tandem to deliver oxygenated blood to the patient. The reservoir collects blood that drains from the venous subsystem and stores excess blood. The reservoir enables removal of any air that may have gotten entrained as blood is pulled from the bottom of the reservoir. Vacuum can also be applied to the reservoir to assist in drainage back from the patient. The oxygenator consists of a gas exchange membrane of hollow microporous polypropylene fibers. This permits exchange of oxygen and carbon dioxide between the blood and the gas mixture. The heat exchanger typically flows counter-current to the blood flow, with the cooling or heating fluid (typically water) flowing in opposite directions within separate channels of the heat exchanger. This enables a patient to be cooled to hypothermic conditions during CPB procedures.

A risk factor for injury during CPB is the development of or dangerously low hematocrit levels (hematocrit is the red blood cell volume fraction in blood) or hemodilution [126-128]. Hemodilution can occur due to circuit priming (e.g., the CPB reservoir and plastic tubing increase the volume that blood

needs to fill, which can lower hematocrit), blood loss, IV fluid injection, and the use of plasmalyte to increase blood volume. To prevent its occurrence, hematocrit levels between 28-30% are targeted [126].

Another complication that can occur during CPB is blood clotting. The exogenous surfaces in the bypass circuit increase the risk of developing life-threatening blood clots. Patients on CPB are given heparin to promote anticoagulation, but, unfortunately, heparin also increases the risk of blood loss from bleeding. To manage this tradeoff during CPB, the activated clotting time (ACT) is monitored via IV blood sampling. After decannulation, heparin is reversed with the administration of protamine.

6.2 Hypothermia

Hypothermia is generally believed to reduce metabolism in the brain. While this effect is typically realized, it is not the only factor that improves neuroprotection [64]. There is some evidence, for example, that hypothermia reduces release of excitotoxic neurotransmitters, mitigates disruption of the blood-brain-barrier, and slows inflammatory responses [15].Together, all of these factors provide the patient with neurological protection; thus, hypothermia is one of the most robust neuroprotectant strategies in use [15]. Hypothermia is employed in a variety of clinical settings including cardiac surgery, stroke, and after cardiac resuscitation [13-15].

My focus is on the cerebral hemodynamic and metabolic effects of hypothermia during CPB. It is currently unclear per whether mild hypothermic CPB (MH-CPB) (34°C) or deep hypothermic CPB (DH-CPB) (18°C) is better for patients. DH-CPB has traditionally been used, but the use of MH-CPB has recently grown because MH-CPB requires less time on CPB, which possibly reduces the risk of injury [16]. Important questions remain unresolved about whether MH-CPB reduces cerebral metabolic demand and provides adequate neuroprotection to prevent neurological injuries acquired from CPB surgeries. Herein I use diffuse optics concurrently with cerebral microdialysis to probe the influence of mild hypothermic CPB on oxygen delivery/metabolism, and to assess neurologic injury.

6.3 Preclinical Swine Model Experiment

My experiments utilize a neonatal swine model. Specifically, I used diffuse correlation spectroscopy (DCS), frequency-domain diffuse optical spectroscopy (FD-DOS), and cerebral microdialysis methods to continuously monitor cerebral hemodynamic and metabolic changes associated with: a) the initiation of MH-CPB, b) the increase of MH-CPB time, and c) the acute time periods after MH-CPB. I also monitor elevations in the cerebral microdialysis lactate-pyruvate ratio (LPR) and glycerol metrics are biomarkers of metabolic distress and injury (see Chapter 4). Lastly, mitochondrial respirometry and histopathology analysis (see Sections 4.4 and 4.5) were performed on cerebral tissue collected after euthanasia to assess mitochondrial function and neurologic injury. In combination, the optical and invasive neuromonitoring promise to aid understanding of the physiologic mechanisms of injury during and after MH-CPB.

My experiments also show the importance of correcting for changing hematocrit levels in diffuse optical quantification of blood flow and oxygen metabolism during CPB. This work uses the model derived in Chapter 2. Specifically, I found that if the hematocrit correction is not made, then the reported oxygen metabolism change (based on diffuse optics metrics) at the onset of MH-CPB is not physiological.

6.3.1 Materials and Methods

Non-invasive FD-DOS/DCS monitoring and invasive cerebral microdialysis sampling were conducted in one-week-old, female Yorkshire swine. Subjects were placed on MH-CPB for three hours. A subset of animals was decannulated and randomized to different survival durations post decannulation. Survival durations were either eight, twelve, eighteen or twenty-four hours. Survival timepoints were selected to examine temporal changes in mitochondrial respiration and histopathological outcomes in the brain following MH-CPB. Remaining animals were euthanized following three hours of CPB support. An overview of the procedure timeline can be seen in Figure 6.2. All animal care and procedures were

approved by our Institutional Animal Care and Use Committee in accordance with the National Institutes of Health Guide for the Care and Use of Laboratory Animals.
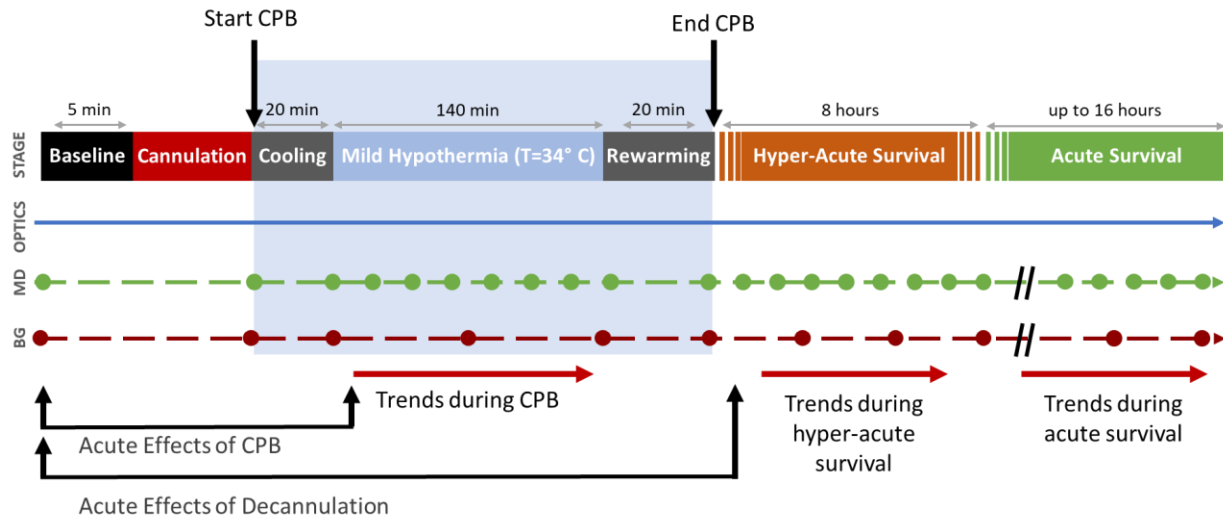
Figure 6.2 Survival study timeline. Optical metrics were continuously collected. Microdialysis was

episodically collected every 20 min during CPB and every 60 min during the survival periods.

Blood gas samples were collected every 1 hour during CPB and every 3 hours during the survival

periods. Statistical analysis was performed using three linear mixed effects models looking at

three distinct periods: mild hypothermic cardiopulmonary bypass (CPB), hyper-acute survival,

and acute survival. The intercepts from these models show the initial changes from baseline for

each period, while the slopes indicate the trends during each period.

Induction and Sedation. Subjects were anesthetized with intramuscular injection of ketamine (30 mg/kg) and inhaled isoflurane (titrated between 1-2.5% to ensure absence of withdrawal response to toe pinch) before intubation. After intubation, ventilation was maintained by volume control at a tidal volume of 10-12 mL/kg, a positive end-expiratory pressure of 5 cmH$_2$O, an inhaled fraction of oxygen (FiO$_2$) of 21%, and a respiratory rate titrated to an end-tidal CO$_2$ of 38-42 mmHg. Venous and arterial access were established in the right femoral vein and artery, allowing for intravenous anesthetic infusions of fentanyl

75

(25-200 μg/kg/min) and dexmedetomidine (0.5-2 μg/kg/min). These were titrated such that the piglet had no withdrawal response to toe pinch with 1-1.5% inhaled isoflurane.

    Monitor Placement and Baseline Acquisition. After anesthetic and respiratory stabilization, physiologic monitors were placed. Neuromonitoring consisted of a non-invasive optical probe and an invasive microdialysis catheter. The optical probe was sutured onto the left forehead and allowed continuous FD-DOS and DCS measurements (shown in Figure 6.3 The cerebral microdialysis probe was inserted into the right frontal cortex (CMA 70 Elite, mDialysis, Sweden) at a depth of about 1-1.5 cm into the brain parenchyma. The left femoral artery and vein were used for continuous arterial pressure monitoring and central venous access for medication delivery and blood gas sampling. After placement of all monitoring devices, physiologic data was continuously acquired for a "baseline" period of five minutes during which changes in medication, ventilation, and physical manipulations were halted; this approach provided an accurate measurement of the subject before MH-CPB. To maintain as much homogeneity as possible across subjects prior to MH-CPB, inhaled oxygen was kept at room air, MAP was kept between 45-65 mmHg (*i.e.,* via venous infusions of milrinone, nitroglycerin and/or nicardipine), and the end-tidal CO_2 was kept between 38-42 mmHg.
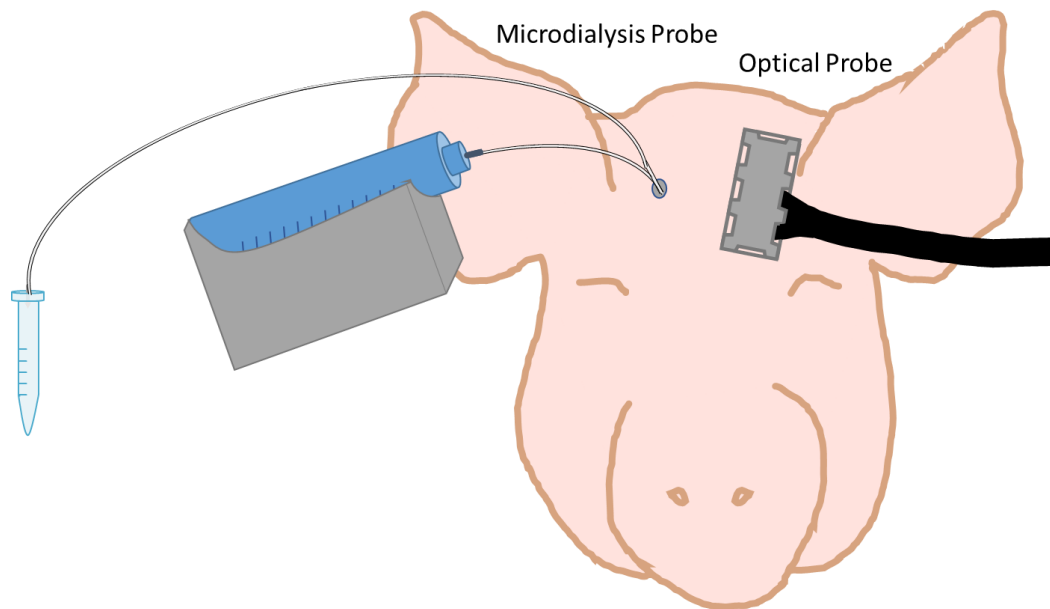
Figure 6.3 Neuromonitoring placement. Placement of invasive, microdialysis neuromonitoring on the

right hemisphere and noninvasive, optical neuromonitoring on the left hemisphere.

Initiation of Cardiopulmonary Bypass. After the baseline measurement, a heparin bolus of 4000

IU was given to the subject to prevent clot formation during cannulation. Cannulation was initiated after

the activated clotting time (ACT) was > 450 seconds in alignment with institutional practice. Cervical

cannulation was performed with placement of an 8 Fr arterial cannula in the right carotid artery and a 10

or 12 Fr venous cannula in the right external jugular vein. Following cannulation, CPB was initiated, and

inhaled isoflurane administration was ceased as 1% isoflurane was given through the CPB circuit.

Throughout the three-hour duration of CPB, flow rates were kept above 100 mL/kg/min, heparin infusion

was titrated to maintain an ACT above 450 seconds. The CPB circuit was titrated to ensure a partial

pressure of arterial oxygen (PaO_2) > 250 mmHg and MAP between 45-65 mmHg. Hematocrit was

maintained above 28% by hemoconcentration with additional donor blood. Mechanical ventilation was

maintained throughout CPB with respiratory rate reduced to 10 breaths per minute for lung maintenance.

Immediately after bypass initiation, subjects were cooled at a rate no greater than 1 °C/min over

a 20-minute period to mild hypothermia (34 °C). Subjects were maintained at 34 °C for 140 min. Twenty

minutes before the end of the three-hour CPB period, subjects were rewarmed at a rate no greater than 1 °C/min to normothermia (37 °C).

Decannulation and Post-Operative Survival. After three hours of CPB, the flow rate was reduced to zero and animals designated *a priori* for survival were decannulated. Immediately after CPB cessation, protamine was administered at 1 mg per 100 IU heparin that was given throughout the CPB period, based on current clinical guidelines, to reverse the anticoagulatory effects of heparin. The right carotid and jugular vessels were ligated, and vent settings were returned to pre-CPB values. Isoflurane was not immediately used after MH-CPB, however it was restarted if there was a response to toe pinch; fentanyl and dexmedetomidine infusions continue throughout the survival period. Animals continued to receive mechanical ventilation, intravenous sedation, and vasoactive support to sustain a MAP of 45-65 mmHg and an end-tidal CO_2 between 38-42 mmHg.

After decannulation, animals were continuously monitored for zero, eight, twelve, eighteen, or twenty-four hours prior to euthanasia (via a bolus injection of potassium chloride).

Diffuse Optical Neuromonitoring. A customized, commercial FD-DOS instrument (Imagent, ISS Inc., Champaign, IL, USA) was used to continuously measure optical properties of cortical brain tissue (seen in Figure 6.4). Twelve intensity modulated (110 MHz) diode laser sources (four 690, four 725 and four 830nm) and one photomultiplier tube detector housed in the instrument were coupled via optical fibers to the head probe (with source-detector separations of 0.7, 1.2, 1.7 and 2.2 cm). Absolute absorption and scattering coefficients were calculated using multi-distance fits of the AC intensity and phase data [4]. Cerebral oxy- and deoxy-hemoglobin concentrations ($[HbO_2]$ and $[Hb]$, respectively, in µmol/L) were quantified from tissue absorption and scattering coefficients using chromophore extinction coefficients, as previously described in Section 2.5 (note, cerebral tissue water volume fraction was assumed to be 75%) [4]. From the oxy- and deoxy-hemoglobin measurements, tissue oxygen saturation (StO_2) was

calculated as [HbO₂] / [HbO₂] + [Hb]. As detailed in Section 4.3, oxygen extraction fraction (OEF) was

derived from StO₂ and blood gas measurement of the arterial concentration of oxygen (CaO₂) using

Equation (4.6), and cerebral blood volume (CBV) was derived from FD-DOS measurements of total

hemoglobin concentration and blood gas measurements of blood hemoglobin concentration (Equation

(2.37)). Note that during MH-CPB, free arterial oxygen dissolved in the blood is not negligible, and we

accounted for this in the computation of OEF.
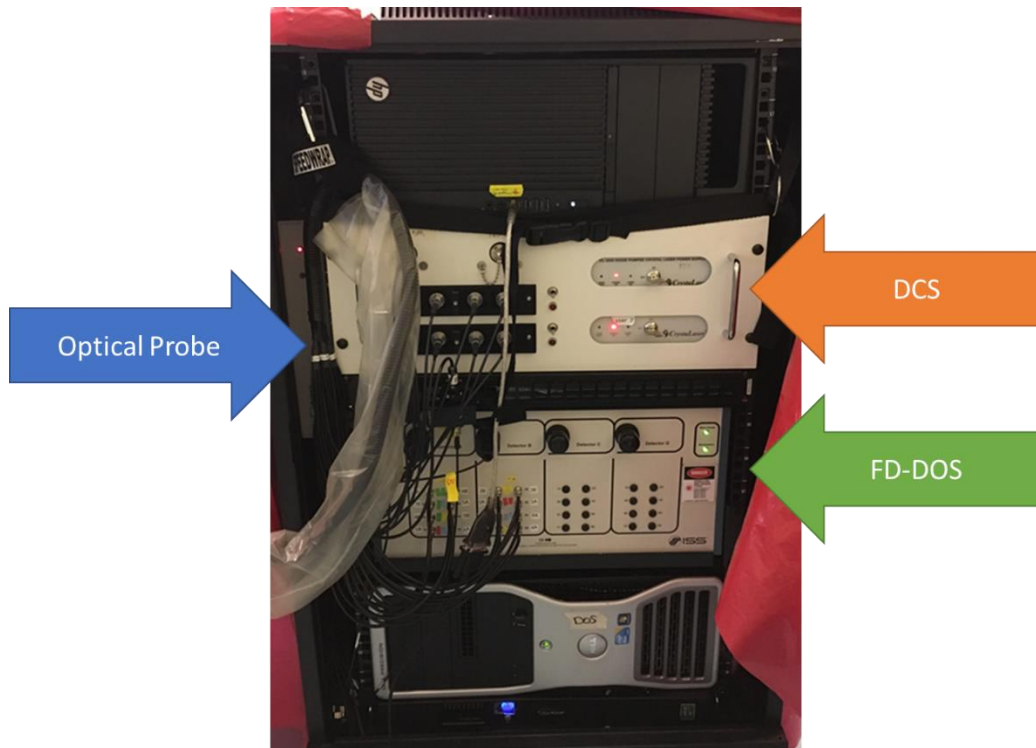
Figure 6.4 Image of assembled instrument used. A customized, commercial FD-DOS Imagent and a lab-

built DCS instrument are housed in a single cart and coupled to the same optical probe for

integrated measurements.

DCS instrumentation (discussed in Section 3.2) was integrated into the same optical probe as FD-

DOS permitting co-located measurements as previously described [4,30]. DCS measurements were made

using a source-detector separation of 1.7 cm. The source was a continuous-wave, long-coherence, 785

nm laser (Custom iBeam smart WS, TOPTICA). Two single-mode detection fibers were coupled to single-

photon-counting avalanche photodiodes (SPCM-AQ4C, Excelitas Technologies, Corp.). The $g_2(\tau)$ curve was sampled at 20 Hz and averaged over 5 seconds (100 points). From this data estimations of tissue blood flow (blood flow index, BFI), as well as the value of β in the Siegert relation were derived.

During analysis, large fluctuations in β can result from measurement artifacts (*e.g.,* motion and laser instabilities); such artifacts were observed in some animals. To account for this, we averaged the g_2 curve across the entire baseline period; BFI and β were numerically derived by fitting the g_2 curve to the semi-infinite solution of the correlation diffusion equation [30]. The tissue absorption and reduced scattering coefficients at 785 nm estimated from concurrent FD-DOS measurements (*i.e.,* via [HbO$_2$], [Hb], and a Mie scattering model [129]) were inputs in the DCS fit.

Throughout the experiment, we filtered out measurement instabilities by removing time-points where the estimated β (the first three points of the $g_2(\tau)$ curve) was less than 0.03 of the averaged, fit β value during baseline. For measurements after the baseline period, β was fixed at the value calculated during the baseline period. Cerebral blood flow (CBF) was derived from BFI using the equation we derived in Chapter 2 that accounted for changes in hematocrit, the FD-DOS measurement of the reduced scattering coefficient at 785 nm, and the blood gas measurement of hematocrit using Equation (2.59). Finally, cerebral metabolic rate of oxygen (CMRO$_2$) was calculated from CaO$_2$, OEF, and CBF using Equation (2.61) in Chapter 2. A summary of diffuse optical metrics calculations is shown in Figure 6.5.
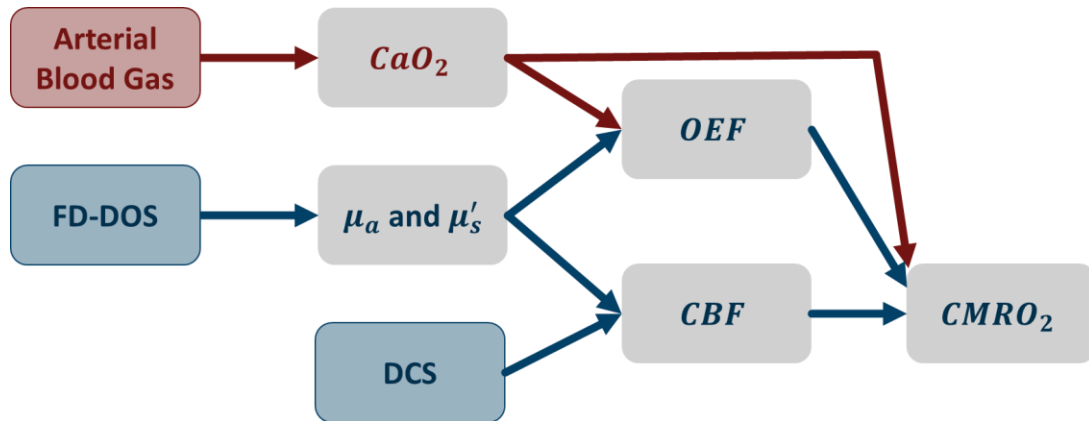
Figure 6.5 Summary of optical metrics used.

Cerebral Microdialysis. Sterile saline was perfused at 1µL/min for at least 30 minutes for equilibration before a baseline collection. Invasive cerebral microdialysis samples were collected at baseline (prior to CPB), in twenty-minute time intervals during CPB, and in sixty-minute time intervals during the survival period after decannulation. From these samples, the concentrations of pyruvate, lactate, glucose, and glycerol were measured using an automated ISCUS Flex™ Microdialysis Analyzer (CMA 71 Elite, mDialysis, Stockholm, Sweden), and data was processed using the associated LABpilot software. Data was excluded if it fell outside of the measurable range specified by the microdialysis analyzer (*i.e.*, Lactate less than 100 µM or greater than 12,000 µM; Pyruvate less than 2 µM or greater than 300 µM; Glycerol less than 10 µM or greater than 1500 µM; Glucose less than 0.1 mM or greater than 25).

Blood Gas Collection. We collected arterial blood gas samples at baseline, once every hour during the bypass period, and once every three hours during the survival period (Fig 1). Immediate analysis of blood gas samples was completed using a blood gas analyzer (GEM 3000, Instrumentation Laboratory).

Mitochondrial Respirometry. An Oroboros O2k FluoRespirometer was used for the measurement of respirometry data as previously discussed in Section 4.4. The samples for this test were harvested from

the left cortex after subjects were euthanized. This technique enables detection of dysfunctional or damaged mitochondria, which can then be compared to results from the optical data.

Histopathology. Five mm coronal sections of the right hemisphere were collected after euthanasia and fixed for histopathological analysis. This permitted the examination of glial fibrillary acidic protein (GFAP) and ionized calcium-binding adaptor protein-1 (IBA-1) as measures of microglial activation and nodule formation, respectively as described in Section 4.5.

Statistical Analysis. Statistical analyses were carried out using MATLAB 2022a (The MathWorks Inc., Natick, MA, USA). All statistical tests were two-sided, and a p-value < 0.05 was used to deem significance. Summary statistics are presented using medians and interquartile ranges.

First, we assessed the average impact of MH-CPB on MAP, arterial blood gas metrics, cerebral optical metrics, and cerebral microdialysis biomarkers. For each animal in the cohort and for each measurement parameter, we computed the mean across the baseline period (*i.e.,* the 5-minute window just prior to CPB cannulation) and the mean across the MH-CPB period (*i.e.,* the 140-minute window of constant temperature and CPB flow rate). Wilcoxon signed-rank tests were then used to assess differences between the baseline and MH-CPB periods. Of particular interest from these assessments was whether MH-CPB was accompanied by decreased $CMRO_2$ and CBF.

Next, we used linear mixed effects regression analyses to investigate the presence of linear temporal trends in MAP, Hct, CaO_2, cerebral optical metrics, and cerebral microdialysis biomarkers for each experimental period after baseline (*e.g.,* MH-CPB, survival). Prior to performing the regressions, MAP, Hct, CaO_2, and cerebral optical metrics were first block averaged across time windows that corresponded to each microdialysis sampling period (*i.e.,* across 20-minute windows prior to microdialysis collection during CPB, and across 60-minute windows prior to microdialysis collection during survival; see Figure 6.2). Regressions were then performed on the relative changes of each parameter from baseline.

The relative changes were computed using Eq. (5.2) from Section 5.2. The linear mixed-effects analyses of temporal trends include random slope and intercept effects to account for within-subject correlation of repeated measures. Linear fits versus time for each parameter were performed during a) mild hypothermic CPB (20-160 min during CPB); b) hyper-acute survival (0-8 hours post decannulation); and c) acute survival (8-24 hours post decannulation) as shown in Figure 6.2. The cooling (0-20 min CPB) and rewarming (160-180 min CPB) periods were excluded due to the non-linear effects of temperature change. Note, we sought to differentiate the hyperacute and acute survival periods based on the hypothesis that the linear trends are different immediately after decannulation than they are at a longer time after decannulation. The eight-hour post decannulation timepoint used to divide the hyperacute and acute survival periods was selected based on a sensitivity analysis that is described in detail in Appendix 6.5.3.

For each linear model, the p-value of the y-intercept tests whether the percentage change from baseline significantly differs from 0 at the start of each experimental period, and the p-value of the slope tests whether there is a significant change in the parameter during the experimental period.

For data collected after euthanasia (i.e., respirometry and pathology), only a single data point is obtained for each subject, thus a linear mixed effects model is not appropriate. In these cases, an analysis of variance (ANOVA) was performed using MATLAB 2022a to determine if there is a statistical difference between groups.

6.3.2 Results during and after MH-CPB

Twenty-eight piglets (3.5-5.5 kg) were successfully placed on CPB for 3 hours and maintained at 34°C for 140 minutes. In 19/28 animals, CPB support was discontinued, animals were decannulated, and randomized to eight (n=5), twelve (n=5), eighteen (n=4) or twenty-four (n=5) hours of monitoring post-decannulation. The remaining nine animals were euthanized following three hours of CPB support.

Continuous FD-DOS measurements of wavelength-dependent tissue optical absorption and scattering coefficients, and continuous DCS measurements of blood flow index were successfully collected throughout the MH-CPB period as well as the survival period in all animals. Overall, an average of 7% of DCS data was excluded from the MH-CPB period and about 4% were excluded from the survival period.

One animal did not have blood gas analysis due to equipment malfunction, limiting the possibility for hematocrit corrected optical measurements; therefore, no blood gas data or optical properties requiring blood gas data are included in the analysis for this animal. One animal did not have MD collection for the first hour of experiment due to battery failure in the MD pump. Additionally, MD data was not included if it fell above or below the limits set by mDialysis software. This meant that during the bypass period, only 78% (n=173) of glucose values, 83% (n=183) of glycerol values and 78% (n=172) of LPR values were included, and during the survival period, only 75% (208) of glucose values, 95% (n=262) of glycerol values and 91% (n=250) of LPR values were included. Of the removed data, 13% were below the detection limit while 4% were above the threshold limit of the mDialysis software.

Mild Hypothermic Cardiopulmonary Bypass (MH-CPB) Period. The means of each parameter across the baseline period and across the MH-CPB period were compared. Summary results and statistics are listed in Table 1, and all differences between parameters reported in-text reflect the relative change in the parameter as a percentage of baseline (*i.e.,* Equation (5.2)). We observed a large increase in hematocrit (+48%, p<0.001) during MH-CPB. This increase in hematocrit, as well as a modest increase in SaO_2 (+2.6%, p<0.001), produced a substantial increase in CaO_2 (+61%, p<0.001). In addition, OEF (-12%, p<0.001) and CBF (-22%, p=0.03) decreased, and StO_2 (14%, p<0.001) increased during the MH-CPB period. Interestingly, there was no change from baseline in $CMRO_2$ during MH-CPB (p=0.8). There were also no changes in the microdialysis injury biomarkers.

Table 6.1 Summary statistics of baseline and bypass periods.

Modality	Parameter	Baseline	Mild Hypothermic CPB	p-value
	Length (cm)	37 (36, 38), (n=27)	-	-
	Weight (kg)	4.3 (4.1, 4.5), (n=28)	-	-
	MAP (mmHg)	61 (54, 71), (n=28)	63 (57, 71), (n=28)	0.3
Blood Gas	Hct (%)	23 (21, 27), (n=28)	34 (33, 36), (n=28)	**<0.001**
	CaO_2	11 (9, 12), (n=27)	16 (15, 16), (n=27)	**<0.001**
	SaO_2 (%)	97 (97, 98), (n=27)	100 (99.9, 100), (n=27)	**<0.001**
	paO_2 (mmHg)	91 (84, 96), (n=28)	257 (239, 270), (n=28)	**<0.001**
	Glucose (mg/dL)	105 (80, 117), (n=28)	152 (121, 187), (n=28)	**<0.001**
	Lactate (mmol/L)	1.2 (1, 1.6), (n=28)	2.2 (1.7, 2.9), (n=28)	**<0.001**
Optics	StO_2 (%)	54 (50, 56), (n=28)	60 (57, 64), (n=28)	**0.001**
	OEF (%)	62 (57, 66), (n=27)	55 (50, 59), (n=27)	**0.002**
	rCBF (%)	100, (n=28)	63 (37, 89), (n=28)	**0.002**
	$rCMRO_2$ (%)	100, (n=27)	88 (58, 132), (n=27)	0.4
	CBV (μL/g brain tissue)	56 (51, 68), (n=28)	48 (41, 53), (n=28)	**<0.001**
	THC (μM)	71 (65, 83), (n=28)	83 (79, 92), (n=28)	**<0.001**
Microdialysis	LPR	17 (15, 20), (n=20)	16 (12, 21), (n=26)	0.12
	Glycerol (μM)	21 (17, 31), (n=21)	22 (18, 24), (n=28)	0.7
	Glucose (μM)	12 (8, 19), (n=20)	11 (6, 15), (n=27)	0.17

Summary parameters are reported as median (IQR). Reported p-values are associated with Wilcoxon Sign-Rank tests between Baseline and MH-CPB period for each parameter. MAP = mean arterial pressure, Hct = hematocrit, CaO_2 = arterial concentration of oxygen, SaO_2 = arterial blood-oxygen saturation, paO_2 = partial pressure of oxygen in the arterial blood, StO_2 = tissue oxygen saturation, OEF = oxygen extraction fraction, rCBF = relative cerebral blood flow, $rCMRO_2$ = relative cerebral metabolic rate of oxygen, CBV = cerebral blood volume, THC = total hemoglobin concentration, LPR = lactate-pyruvate ratio.

We next investigated temporal trends in the measured systemic and cerebral physiologic parameters during MH-CPB (Table 2). OEF decreased from baseline at the start of MH-CPB (-12%, p<0.001) and then increased with time (+1.9%/h, p<0.001). This finding was mirrored by CBV, *i.e.,* CBV decreased from baseline at the initiation of MH-CPB (-21%, p<0.001) and then increased with time (+2.1%/h, p=0.011). Interestingly, the trends in CBF did not mirror CBV; CBF initially decreased at the start of MH-CPB (-22%, p=0.03), but then it decreased further with time (-5.4%/h, p=0.03). The initial $CMRO_2$ at the start of MH-CPB was not different from baseline, and $CMRO_2$ decreased with time thereafter (-6.2%/hr, p=0.02). Note, the $CMRO_2$ decrease with time was not sufficient to cause the mean $CMRO_2$ across MH-CPB to be significantly different from baseline (see Table 6.1 analysis). In total, these results demonstrate

that MH-CPB has both an acute (immediate) and sustained impact on cerebral physiology. However, no

significant changes in cerebral microdialysis biomarkers were observed.

Table 6.2 Trends during the mild hypothermic cardiopulmonary bypass (MH-CPB) period.

Parameter	LME y-intercept			LME Slope		
	Value (%)	95% CI	p-value	Value (%/h)	95% CI	p-value
ΔrMAP	+8	(-2. 18)	0.1	-1.0	(-4.1, 2.2)	0.6
ΔrHCT	+54	(43, 64)	**<0.001**	-2.1	(-5.0, 0.7)	0.14
ΔrCaO$_2$	+61	(49, 72)	**<0.001**	-1.5	(-4.4, 1.4)	0.3
ΔrStO$_2$	+14	(8, 19)	**<0.001**	-1.5	(-3.1, 0.2)	0.08
ΔrOEF	-12	(-17, -7)	**<0.001**	+1.9	(0.1, 3.7)	**0.04**
ΔrCBF	-22	(-42, -2)	**0.03**	-5.4	(-10.2, -0.5)	**0.03**
ΔrCMRO$_2$	+3	(-18, 24)	0.8	-6.2	(-11.5, -1.0)	**0.02**
ΔrCBV$_{Hct}$	-21	(-26, -16)	**<0.001**	+2.1	(0.49, 3.7)	**0.011**
ΔrTHC	+19	(15, 22)	**<0.001**	+0.86	(-0.49, 2.20)	0.2
ΔrLPR	+48	(-37, 134)	0.3	-24	(-64, 16)	0.2
ΔrGlycerol	9	(-196, 215)	0.9	+48	(-83, 178)	0.5
ΔrGlucose	+47	(-25, 120)	0.2	-18	(-57, 21)	0.4

Results of the univariate linear mixed effects (LME) models during MH-CPB accounting for within-subject correlation of repeated measures. 95% CI is the 95% confidence interval for the stated fixed-effect coefficient in the linear mixed-effects model. Significant p-values are bolded for clarity.

Impact of Hct Changes on CBF Measurements. We observed a substantial effect on diffuse optical

quantification of CBF and CMRO$_2$ after accounting for hematocrit changes (Figure 6.6). During MH-CPB,

uncorrected CBF did not differ from baseline; however, after correction, CBF was significantly lower than

baseline (as reported above). A similar downwards shift was observed in CMRO$_2$; uncorrected CMRO$_2$

increased significantly from baseline (+50%) at the start of MH-CPB, but after correction, no significant

difference was observed. The correction did not impact the direction of significant temporal trends. Both

corrected and uncorrected CBF and CMRO$_2$ demonstrated a significant decrease with increasing MH-CPB

time. Notable, the corrected values are much more physiologically sensible that the uncorrected values,

especially CMRO$_2$.
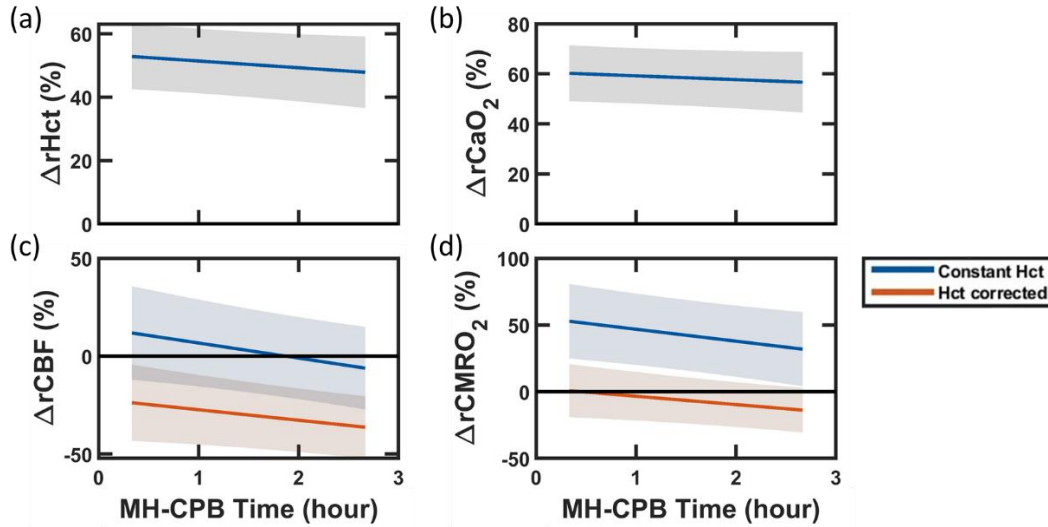
Figure 6.6 Impact of Hematocrit on Blood Flow and Oxygen Metabolism During Mild-Hypothermic

Cardiopulmonary Bypass (MH-CPB). Linear mixed effects regression analyses of percent changes

from baseline in (a) hematocrit (Hct), (b) arterial concentration of oxygen (CaO$_2$), (c) cerebral

blood flow (CBF), and (d) cerebral metabolic rate of oxygen (CMRO$_2$) during the 140 minutes of

MH-CPB. The linear fit (solid lines) and 95% CI (shaded regions) across the 28 swine are shown in

all plots. In panel (c), CBF was derived in two ways: 1) from DCS measurements assuming

constant Hct (blue line), and 2) from DCS measurements, blood gas Hct measurements, and FD-

DOS scattering measurements using equation 8 (red line). In panel (d), CMRO$_2$ was derived from

Equation (2.61) using 1) the constant Hct CBF measurements (blue line), and 2) the "Hct

corrected" CBF measurements (red line).

Hyper-Acute and Acute Survival Period. In the animals that were monitored after cessation of CPB

support (i.e., after decannulation), the trends in measured systemic and cerebral physiologic parameters

were analyzed from zero to eight hours post decannulation and from eight to 24 hours post

decannulation. These timepoints were chosen because we observed that some of the parameters,

(ΔrStO₂, ΔrOEF, ΔrCBF, ΔrCMRO₂, ΔrTHC, ΔrGlycerol) returned, or started to return, to baseline values during the twenty-four-hour survival period (Figure 6.7).
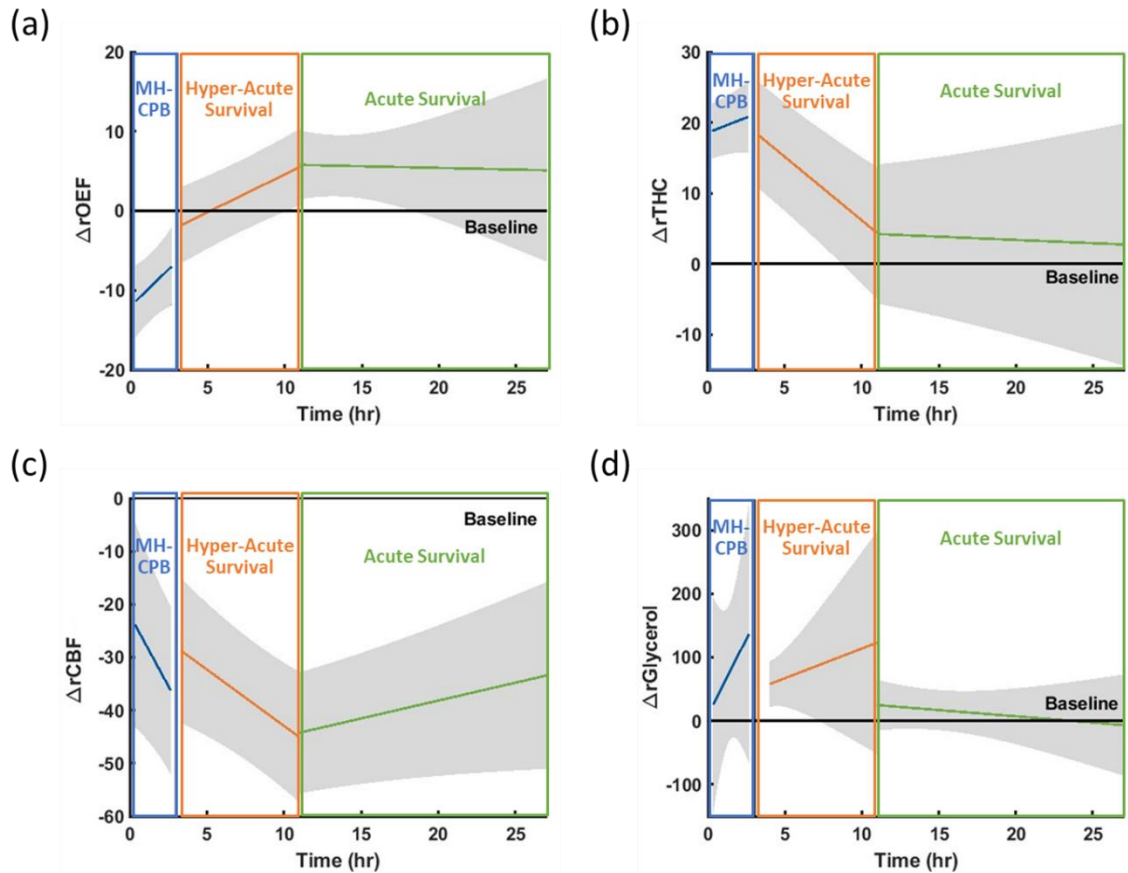
Figure 6.7 Linear Mixed Effects Models for ΔrOEF, ΔrCBF, ΔrTHC and ΔrGlycerol.

Summary results of the piecewise linear mixed effects models for the two periods are listed in Table 6.3 and Figure 6.7. A significant elevation in glycerol was observed at the beginning of the "hyper-acute" survival period (0-8 hours post-CPR; +58%, p=0.002), but glycerol levels returned to baseline in the later "acute" survival period (8-24 hours post-CPB). Diffuse optical parameters also demonstrated disparate trends between hyper-acute versus acute survival periods. Specifically, trends during the hyper-acute period matched the trends during the MH-CPB period discussed, *i.e.,* OEF increased while CBF and CMRO₂ decreased over time. In the subsequent acute survival period, however, significant temporal changes were no longer present in all the variables except CBF, which increased over time. The increases

observed during MH-CPB in both hematocrit and CaO_2 were sustained throughout the hyper-acute and acute survival periods; both parameters remained significantly higher than baseline. No significant elevation of metabolic distress biomarker (LPR) was observed.

Table 6.3 Trends during the hyper-acute (0-8 h) and acute (8-24 h) survival periods.

Parameter	Time Post Decannulation	LME y-intercept			LME Slope		
		Value (%)	95% CI	p-value	Value (%/h)	95% CI	p-value
ΔrMAP	0-8 h	+12	(-5, 29)	0.2	+0.6	(-1.2, 2.4)	0.5
	8-24 h	+13	(1, 24)	0.03	-0.0	(-0.1, -0.0)	<0.001
ΔrHct	0-8 h	+53	(50, 55)	<0.001	-0.3	(-1.2, 0.7)	0.6
	8-24 h	+50	(48, 53)	<0.001	-0.2	(-0.5, 0.0)	0.09
ΔrCaO$_2$	0-8 h	+60	(49, 71)	<0.001	-0.5	(-0.6, -0.4)	<0.001
	8-24 h	+56	(45, 67)	<0.001	-0.5	(-0.7, -0.4)	<0.001
ΔrStO$_2$	0-8 h	+7	(2, 11)	0.003	-1.0	(-1.4, -0.6)	<0.001
	8-24 h	-1	(-5, 2)	0.4	-0.1	(-0.7, 0.6)	0.9
ΔrOEF	0-8 h	-2	(-7, 3)	0.4	+0.9	(0.5, 1.4)	<0.001
	8-24 h	+6	(1, 10)	0.009	0.0	(-0.8, 0.8)	0.9
ΔrCBF	0-8 h	-28	(-42, -14)	<0.001	-2.1	(-3.6, -0.7)	0.004
	8-24 h	-44	(-56, -33)	<0.001	+0.7	(-0.0, 1.4)	0.05
ΔrCMRO$_2$	0-8 h	+8	(-10, 27)	0.4	-3.0	(-5.0, -0.9)	0.004
	8-24 h	-13	(-27, 1)	0.05	+0.6	(-0.1, 1.3)	0.1
ΔrCBV	0-8 h	-20	(-28, -11)	<0.001	-1.0	(-1.5, -0.5)	<0.001
	8-24 h	-28	(-38, -18)	<0.001	0.0	(-0.5, 0.5)	0.95
ΔrTHC	0-8 h	+19	(11, 26)	<0.001	-1.8	(-2.5, -1.1)	<0.001
	8-24 h	+4	(-6, 14)	0.4	-0.1	(-0.7, 0.5)	0.8
ΔrLPR	0-8 h	-5	(-40, 29)	0.8	+5.0	(-0.7, 10.7)	0.08
	8-24 h	+2	(-39, 43)	0.9	+4.0	(-11.7, 19.6)	0.6
ΔrGlycerol	0-8 h	+48	(7, 89)	0.02	+9.3	(-14.7, 33.3)	0.4
	8-24 h	+25	(-15, 64)	0.2	-2.0	(-8.0, 4.1)	0.8
ΔrGlucose	0-8 h	-0	(-94, 93)	>0.99	+2.1	(-21.6, 25.8)	0.9
	8-24 h	+60	(-101, 221)	0.5	-2.0	(-8.0, 4.1)	0.5

Results of the univariate linear mixed effects models for optical parameters versus time post MH-CPB. The survival period was split into two phases, hyper-acute and acute survival, separated at eight hours post-decannulation (the eight-hour time point choice is justified in supplemental material).

6.3.3 Discussion

In this study we characterized the effects of MH-CPB on cerebral physiological parameters quantified non-invasively by diffuse optics and invasively by cerebral microdialysis in a neonatal swine model. A novel aspect of our optical study was the implementation of hematocrit corrections in the quantification of

cerebral oxygen metabolism; these corrections were important because hematocrit varied substantially in this study. Overall, mild-hypothermia did not reduce cerebral metabolism during cardiopulmonary bypass in this model. An elevation in cerebral glycerol, a biomarker of injury, was observed in the first eight hours following MH-CPB; however, this did not correspond to elevation in biomarkers of metabolic distress; thus, its elevation indicates an alternate, possible inflammatory, origin of injury. This injury may be associated with temporal changes of optically-measured cerebral metabolic parameters during MH-CPB that also persisted for eight hours following MH-CPB. Our results suggest that, during this hyper-acute period, the brain may be at increased vulnerability to secondary insults.

Improved Quantification of CMRO$_2$: Impact of Hematocrit. In many clinical settings, substantial changes in hematocrit occur that can influence interpretation of diffuse optical CBF and CMRO$_2$ measurements. We observed a significant increase in hematocrit at the start of MH-CPB (+54% relative to baseline) which remained high throughout the entire 24-hour survival window. In addition to CPB procedures, hemoconcentration occurs with extracorporeal membrane oxygenation (another form of life-support) and with blood transfusions. Hematocrit levels can also be altered when there is severe blood loss, or when an excess of fluids is given to treat severe dehydration. In all these scenarios, utilization of an optical CBF and CMRO$_2$ that accounts for hematocrit fluctuations is important for accurate characterization of longitudinal changes.

Using conventional DCS approaches that did not account for hematocrit changes (i.e., $CBF \propto BFI$), we observed a +2% increase in CBF at the start of MH-CPB compared to baseline. The effect of hematocrit on CBF quantification has been examined previously via experimental and theoretical work with conflicting results [22,23]. When effects of increasing hematocrit were examined *in vitro*, Sathilaingam, et al. found that DCS measured CBF decreased with increasing red blood cell concentration in their phantom models; specifically the deduced the relationship: $CBF \propto BFI/(1 - 1.8 \times Hct)$ [22].

We explored the use of this correction as well as the one discussed above. Note, this correction (to lowest order) will be proportional to Hct rather than inversely proportional (as is the case for our primary model). Using the correction from [22], we obtained a 75% increase in CBF from baseline and a 145% increase in CMRO$_2$ from baseline at the beginning of MH-CPB. This sustained increase in CBF was deemed non-physiologic as it would result in hyperemic injuries (edema and/or hemorrhage) that were not observed [130-132]; similarly, the enormous increase of CMRO$_2$ was also non-physiologic. By contrast, our approach (which ultimately derives from the model of Boas, et al. that gave $CBF \propto BFI/Hct$ [23]) generated a plausible decrease in CBF at the onset of MH-CPB (-22%). A reduction of CBF with reduction in temperature has been reported during hypothermic CPB [4,120]. Overall, our approach gave biomarker metrics that are consistent with physiologic expectations. Future work is needed to understand the origin of the discrepancies of our approach compared to approach based on the *in vitro* measurements, but this is beyond the scope of my present research. (For example, it might be that some of the parameters in the relation between CBF and BFI (Equation (2.59)) assumed constant herein, such as α_{shear} and vol_{RBC}, are altered with hemoconcentration in the *in vitro* model.)

In addition to influencing CBF estimations, proper accounting for hematocrit and the free dissolved oxygen content also impacted characterization of changes in CaO$_2$ and OEF parameters in the overall estimation of CMRO$_2$. Had we neglected changes in PaO$_2$, Hct and CaO$_2$ from baseline, as in prior work, then our data analysis would have generated a significant underestimation of the contributions of CaO$_2$ and OEF during CPB. With this oversimplification, we obtained a significant increase in CaO$_2$ (+61%) and a reduction in OEF (-12%) at the start of MH-CPB. Moreover, combining these parameters with uncorrected CBF estimations resulted in a 53% increase in CMRO$_2$ from baseline at the start of MH-CPB that does not agree with physiologic estimations of the effects of hypothermia [117,120,133]. However,

using Fick's law with the proper corrections, the $CMRO_2$ values at the start of MH-CPB did not significantly differ from baseline at the start of MH-CPB.

As noted above, in the future, additional validation of our novel approach against gold standard measurements of CBF and $CMRO_2$ is desirable.

Effects of Mild-Hypothermic Cardiopulmonary Bypass. As discussed above, we did not observe a significant reduction in $CMRO_2$ at the start of MH-CPB; this finding contrasts with our hypothesis that mild hypothermia would reduce $CMRO_2$. Cooling has been observed to reduce metabolic demand of tissue, thus reducing $CMRO_2$ [13,15,64]; however thermoregulatory processes could account for compensatory maintenance of $CMRO_2$ at mild-hypothermic temperatures where muscles are contracting to produce heat through friction (*i.e.*, shivering), requiring additional energy [14]. The lack of reduction in $CMRO_2$ could indicate a need to cool further than 34°C in order to reduce metabolism and suppress inflammatory cascades as a means of neuroprotection [14].

During MH-CPB, we found a decrease over time in the non-invasive optical estimates of CBF and $CMRO_2$, and an increase of OEF and CBV. Increasing OEF indicates a growing imbalance between oxygen delivery and demand with increasing time on CPB. The lack of elevation of biomarkers of cerebral metabolic distress suggests that, despite growing mismatch, for the three-hour duration used in our experimental model, oxygen supply met demand (for longer CPB times, however, this may no longer be the case if the observed CBF and OEF trends persist). In addition to metabolic distress, recent work has highlighted the role of inflammation and reactive oxygen species generation as mechanisms of neurological injury during MH-CPB [12]. Thus, the reduction in CBF with corresponding increase in OEF may serve as a biomarker of this injury process. Of note, the observed increase in CBV over time during MH-CPB, despite decreasing CBF, may also be indicative of inflammation.

Cerebral Metabolism and Injury during Post-CPB Survival (0-24 h). An elevation in cerebral glycerol, a biomarker of injury, was observed in the first eight hours following MH-CPB; however, this did not correspond to elevation in biomarkers of metabolic distress. As discussed above, this lends support to an alternate, possible inflammatory, origin of injury. While this injury was observed *following* CPB, corresponding trends in cerebral physiologic parameters suggest that this injury process was initiated *during* CPB and continued for eight hours following decannulation (termed "hyper-acute" survival in our work). During this period, consistent with temporal trends observed during MH-CPB, OEF significantly increased, and CBF and $CMRO_2$ significantly decreased over time. In the subsequent 8-24 hour "acute" survival period, glycerol was no longer elevated, and these cerebral physiologic trends were no longer present. In fact, CBF demonstrated an inflection and began to increase over time. These results suggest that CPB-associated injury mechanisms persisted for eight hours following MH-CPB and highlights this period as a critical window of neurological vulnerability.

In a previous study applying diffuse optical quantification during CPB in neonates with severe congenital heart defects who underwent either normothermic or mild hypothermic (>22°C) CPB, a significant decrease in CBF as well as an increase in OEF and CaO_2 was also seen following CPB [134]. However, our observations differed in that after decannulation, OEF was not significantly different from baseline values, although it did continue to rise during the hyper-acute period, becoming significantly different from baseline values by eight hours. Differences in OEF with our study may be a result of impaired oxygenation at baseline in clinical subjects, while our model used healthy animal subjects. The increase in OEF during the hyper-acute survival period and the significant elevation during the acute survival period are consistent with prior evidence of the timing of an inflammatory response, as it takes time for oxygen demand to increase [121,135]. Concurrent MAP elevation with diminished CBF during this

period also suggests increased intracranial pressure that may occur secondary to inflammation, potentially due to the heparin-protamine interaction or impaired cerebral autoregulation [136-138].

Microdialysis. These findings are discussed further in Appendix 6.5.1. However, as a brief summary, microdiaylsis measurements of metabolic distress or neurological injury did not reach currently accepted thresholds (LPR >40 and glycerol >30 µM) [86], thus we cannot conclude there was injury from these metrics. We did see a trending increase in glycerol with increased CPB duration, which could indicate that if time on CPB was extended, there is a higher chance of injury.

Pathology. The pathology findings are discussed in depth in Appendix 6.6.2. In summary, there was not statistical differences found in the pathology data to indicate that there was neurologic injury from CPB. There were trends that could indicate a return towards baseline values around 8-12 hours post, which further supports the optically found results.

6.4 Limitations

There are several assumptions made in Eq. (2.59) the calculation of CaO_2 and OEF that could affect results. We do not have a direct measure of SaO_2 or SvO_2 entering or leaving the brain, instead we have assumed a systemic measurement of SaO_2 is equivalent to the SaO_2 entering brain tissue. This is most likely an accurate assumption during the CPB period where SaO_2 is close to 100%, however, it may not be as accurate during the post CPB period where systemic SaO_2 may be lower than what is provided directly to the brain. This effect would then cause the calculated OEF to be lower than its true value.

Other study limitations include the fact that monitoring was only carried out for twenty-four hours post CPB, potentially missing secondary injuries that often occur later in the recovery [18,113,134]. Additionally, no neuroimaging was done either during or post CPB; neuroimaging has previously used as a marker of neurological injury [139,140].

Invasive cerebral venous sampling was not performed in our animal model due to bleeding risks associated with anticoagulation therapy.

6.4.1 Limitations of Animal Model

There are several limitations from using a swine model that could impact the application of results to neonatal patients. First, the piglet baseline temperature is slightly higher than human neonates at 38.5°C compared to 36.5°C [4,141]. Additionally, the oxygen binding affinity of swine hemoglobin is significantly lower than human hemoglobin and could account for lower oxygen saturations in tissue measured [142].

It is also important to note that baseline hematocrit in healthy neonates is around 57% [143], and around 35% at the beginning of reparative cardiac surgery in neonates needing CPB [127]. For healthy swine, we found a hematocrit around 25%. This means that while we are increasing hematocrit during CPB to the same levels used in clinical procedures, we are drastically increasing our hematocrit compared to baseline, and thus increasing the oxygenation capacity of the blood.

Neonatal swine models have been previously used to explore the impact of bypass on the brain and cardiovascular system [4,12,49,86,118]. This gives an advantage over clinical measurements previously performed which can have many confounding variables, especially since none of the subjects have a healthy baseline for comparison [134]. Furthermore, the effectiveness of deep hypothermia for reducing metabolic demand has been verified in swine models [12,133].

6.5 Appendix

6.5.1 Comparison of Microdialysis and Optical Parameters

Previous work from our group focused on deep-hypothermic CPB, specifically, correlating optics parameters with microdialysis metrics of metabolic distress (LPR >40) and neurological injury (glycerol >30 μM) [86].

In animals that underwent deep-hypothermic circulatory arrest, this previous work found associations between elevated LPR and decreased tissue oxygen saturation (StO_2 <48.2%), changes in THC (9% decrease from baseline), and a decrease in rCBF by 61% [86]. We apply these thresholds as a marker of metabolic distress in the present work. Out of the 422 LPR measurements kept, only 16 instances (4% of total measurements) had LPR >40; 56% of these instances had optics parameters below the thresholds previously reported. On average StO_2 and THC remained higher than baseline throughout and CBF decreased by about 25%. This suggests that subjects from this cohort were not exposed to metabolic distress during MH-CPB, as evidenced by the absence of cases with elevated LPR.

Additionally, we ran the analysis with similar time delays as those found in previous work from our lab [86]. While we did not meet the clinical threshold for injury, the data shown in Figure 6.8, was further support of the previous publication. This figure has a 30-minute time delay on the LPR compared to the averaged optical region as this is the delay found previously between injury and impact in LPR. It was found that there is no correlation between StO_2 and the ln(LPR) while there is an inverse relationship between the relative THC and ln(LPR). The linear mixed effects model here is similar to that previously described in section 5.2, however the x variable is now the optical metric instead of time.

Figure 6.8 Linear mixed effects model comparing lactate pyruvate ratio with a 30-minute time delay to optical metrics of StO$_2$ and rTHC while accounting for multiple measurements within the same subject.

We observed 91 instances of glycerol >30 μM (20% of total microdialysis measurements), but only 20 of these reached any of the optical thresholds (22%). Since we were rarely below the thresholds established to maintain anaerobic metabolism [86], this suggests that the injury detected by MD or optics was not due to hypoxic/ischemic injury [119]. The injury seen in this model is therefore likely caused by a different mechanism such as inflammation or increased tissue oxygen tension, as proposed by previous studies [114,119,144].

A similar plot to that done for LPR was performed on the glycerol data, with a 60-minute time delay as found in the previous study from the lab [86]. These results can be seen in Figure 6.9. Our study was in contradiction to the trend previously found between glycerol and relative THC. This could be due to the increase in THC due to bypass, since the previous study defined baseline once on bypass, thus not seeing a significant increase in THC.
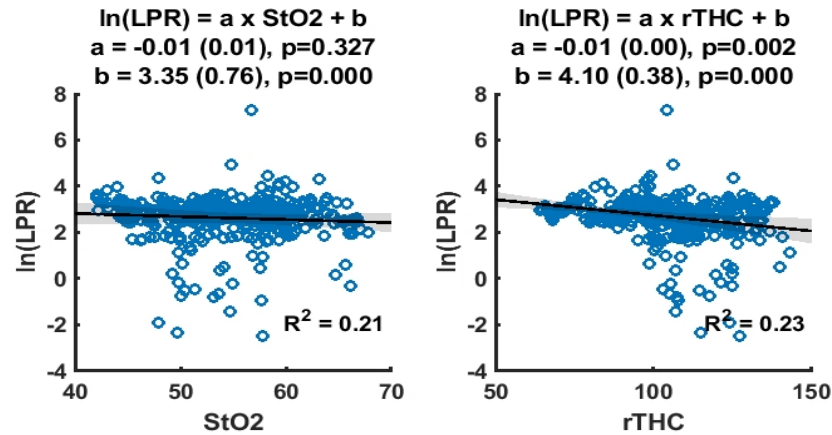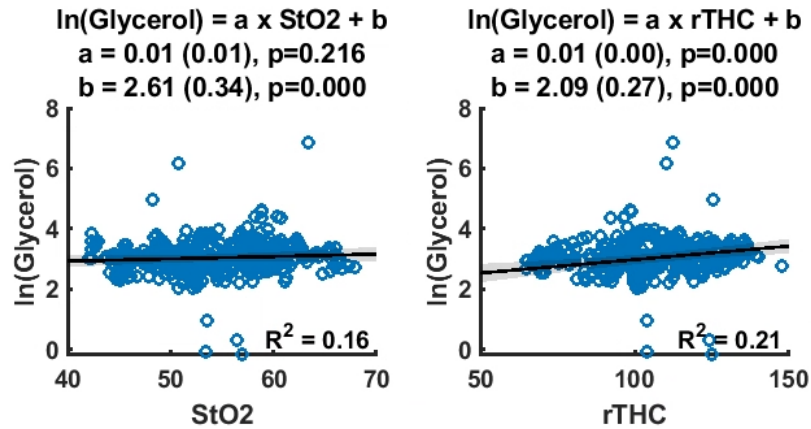
Figure 6.9 Linear mixed effects model comparing glycerol with a 60-minute time delay to optical metrics

of StO$_2$ and rTHC while accounting for multiple measurements within the same subject.

6.5.2 Comparison of Pathology, Respirometry and ROS to Optical Parameters

After euthanasia of the subjects, brain tissue samples were collected from the brain, allowing for

respirometry (using the left hemisphere) and pathology analysis (using the right hemisphere). The

protocol for respirometry measurements was carried out as described in Section 4.4. Since there is only

data at euthanasia, each subject only contributes one data point, according to the survival group they

were placed in. An ANOVA test was then carried out to look for differences between the two groups

(shown in Figure 6.10). None of the metrics were found to be significantly different, thus it was

determined that comparisons to optics metrics would not provide much additional information as there

was no evidence of injury.
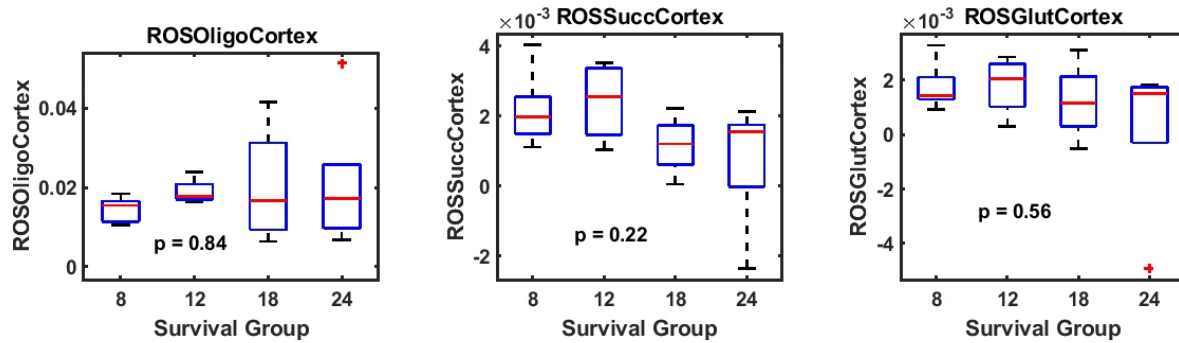
Figure 6.10 Boxplots of respirometry data for different survival groups. All data shown is citrate synthase normalized and thus has no units. An ANOVA test was performed on all three groups and no significant differences were found.

Similar to the respirometry data, the pathology data was only collected at euthanasia, thus each subject is only one data point. Unfortunately, none of the subjects who were euthanized immediately after decannulation had tissue collected for pathology measurements. Thus, we had to compare to a slightly different cohort (n=3) that underwent a sham protocol of 30 minutes on a ventilator with all the same monitoring placed. While this is not a perfect comparison, it does provide an estimate of how these subjects were before the bypass procedure.

Boxplots of this data including the p-value from the ANOVA test can be seen in Figure 6.11, While neither GFAP nor IBA were statistically different at any timepoint, there does appear to be a trend in the GFAP data that resolves at some point between the 12- and 18-hour timepoints. This is further support of the optical findings showing that injury is resolving around 8 hours post-decannulation. While the timeframes may not be the same, there may again be some delay in the injury seen by pathology, similar to that seen in the microdialysis data.
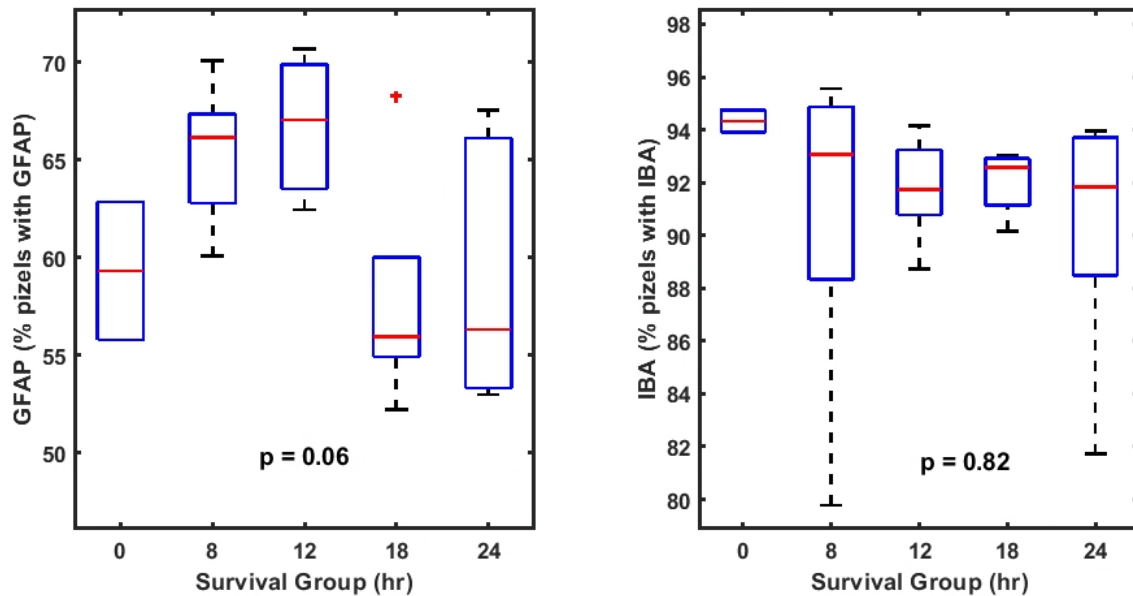
Figure 6.11 Boxplots of pathology data for different survival groups. The healthy group shown as time

equal zero did not go on bypass, but instead had all the same monitoring placed and then

remained on a ventilator for 30 minutes. An anova test was performed on both groups and no

significant differences were found, although GFAP does seem to trend upwards until 12 hours

post-decannulation before resolving.

6.5.3 Sensitivity Analysis

In order to determine the cutoff between the hyper-acute survival and acute survival, several

different cutoff times were tried (ranging from 2 to 12 hours post CPB); this approach is similar to what

was done previously by Ko, et. al [86]. The slope (and corresponding p-value) of both the hyper-acute and

acute survival periods were plotted over the range of cutoff points as seen in Figure 6.12. From these, we

were able to choose when the slope became zero, or changed sign, while maintaining a good linear fit in

both the hyper-acute and acute periods (evaluated using p-values as R^2 values were good throughout,

≈0.8-1). We found that 8 hours post had the lowest p-values for the hyper-acute period, while also having

an acute period slope close to zero. Thus, this time point was chosen as the cutoff between the two periods (results are shown in Figure 6.7 for OEF, THC, CBF and Glycerol).
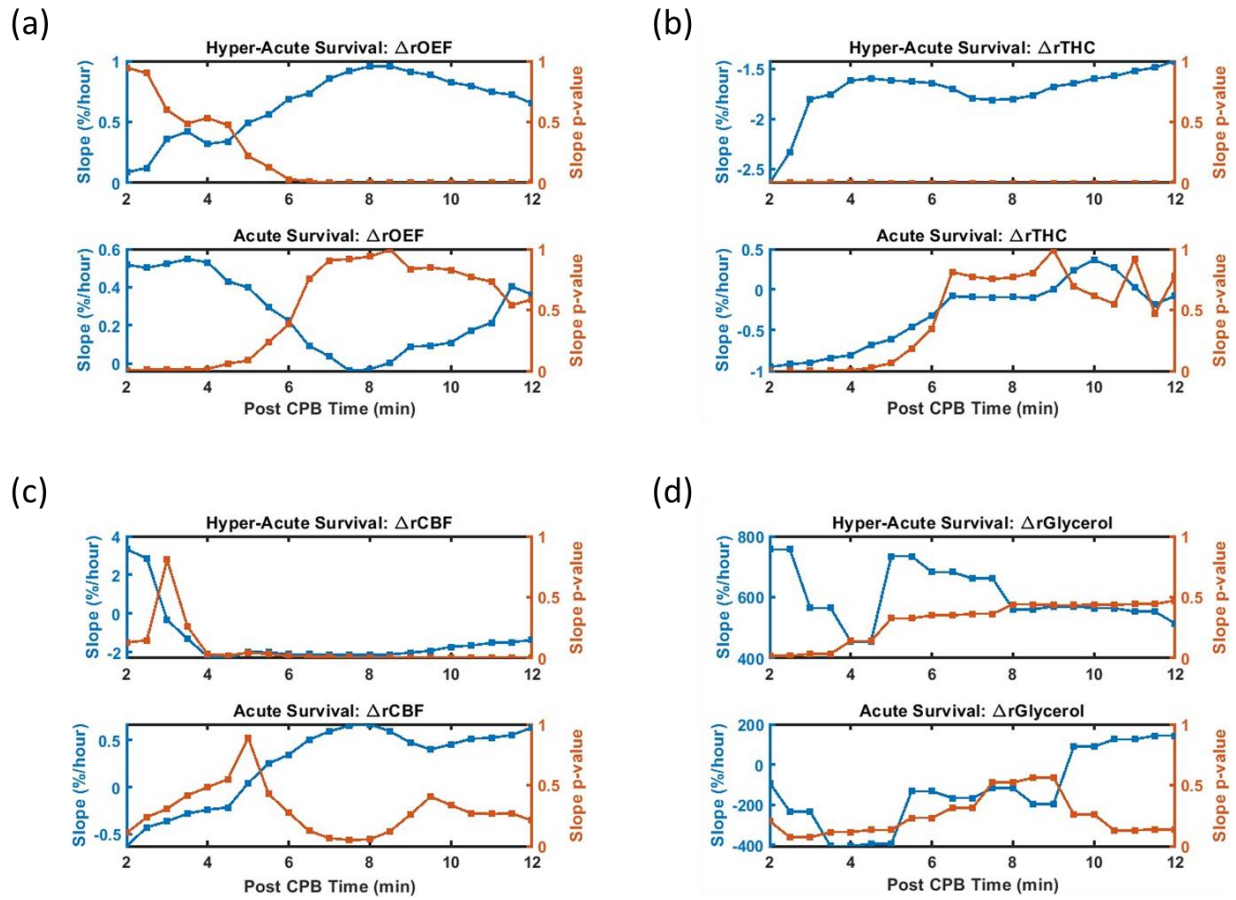
Figure 6.12 Sensitivty analysis for ΔrOEF, ΔrCBF$_{Hct}$, ΔrTHC and ΔrGlycerol. Each sub-figure contains the slope and p-value plotted against different cutoff times for both of the piece-wise functions.

CHAPTER 7

NEW DIFFUSE OPTICS PROBE DESIGNS

The design of the diffuse optical probe head influences our ability to effectively and accurately carry out measurements in a variety of clinical and pre-clinical settings. The probe head couples instrument optoelectronics to the subject. Broadly, a "good" probe head facilitates low loss source transmission into tissue and low loss and stable signal detection; additionally, the operator should be able to easily place and utilize the probe head, and the subject should be comfortable during the entire process. These constraints pose challenges for tissue monitoring, especially in scenarios where the probe must be rapidly placed (and made to adhere) onto the tissue surface, or where the probe needs to be readily readjusted. A very important example along these lines is a surface with hair. As part of my thesis research, I addressed two critical gaps per our current probe designs in this context: 1) measurement repeatability over long duration, and 2) DCS measurements over hair-covered regions of the head.

I carried this work out with the help of two undergraduate students; I was their mentor. The first student was Giselle Matlis, who worked tirelessly on the chassis design and is submitting a paper on the design. The second student was April Hurlock, who spent hours taking hair probe measurements and trying to make the probe less painful for use. The basis of the chassis-based optical probe was modeled after previous probe designs from our lab as outlined in Ko et. al. [4].

7.1 Chassis Probe

A chassis-based optical probe design was developed to address the need to increase the reliability and ease of probe attachment. This design had to account for the compatibility with the optical system, the interface with the patient, size, durability, and cost. Current fiber optic probes for FD-DOS/DCS in our lab and the community at-large range from optical fibers glued to the subject's head to custom printed 3D housings [107,145-148]. Perhaps the most complex of these designs utilize whole head caps (for diffuse optical tomography), wherein each fiber is placed/adjusted individually [149].

The appeal of a chassis probe is to ensure repeatable monitoring measurements can be made after the probe has been removed and then quickly re-secured. This capability is beneficial in the clinical space where a probe may need to be removed periodically to ensure the skin under the probe is free of pressure marks or laser burns. While these skin checks are useful, there is a cost; it can be difficult to place the probe in a location identical to the original location. Another instance for which a chassis style probe is important is in cases that require patient/subject adjustments. For example, during some procedures it may be necessary to move the subject (e.g., from a prone position to a supine position). The "bulky" probe can often be cumbersome to manage during these maneuvers; instead, it is often removed and re-secured after the subject is repositioned. To quantitatively assess the reproducibility that the chassis design provides, DOS and DCS measurements using a conventional approach (manual placement of the probe) versus the chassis approach (placement guided by the pre-attached chassis) were compared in a pediatric swine model [150].

The novel chassis design consisted of a detachable, circumferential chassis that was compatible with the optical probe body (seen in Figure 7.1). Both the probe body and the chassis were 3D-printed using black resin and optimized for non-invasive diffuse optical measurements in a pre-clinical swine model. We focused on three main issues during the design process: 1) compatibility with the optical system; 2) size of probe and chassis, and 3) durability of the design.
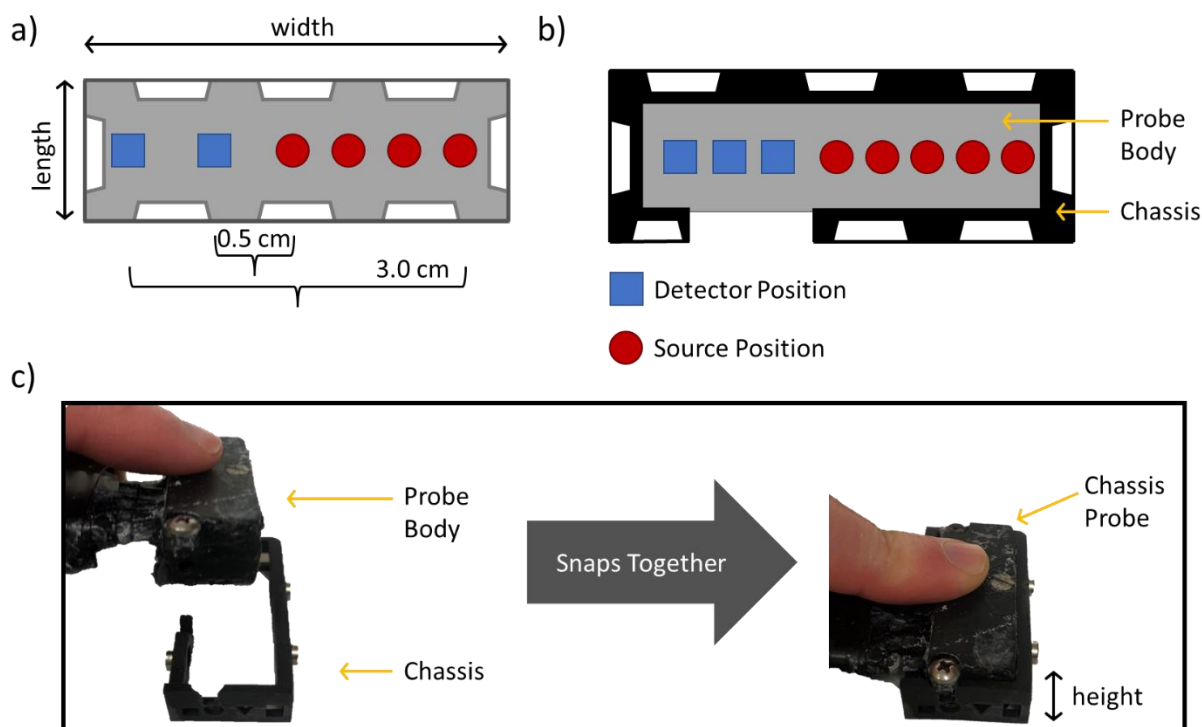
Figure 7.1 Chassis probe design layouts. (a) shows a historical probe with the suture points attached to

the probe body. (b) the chassis and probe body can now be detached. An extra detector and

source position have been added for bDOS capabilities. (c) demonstrates how the probe body

and the chassis snap together to form the chassis probe.

7.1.1 Compatibility with Optical Measurements

Since our optical measurements rely on both FD-DOS and DCS, the fibers for both techniques must be co-located (packaged) into a single probe. This probe contained four source position fibers (2.5mm borosilicated bundles divided into 7 SMA and one FC, Fiberoptics Technology Inc., Pomfret, CT), and two detector fibers (borosilicate bundles divided into one 2mm and 8 780HP, Fiberoptic Systems, Simi Valley, CA); all fibers were housed in a 3D printed body (Figure 7.1). (As an aside, more recent iterations on this probe design also include broadband diffuse optical spectroscopy (bDOS) capabilities, which require incorporation of two additional fibers (one source with a 2.5 mm core and one detector with a 1 mm

core). The broadband measurements are not discussed in my thesis, but our lab is applying broadband for quantification of mitochondrial changes in complex IV (i.e., cytochrome c oxidase), carboxyhemoglobin and water concentrations [151,152].)

Optical measurements require minimization of signal contamination due to ambient light. Ambient light from the room, or from other components/devices placed on the head, can add background intensity which can affect the collected spectra and correlation functions. For example, this can introduce a slight offset in intensity (due to light leakage), and even detector saturation; such effects introduce systematic errors into the measurements [153]. Light leakage is sometimes caused by loss of contact between the surface of the skin and the probe; this effect is common when there is significant patient movement. This loss of contact also can cause some light from the source to travel "along" the surface to the detector, again undermining interpretation of collected data [145,153].

To mitigate the impact of light leakage, several design strategies are employed. The probe can include light-blocking fiber housing (e.g., the probe body can be made of black resin/silicone). Additionally, a light blocking cloth can be used post-placement of the probe to attenuate ambient light. Another design consideration concerns contact pressure between the surface of the skin and the probe contact; means to maintain/insure adequate and "constant" pressure are important and can be implemented more (or less) quantitatively with pressure probes. This increases the measurement robustness to movement and improves measurement reproducibility [145,154,155].

In order to obtain accurate diffuse optics measurements, the source-detector separations (SDS) in the probe need to be precisely maintained. The SDS is the major factor that affects the spatial distribution of photons in the tissue, and thus sets the depth-sensitivity of the measurement. In young children, typical SDS are in the range 1.5 cm to 3 cm, which permits light to reach the brain (located at a

depth of about 0.5-1 cm below the skin surface) [49]. The largest required SDS plays a significant role in setting the overall size of the optical probe.

7.1.2 Probe Size

The second category of the design concerns overall probe size. A lower limit is set by the previously mentioned SDSs needed for sufficient penetration into tissue. This means that the probe needs to be at least 3 cm wide to permit measurements of tissues located ≈1 cm below the skin surface.

The upper limit of the probe size is determined based on the measurable surface area on a subject's forehead. For the piglet data that I collected, we were interested in monitoring the frontal cortex of the brain (Figure 7.3). To apply the conventional, semi-infinite photon diffusion theory for data analysis, the sagittal sinus should be avoided if possible because it typically has different background optical properties compared with those of the brain tissues of interest. Another factor to consider is the curvature of the head. If the probe is flexible, head curvature changes the effective SDS; if the probe is instead rigid, head curvature can inhibit probe contact. Thus, it is ideal to place the probe on the part of the forehead with the least amount of curvature [156]. With these considerations, the upper limit of the probe size, including the chassis, should not exceed 4.5cm x 2.5 cm.

Ideally, the probe should be of "minimal" thickness. This helps to reduce the weight of the probe, and it can also reduce strain on probe attachment parts and allow for improved range of placement positions. The minimal height of the probe (defined in Figure 7.1) was set by the height of the 90-degree bend optical fibers and the prism-coupled fibers.
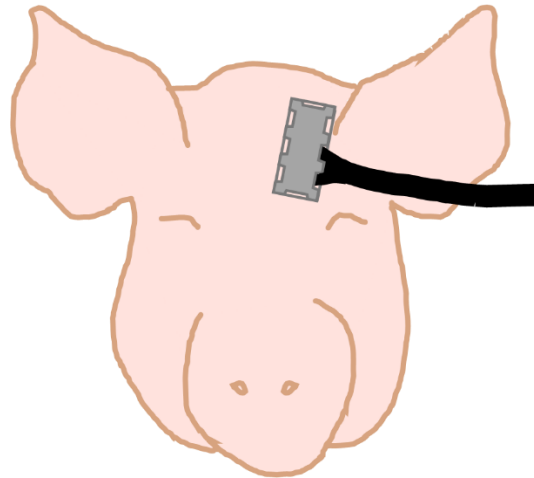
Figure 7.2 Placement of the Optical Probe. The Optical probe is placed over the left frontal cortex.

7.1.3 Probe Durability

The probes need to be durable. This is especially true at the suture points where the probe is attached to the subject. In practice, we found that these suture points were often the first point of breakage on the probe (seen in Figure 7.1). This is likely because the suture points on the probe were placed under constant mechanical strain while the probe was attached. Since these suture points were historically part of the probe body, this meant that once broken, the probe had to be taped or held against the surface to make a measurement, or, sometimes, the entire optical probe would need to be disassembled or discarded. To improve the durability of the optical probe, the suture points were relocated from the probe body to a detachable chassis. This use of the chassis to decouple the probe from the integrity of the suture points represents a critical advance.

7.1.4 Probe Assembly

The optical probe and chassis were modeled using Google Sketchup ED software, versions 2017 and 2019. The chassis framework was designed around the probe body, ensuring that they would fit together. It was determined that triangular cutouts on the chassis best accommodated the suturing techniques of the research personnel performing the attachment and were used for the suture points. Formlabs black resin

(FLGPBL04, Formlabs, Somerville, Massachusetts) was used as the 3D printed black material that absorbed ambient light, prevented light leakage, and was robust enough to last through the whole measurement. Both the probe and chassis were printed on a Formlabs 2 printer (Formlabs, Somerville, Massachusetts) at a 10° angle to ensure that the bottoms would print flat. After the pieces were cleaned, dried, and cured, they were prepared for assembly. This included sanding rough edges and ensuring optical fibers would fit into the housing as well as threading screw holes. The second iteration of the chassis probe (Figure 7.1 b) removed the step of threading screw holes using a 18-8 stainless steel hex nut (M1 x 0.25mm, 91828A003, McMASTER-CARR, Douglasville, Georgia) that was placed inside of the probe body, providing the threads for the screw. This significantly decreased assembly time and improved robustness of the probe as the manual made threads were more likely to be stripped and need repair compared to the stainless-steel nut. Once the probe body was prepared for assembly, the optical fibers were carefully placed inside and enclosed into the printed probe pieces. This was secured together with black liquid electrical tape (07315001126 LTB-400, Gardner Bender, New Berlin, Wisconsin) and screws.

The first iteration of the chassis (Figure 7.3a) included some additional structural features to align and secure the probe and chassis. These features included divots, magnets, and additional screws. The role of the divot was to reduce the footprint of the chassis by providing space for the screw on the probe while simultaneously creating an initial alignment between the probe and chassis. To further improve this initial alignment, two magnets were added to the front, and one to the back of the probe so that the probe could "snap in" to the chassis. Since the magnets were generally not strong enough to hold the probe indefinitely, one screw was added to each lateral wall and the front wall of the chassis. These screws provide translational stability by mechanically securing the probe to the chassis.
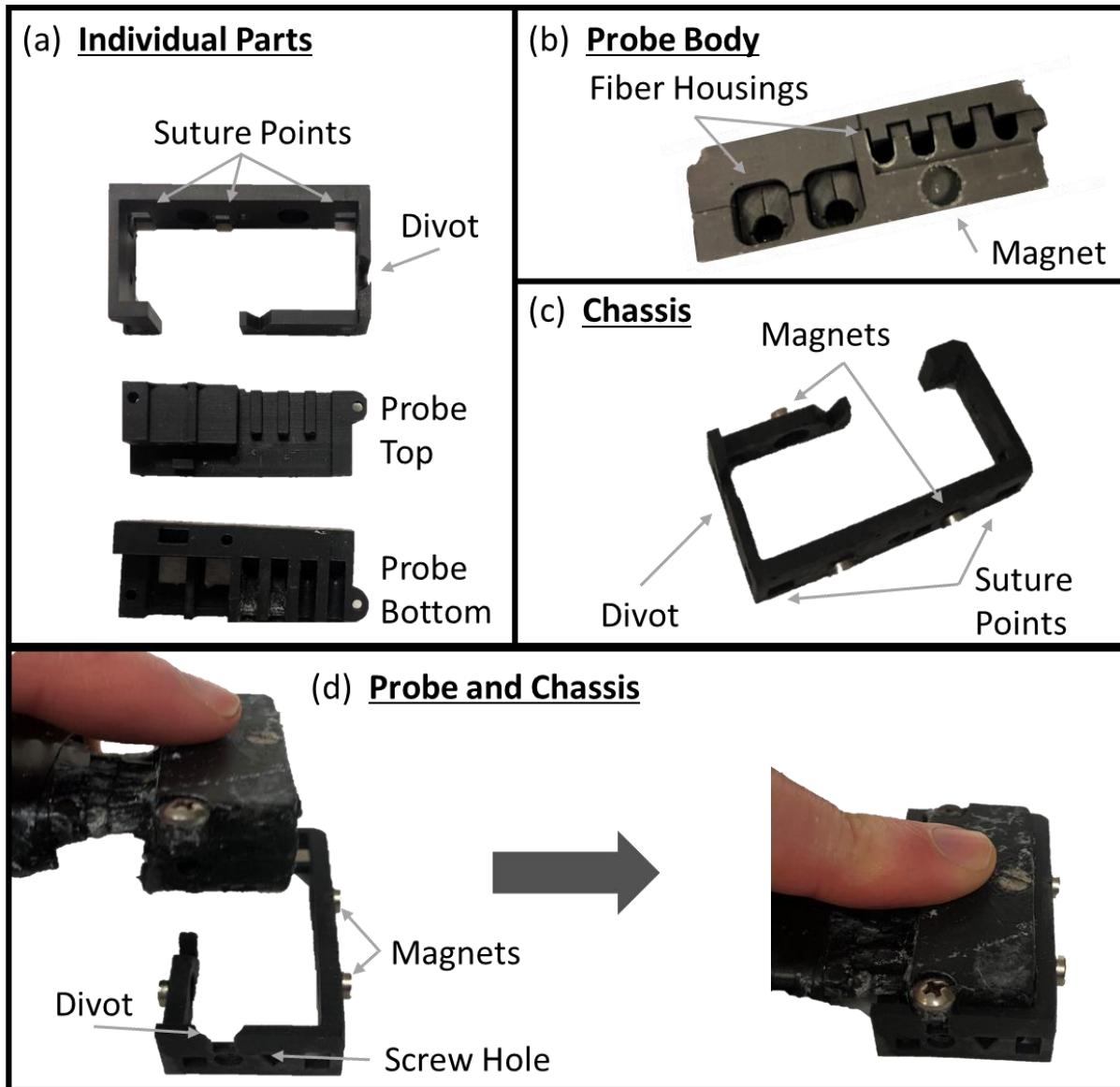
Figure 7.3 First iteration of the chassis probe. (a) Shows the individually 3D printed parts. (b) The

assembled probe body without fibers. The fiber housings are clearly visible, i.e., with two

detector bundles and four source bundles. (c) The chassis with the magnets, divot for alignment,

and suture points for attachment. (d) Alignment of the probe and chassis.

The second iteration of the chassis probe had several additional advantages. The main difference

at this iteration is that it relied on a ratchet design to secure the probe to the chassis, avoiding the need

for the magnets and the screws which could be difficult to insert and secure. The other major change was that a gap was left in the 3D printed probe body such that a nut could be inserted, negating the need to thread screw holes. This iteration also incorporated the additional broadband fibers for bDOS capabilities.
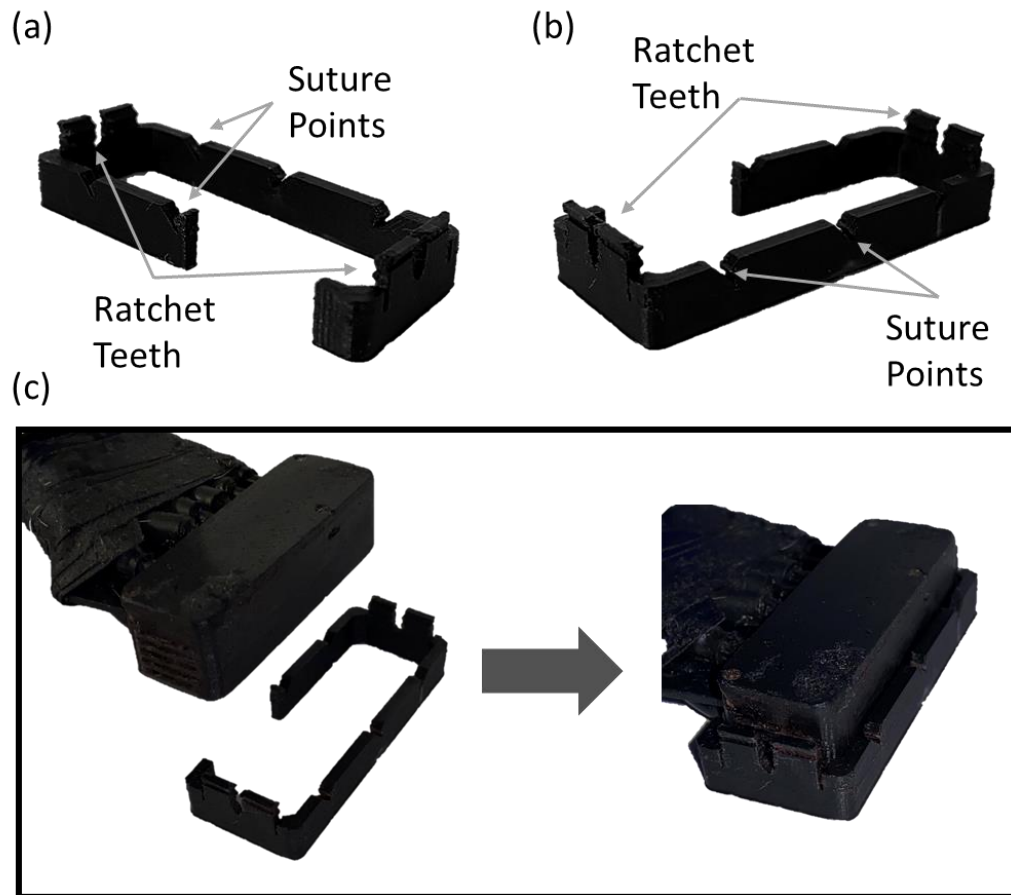
Figure 7.4 Second iteration of chassis probe. (a) and (b) show two different view of the chassis. (c) Attachment of the probe and chassis with the ratchet design.

7.1.5 Validation

To validate the improvements in measurement reproducibility due to use of the chassis, we carried out and compared absolute optical measurements and the coefficient of variation of four independent measurements for both the manual and chassis techniques. No significant differences were observed in either the absolute values or the coefficient of variation between the manual and chassis measurement

(i.e., p>0.05), while giving it the advantage of easy repositioning. This validation study will be published by Giselle Matlis. Overall, this chassis design was found to produce reproducible optical measurements and was a more user-friendly design, making it a promising methodology for future optical probes.

7.2 The Hair Probe

In the US, strokes are among the top five leading causes of death [157]. Acute ischemic stroke is the most common type of stroke and is caused by a regional reduction in CBF, typically due to large vessel occlusion which damages and causes cell death in brain tissue. A reduction in CBF occurs when blood vessels in the brain become narrowed or blocked. Blocked or narrowed vessels are due to a buildup of fatty deposits, blood clots or other debris that travel through the bloodstream and get lodged in brain blood vessels. The middle cerebral artery (MCA) is the most common artery involved in an ischemic stroke [158]. Strokes are typically a heterogeneous, local brain injury (i.e., it is not a homogenous, global injury like ischemia can be) thus requires a localized measurement.

Since DCS measures tissue CBF non-invasively at the bedside, it has been used to study acute stroke physiology and hemodynamic response in the brain. It has been used to examine the response to a variety of stroke interventions including thrombolysis and mechanical thrombectomy, however they are currently limited to stroke patients with infarcts of ischemic penumbra involving the frontal lobe cortex [56,159-161]. By expanding the use of DCS to hair-covered regions of the head, we would be able to monitor stoke physiology and hemodynamic responses in additional regions of the brain (a hypothetical hair probe is pictured in Figure 7.5). This is a major goal in the community.
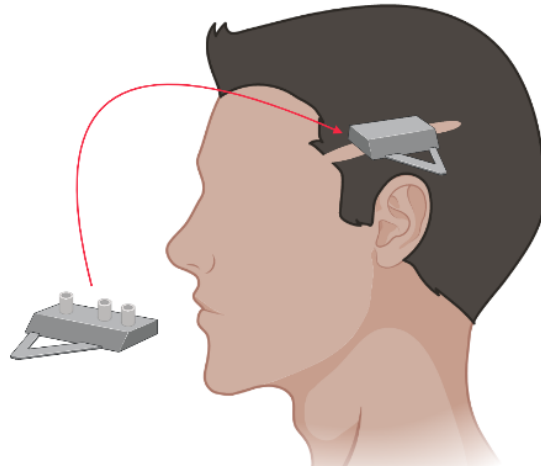
Figure 7.5 Hair probe placement. The hair over the temporal region was parted such that they probe

fibers could make direct contact with the scalp. (Figure courtesy of April Hurlock.)

Currently, DCS and DOS measurements have been almost exclusively done in the anterior frontal

cortex as hair and hair follicles impact light absorption elsewhere [162,163]. DOS/NIRS probes have been

utilized over most regions of the head, since the signal-to-noise of DOS/NIRS is much larger than for DCS

which requires small diameter, single-mode fibers. This has limited application of DCS CBF measurements

to only about 10% of the cortex and has prevented direct localized measurement of hemodynamics at the

injury site, thus limiting the applications in stroke studies.

7.2.1 Compatibility with Optical Measurements

Compatibility considerations (analogous to those discussed in 6.1.1) arise for the hair probe; the main

difference is that we focus only on DCS. To obtain optical measurements at a brain depth of roughly 0.5-

1.25 cm below the scalp, SDSs of 1 cm and either 2.5 cm or 3 cm are used [49]. For a DCS only probe, a

single multi-mode source fiber (1 mm diameter) was employed with two detector bundles (each consisting

of 16 or 32 single mode fibers). The cladding on the single-mode fibers separates each fiber core by

approximately 300 μm within the bundle. Since a single hair follicle has an average thickness of 78 μm and

an average separation of 1.2 mm, it is unlikely that multiple hair fibers will block more than one optical

fiber [164,165]. The 1 mm diameter multi-mode source fiber is also large enough to not be significantly blocked by hair follicles. These fibers were all housed in poured black rubber.

The DCS instrument currently in use in our lab contains 8 detection channels, while the hair probe has 16 or 32 detection fibers. This meant that if a particular detection fiber had low photon counts (<20kHz), a different fiber could be plugged in to the detection channel in case a hair follicle was blocking a particular fiber. In addition, having 8 detector channels allows for improvement of the signal-to-noise by averaging over the 8 channels. In the future, in a 16 or 32 channel DCS instrument, we could further improve the signal-to-noise by using all of the detector fibers. This could be important for subjects with extremely dense or dark hair follicles, which would reduce photon counts below the current signal-to-noise threshold.

7.2.2 Patient Comfort

The hair probe was designed to be able to get around individual hair follicles with the intention that it could "comb through" hair and permit placement directly onto the scalp (seen in Figure 7.5). Like a comb, this meant that the fiber trips must protrude slightly through the probe body to ensure contact with the scalp. Since pressure is needed to obtain good measurements, and without the entire probe body in contact with the scalp, this meant that all of the pressure was applied to the three, small probe tips, causing discomfort and sometimes pain to the subjects. For this to be a viable method of DCS measurement, the probe needs to be comfortable enough to remain on the subject for at least 5 minutes. Assessment of comfort was necessary to ensure usability of the probe.

The first step to improving comfort of the optical probe was to add Teflon balls to help distribute the pressure over a greater surface area without impacting the ability of the probe to comb through hair (seen in Figure 7.6 a and b). We found that this approach did not provide adequate distribution of pressure, leaving marks on the subject's head (shown in Figure 7.6 (c)); thus, rubber strips were added

above and below the fibers on the probe (pictured in Figure 7.6). These rubber strips had the added benefit of improving the stability of the probe. While a single layer of rubber strips, moderately improved comfort of the probe, it was determined that a second rubber strip could be added, further improving comfort without sacrificing signal intensity (Figure 7.6).
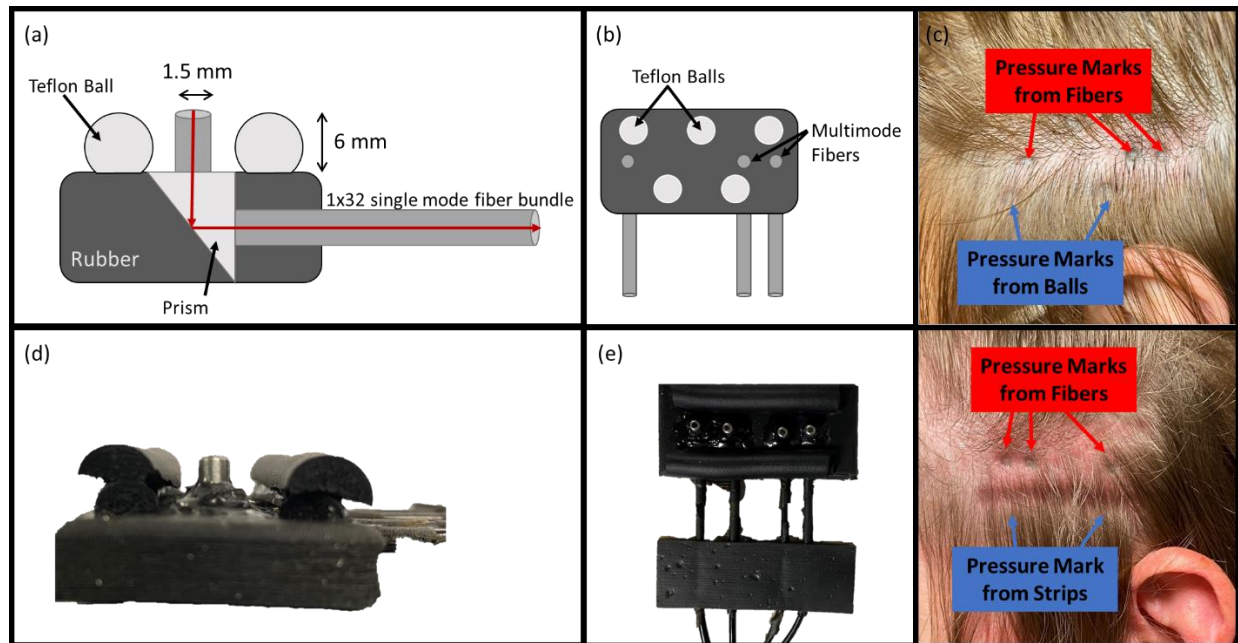
Figure 7.6 Hair Probe Diagrams. (a) and (b) are schematics for the side and top view (respectively) of the first iteration hair probe. (c) Shows the pressure marks left from the first iteration of the subjects head. (d) and (e) are pictures of the final hair probe design, measurements from image (a) are similar for this image as well. (f) is the pressure marks left from the final hair probe design on the subject. It can be seen that the pressure is more evenly distributed from this probe.

7.2.3 Fiber Selection

As was mentioned in section 7.2.1, it was hypothesized that a particular detector fiber could be blocked by a single hair follicle, thus all 32 detector fibers were tested within a single placement to determine which fibers had the best contact with the scalp. To test this theory, intensity measurements were made

114

for all 32 fibers. Since the current DCS instrument only contains 8 detector channels, the hair probe was secured over the temporal region making sure to part the hair where the probe was placed. Once secured, data was collected for the first 8 fibers for 2 minutes, at which point the detectors were turned off and the next set of 8 fibers were plugged in. This was repeated until measurements were made with all 32 fibers. To compare to the forehead region (where there were no hair follicles present), this process was repeated, placing the hair probe on the forehead, and measuring the average intensity of all 32 detector fibers.

The median over the 32 available fibers for the forehead region was 9.1 (IQR: 7.8 - 10.1) and the temporal region was 2.2 (IQR: 2.0 – 2.4) and can be seen in Figure 7.7. An ANOVA test shows that the two groups are statistically different with a p-value <0.001, but there were no outliers in either group to signify that there is a hair follicle blocking an individual fiber. This is in contrast to our hypothesis that certain fibers would be blocked by hair follicles while others would have better transmission from the tissue. Since all fibers are impacted the same, the hair follicles must be absorbing below the surface of the skin as well. Since the intensity is so much lower in the temporal region, we could improve the signal to noise by using all 32 detectors simultaneously. In order to accomplish this, a new DCS instrument, or multiple instruments used in tandem, will have to be assembled.
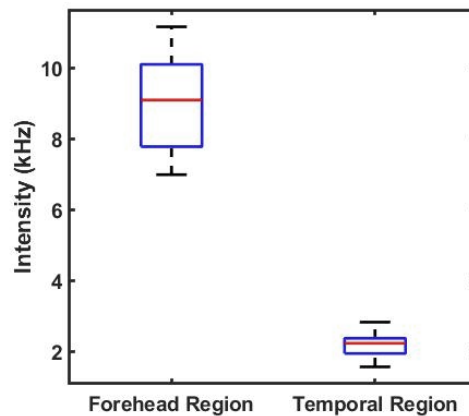
Figure 7.7 Boxplots of the Averaged Detected Intensity for all 32 Hair Probe Fibers for Both the Forehead

Region and the Temporal Region.

7.2.4 Breath Hold Study: Preliminary Data

In order to get an accurate comparison of the traditional forehead probe and the hair probe, a breath

hold experiment was conducted using both probes simultaneously. This required the use of two DCS

instruments to increase the number of detector channels to 16; an individual instrument was used for

each probe so that each probe had 8 detector channels.

The hair probe was placed over the temporal region first as it requires additional steps to ensure

a good measurement. First, a comb was used to part the subject's hair over the location of the

measurement and hair clips and/or gel were used to maintain the part. The instrument was turned on to

ensure a signal of over 5 kHz was obtained, if not, the probe was readjusted to find a better location. Once

the hair probe was placed, the traditional forehead probe was placed over the forehead region. Both

probes were placed on the left side of the subject's head. The probes were secured with an ace bandage

with additional black cloths over the probes to prevent ambient light contaminating the signal.

A single breath hold study consisted of a total of five breath holds. A timeline of a single breath

hold is summarized in Figure 7.8 There is a two-minute baseline consisting of normal breathing, after

116

which the subject was asked to breathe in for three seconds and then out for three seconds before holding

for thirty seconds (seen in Figure 7.8). After the subject was told to release the hold there was a one-

minute recovery before restarting the process. An example of the data collected from a single breath hold

is shown in Figure 7.8.
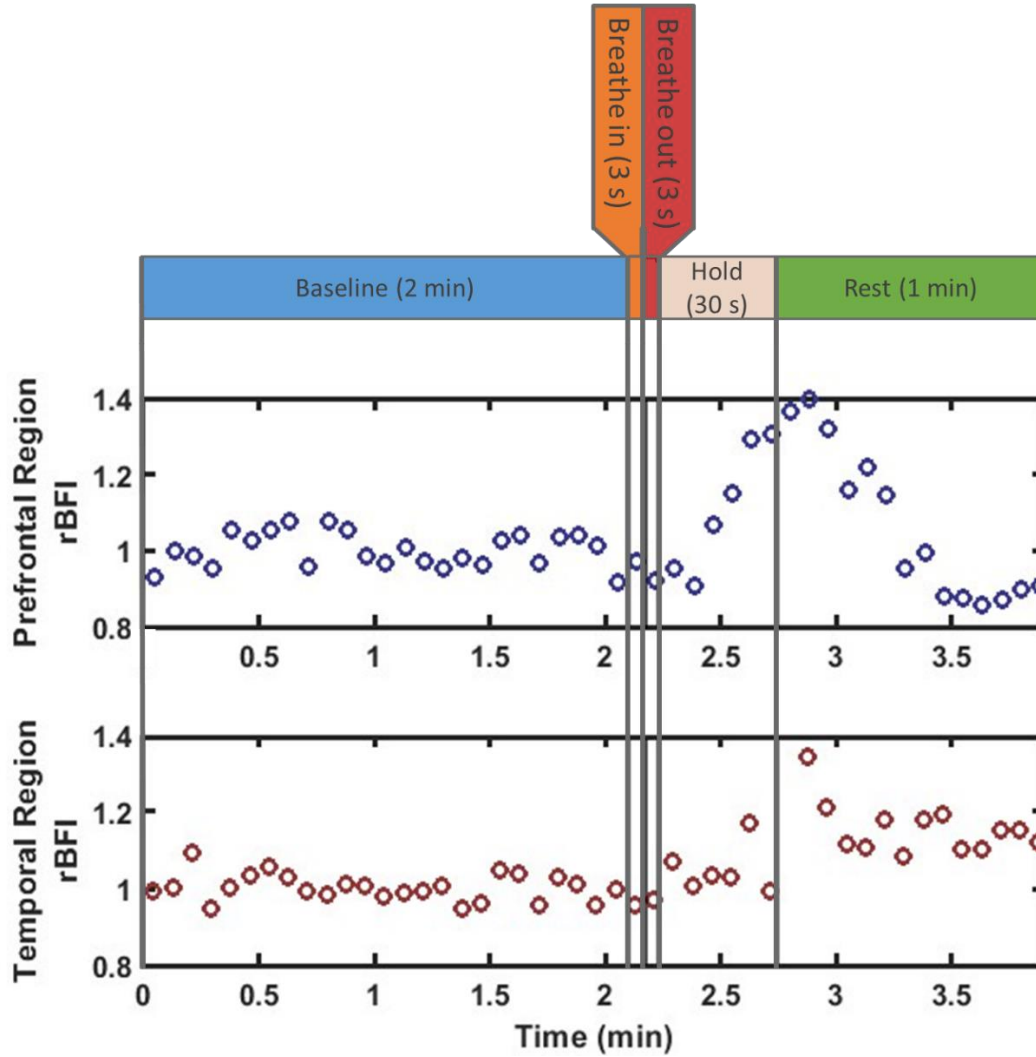
Figure 7.8 Example breath-hold experiment. A traditional probe was placed over the prefrontal region while the hair-probe was placed over the temporal region. The data from both probes were collected simultaneously. (April Hurlock helped in the creation of this figure.)

This preliminary study was completed for three subjects with different hair types yielding varying results. It was determined that darker, thicker hair led to a potential for increased light absorption by the hair and hair follicles, decreasing the measured light intensity and thus decreasing the signal-to-noise for the CBF measurements. Measurements of the fractional change in BFI from the breath hold can be seen in Figure 7.9, with $fBFI = BFI_{hold}/BFI_{baseline}$.
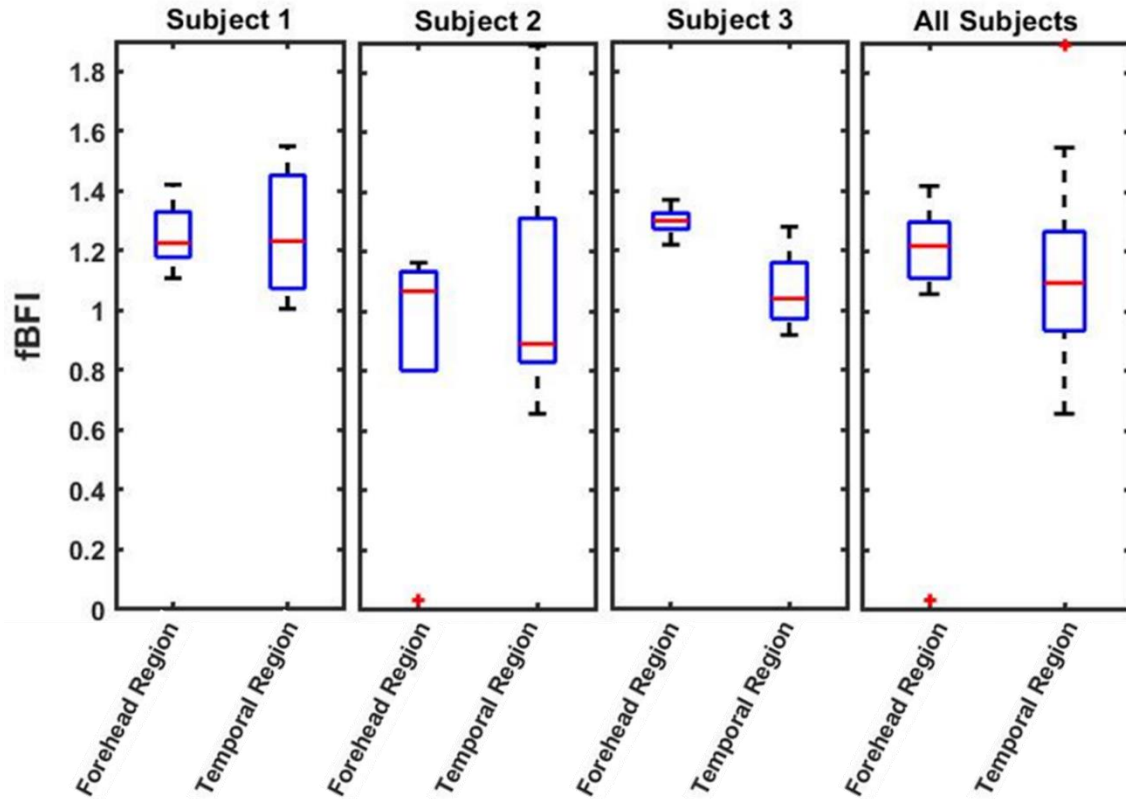
Figure 7.9 fBFI changes during breath hold for different subjects. All subjects had five breath holds

where BFI was measured over the forehead regions and the temporal region simultaneously

with different probes (conventional on the forehead and hair probe over the temporal region).

The fractional BFI ($fBFI$) was defined as the difference in the averaged last 6 seconds of the

breath hold and the averaged last 42 seconds of the baseline period. Subject 1 had long, fine,

light brown hair and had the most consistent measurements between the two probes. Subject 2

had short, thick, brown hair. There was some light leakage from the source present as there was

not adequate pressure to hold either probe on. Subject 3 had long, medium-thick, reddish-

brown hair.

While this is still in the testing phase, great advances were made towards measurements over

hair covered regions. We were able to develop a prototype design and improve comfort so that a

preliminary breath hold study could be completed. We were able to observe the expected shape over

both the forehead region and the temporal region although the data quality was severely impacted by the hair type of the individual. In order to improve data quality additional fibers could be used in order to increase the total number of photons measured. To do this, the number of detectors available on the DCS instrument would need to be increased.

CHAPTER 8

SUMMARY AND FUTURE OUTLOOK

In the presented work, I used two diffuse optical techniques to address the clinical need for noninvasive, continuous cerebral monitoring of hemodynamics and metabolism during cardiopulmonary bypass (CPB) surgical procedures. These measurements demonstrated the potential impact diffuse optics to improve and individualize care within this vulnerable population of infants with congenital heart disease. In the future, it is my hope that non-invasive diffuse optical neuromonitoring of injury associated with CPB (as well as in other surgical procedures) could aid in the optimization of clinical management during periods of increased neurological vulnerability.

Specifically, we characterized cerebral hemodynamic trends during and acutely after CPB. During CPB, we found (on average) temporal decreases in cerebral blood flow with concurrent increases in cerebral oxygen extraction and cerebral blood volume fraction. Microdialysis measurements of glycerol were further elevated during the 8-hour hyperacute phase immediately after CPB (i.e., elevated compared to the baseline period). In combination, these results suggest a possible inflammatory mechanism of injury from mild hypothermic CPB. Therefore, it may be necessary to cool lower than 34°C to reduce metabolism more and suppress inflammatory cascades. The post-CPB sensitivity analysis found that there was a return of cerebral blood flow and oxygen extraction fraction back towards baseline. This analysis was corroborated to some degree by the invasive marker of cell membrane damage, glycerol, which returned to baseline within the same timeframe. Together, the observations and analysis suggest that both the CPB period and the hyperacute post-CPB period (0-8 hour) are critical windows of neurological vulnerability.

In carrying out this study, we came to appreciate that hematocrit changes during CPB can be large, and that the application of advanced diffuse optical approaches must properly account for these hematocrit (Hct) changes. Building on a theoretical model (supported by simulation) in the literature, we developed an analysis scheme to account for the influence of Hct variation on diffuse optical

measurements. Application to our measurement data led to physiological plausible CBF and $CMRO_2$ quantification; the traditional approach led to non-physiological CBF and $CMRO_2$. We consider this to be a crucial advance in the field of diffuse optics, because there are a multitude of applications that are accompanied by changes in hematocrit, for example including ECMO and studies involving sickle cells, blood transfusions, or anemia due to blood loss. The hematocrit-corrected analysis performed permits more quantitative measurement of blood flow, and thus a better biomarker metric.

In addition to the instrumentation and CPB advances described above, I addressed several practical needs for our optical probe designs. I worked on a chassis design which permits quick removal/reattachment of the probe with good reproducibility (superior to our prior probes). By implementing this design in clinical spaces, patient readjustments, such as lifting the probe to check the skin for pressure marks, will become more routine for clinicians and technicians. These improvements, in turn, will make diffuse optics better suited for clinical use over long time durations. In a different vein, the advances I made with the hair probe took steps towards more routine diffuse optical measurements over hair-covered regions of the head. We were able to significantly improve the comfort of the probe to easily perform breath hold tests, albeit the data quality for probes placed over the temporal region were still worse than the prefrontal region. This remains a work in progress.

In total, the evidence presented throughout this thesis represents one small step towards the inclusion of cerebral diffuse optical monitoring as a standard of care in all health care settings. There is still much work to be done, and I pass it off to the next generation of visionaries to carry out this goal.

References

1. Hoffman, J.I.E.; Kaplan, S. The incidence of congenital heart disease. *Journal of the American College of Cardiology* **2002**, *39*, 1890-1900.
2. Marino, B.S.; Lipkin, P.H.; Newburger, J.W.; Peacock, G.; Gerdes, M.; Gaynor, J.W.; Mussatto, K.A.; Uzark, K.; Goldberg, C.S.; JohnsonJr, W.H.; et al. Neurodevelopmental Outcomes in Children With Congenital Heart Disease: Evaluation and Management. *Circulation* **2012**, *126*, 1143-1172.
3. Buckley, E.M.; Lynch, J.M.; Goff, D.A.; Schwab, P.J.; Baker, W.B.; Durduran, T.; Bush, D.R.; Nicolson, S.C.; Montenegro, L.M.; Naim, M.Y.; et al. Early postoperative changes in cerebral oxygen metabolism following neonatal cardiac surgery: Effects of surgical duration. *The Journal of Thoracic and Caridovascular Surgery* **2013**, *145*, 196-205.
4. Ko, T.S.; Mavroudis, C.D.; Baker, W.B.; Morano, V.C.; Mensh-Brown, K.; Boorady, T.W.; Schmidt, A.L.; Lynch, J.M.; Bush, D.R.; Gentile, J.; et al. Non-invasive optical neuromonitoring of the temperature-dependence of cerebral oxygen metabolism during deep hypothermic cardiopulmonary bypass in neonatal swine. *Journal of Cerebral Blood Flow & Metabolism* **2020**, *40*, 187-203, doi:10.1177/0271678X18809828.
5. Lynch, J.M.; Buckley, E.M.; Schwab, P.J.; McCarthy, A.L.; Winters, M.E.; Busch, D.R.; Xiao, R.; Goff, D.A.; Nicolson, S.C.; Montenegro, L.M.; et al. Time to surgery and preoperative cerebral hemodynamics predict postoperative white matter injury in neonates with hypoplastic left heart syndrome. *The Journal of Thoracic and Cardiobascular Surgery* **2014**, *148*, 2181-2188.
6. Jöbsis, F.F. Noninvasive, infrared monitoring of cerebral and myocardial oxygen sufficiency and circulatory parameters. *Science* **1977**, *198*, 1264-1267, doi:10.1126/science.929199.
7. Vliet, F.F.J.-V. Non-Invasive, Near Infrared Monitoring of Cellular Oxygen Sufficiency in Vivo. In *Oxygen Transport to Tissue VII. Advances in Experimental Medicine and Biology*, Kreuzer, F., Cain, S.M., Turek, Z., Goldstick, T.K., Ed.; Springer: Boston, MA, 1985; Volume 191, pp. 833-842.
8. Prahl, S. Optical Absorption of Hemoglobin. **1999**.
9. Palmer, K.F.; Williams, D. Optical properties of water in the near infrared. *Journal of the Optical Society of America* **1974**, *64*, 1107-1110, doi:10.1364/JOSA.64.001107.
10. Yodh, A.G.; Chance, B. Spectroscopy and imaging with diffusing light. *Physics Today* **1995**, *48*, 34–40.
11. J.S., W.; M., C.; D.T., D.; P., v.d.Z.; S., A.; A.D., E.; E.O.R., R. Measurement of Optical Path Length for Cerebral Near-Infrared Spectroscopy in Newborn Infants. *Developmental Neuroscience* **1990**, *12*, 140-144.
12. Volk, L.E. Increased cerebral mitochondrial dysfunction and reactive oxygen species with cardiopulmonary bypass. *European Journal of Cardio-Thoracic Surgery* **2021**, *59*, 1256-1264, doi:10.1093/ejcts/ezaa439.
13. Engelman, R.; Baker, R.A.; Likosky, D.S.; Grigore, A.; Dickinson, T.A.; Shore-Lesserson, L.; Hammon, J.W. The Society of Thoracic Surgeons, The Society of Cardiovascular Anesthesiologists, and The American Society of ExtraCorporeal Technology: Clinical Practice Guidelines for Cardiopulmonary Bypass--Temperature Management During Cardiopulmonary Bypass. *Journal of Cardiothoracic and Vascular Anesthesia* **2015**, *29*, 1104-1113, doi:10.1053/j.jvca.2015.07.011.
14. Saad, H.; Aladawy, M. Temperature management in cardiac surgery. *Global Cardiology Science and Practice* **2013**, *2013*, 7, doi:10.5339/gcsp.2013.7.
15. Liu, L.; Yenari, M.A. Therapeutic hypothermia: neuroprotective mechanisms. *Frontiers in Bioscience* **2007**, *12*, 816-825.

16. Bhalala, U.S.; Appachi, E.; Mumtaz, M.A. Neurologic Injury Associated with Rewarming from Hypothermia: Is Mild Hypothermia on Bypass Better than Deep Hypothermic Circulatory Arrest? *Frontiers in Pediatrics* **2016**, *4*, doi:10.3389/fped.2016.00104.

17. Parr, G.V.; Blackstone, E.H.; Kirklin, J.W. Cardiac performance and mortality early after intracardiac surgery in infants and young children. *Circulation* **1975**, *51*, 867-874, doi:10.1161/01.cir.51.5.867.

18. Wernovsky, G.; Wypij, D.; Jonas, R.A.; MayerJr, J.E.; Hanley, F.L.; Hickey, P.R.; Walsh, A.Z.; Chang, A.C.; Castañeda, A.R.; Newburger, J.W.; et al. Postoperative Course and Hemodynamic Profile After the Arterial Switch Operation in Neonates and Infants. *Circulation* **1995**, *92*, 2226-2235, doi:10.1161/01.CIR.92.8.2226.

19. Yuerek, M.; Rossano, J.W.; Mascio, C.E.; Shaddy, R.E. Postoperative management of heart failure in pediatric patients. *Expert Review of Cardiovascular Therapy* **2016**, *14*, 201-215, doi:10.1586/14779072.2016.1117388.

20. Robert, S.M.; Borasino, S.; Dabal, R.J.; Cleveland, D.C.; Hock, K.M.; Alten, J.A. Postoperative Hydrocortisone Infusion Reduces the Prevalence of Low Cardiac Output Syndrome After Neonatal Cardiopulmonary Bypass*. *Pediatric Critical Care Medicine* **2015**, *16*.

21. Meinke, M.; Müller, G.; Helfmann, J.; Friebel, M. Empirical model functions to calculate hematocrit-dependent optical properties of human blood. *Appl. Opt.* **2007**, *46*, 1742-1753, doi:10.1364/AO.46.001742.

22. Sathialingam, E.; Williams, E.K.; Lee, S.Y.; McCracken, C.E.; Lam, W.A.; Buckley, E.M. Hematocrit significantly confounds diffuse correlation spectroscopy measurements of blood flow. *Biomedical Optics Express* **2020**, *11*, 4786-4799.

23. Boas, D.A.; Sakadžic, S.; Selb, J.; Farzam, P.; Franceschini, M.A.; Carp, S.A. Establishing the diffuse correlation spectroscopy signal relationship with blood flow. *Neurophotonics* **2016**, *3*, 031412, doi:10.1117/1.nph.3.3.031412.

24. Wang, L.V.; Wu, H.-I. *Biomedical Optics: Principles and Imaging*; John Wiley & Sons: Hoboken, New Jersey, 2007.

25. Baker, W.B. Optical Cerebral Blood Flow Monitoring of Mice To Men. University of Pennsylvania, 2015.

26. Boas, D.A. Diffuse photon probes of structural and dynamical properties of turbid media: Theory and biomedical applications. University of Pennsylvania 1996.

27. Ko, T.S. DIFFUSE OPTICAL CEREBRAL DIAGNOSTICS FOR REAL-TIME GUIDANCE DURING PEDIATRIC SURGERY AND RESUSCITATION. University of Pennsylvania, 2018.

28. Lynch, J.M. INVESTIGATIONS OF CEREBRAL HEMODYNAMICS IN INFANTS WITH CRITICAL CONGENITAL HEART DISEASE USING DIFFUSE OPTICS University of Pennsylvania, 2014.

29. Forti, R.M. Translation of a diffuse optical system for monitoring neurocritical patients. Universidade Estadual de Campinas, 2020.

30. Durduran, T.; Choe, R.; Baker, W.B.; Yodh, A.G. Diffuse optics for tissue monitoring and tomography. *Reports on Progress in Physics* **2010**, *73*, 076701, doi:10.1088/0034-4885/73/7/076701.

31. Patterson, M.S.; Andersson-Engels, S.; Wilson, B.C.; Osei, E.K. Absorption spectroscopy in tissue-simulating materials: a theoretical and experimental study of photon paths. *Appl. Opt.* **1995**, *34*, 22, doi:10.1364/ao.34.000022.

32. Cheong, W.-F.; Prahl, S.A.; Welch, A.J. A Review of the Optical Properties of Biological Tissues. *IEEE Journal of Quantum Electronics* **1990**, *26*.

33. Fishkin, J.B.; Gratton, E. Propagation of photon-density waves in strongly scattering media containing an absorbing semi-infinite plane bounded by a straight edge. *J. Opt. Soc. Am. A* **1993**, *10*, 127, doi:10.1364/josaa.10.000127.

34. Haskell, R.C.; Svaasand, L.O.; Tsay, T.-T.; Feng, T.-C.; Tromberg, B.J.; McAdams, M.S. Boundary conditions for the diffusion equation in radiative transfer. *J. Opt. Soc. Am. A* **1994**, *11*, 2727, doi:10.1364/josaa.11.002727.

35. Aronson, R. Boundary conditions for diffusion of light. *J. Opt. Soc. Am. A* **1995**, *12*, 2532-2539, doi:10.1364/JOSAA.12.002532.

36. Arridge, S.; Cope, M.; Delpy, D. The theoretical basis for the determination of optical pathlengths in tissue: temporal and frequency analysis. . *Physics in Medicine and Biology* **1992**, *37*, 1531-1560, doi:10.1088/0031-9155/37/7/005.

37. Fantini, S.; Franceschini, M.A.; Fishkin, J.B.; Barbieri, B.; Gratton, E. Quantitative determination of the absorption spectra of chromophores in strongly scattering media: a light-emitting-diode based technique. *Appl. Opt.* **1994**, *33*, 5204, doi:10.1364/ao.33.005204.

38. Fantini, S.; Hueber, D.; Franceschini, M.A.; Gratton, E.; Rosenfeld, W.; Stubblefield, P.G.; Maulik, D.; Stankovic, M.R. Non-invasive optical monitoring of the newborn piglet brain using continuous-wave and frequency-domain spectroscopy. *Physics in Medicine and Biology* **1999**, *44*, 1543-1563, doi:10.1088/0031-9155/44/6/308.

39. Wolthuis, R.; van Aken, M.; Fountas, K.; Robinson; Bruining, H.A.; Puppels, G.J. Determination of Water Concentration in Brain Tissue by Raman Spectroscopy. *Analytical Chemistry* **2001**, *73*, 3915-3920, doi:10.1021/ac0101306.

40. Wyatt, J.S.; Delpy, D.T.; Cope, M.; Wray, S.; Reynolds, E.O.R. QUANTIFICATION OF CEREBRAL OXYGENATION AND HAEMODYNAMICS IN SICK NEWBORN INFANTS BY NEAR INFRARED SPECTROPHOTOMETRY. *The Lancet* **1986**, *328*, 1063-1066, doi: 10.1016/S0140-6736(86)90467-8.

41. Buckley, E.M.; Cook, N.M.; Durduran, T.; Kim, M.N.; Zhou, C.; Choe, R.; Yu, G.; Shultz, S.; Sehgal, C.M.; Licht, D.J.; et al. Cerebral hemodynamics in preterm infants during positional intervention measured with diffuse correlation spectroscopy and transcranial Doppler ultrasound. *Optics Express* **2009**, *17*, 12571-12581, doi:10.1364/OE.17.012571.

42. Yu, G.; Floyd, T.F.; Durduran, T.; Zhou, C.; Wang, J.; Detre, J.A.; Yodh, A.G. Validation of diffuse correlation spectroscopy for muscle blood flow with concurrent arterial spin labeled perfusion MRI. *Optics Express* **2007**, *15*, 1064-1075, doi:10.1364/OE.15.001064.

43. Roche-Labarbe, N.; Carp, S.A.; Surova, A.; Patel, M.; Boas, D.A.; Grant, P.E.; Franceschini, M.A. Noninvasive optical measures of CBV, StO2, CBF index, and rCMRO2 in human premature neonates' brains in the first six weeks of life. *Human Brain Mapping* **2010**, *31*, 341-352, doi:10.1002/hbm.20868.

44. Chu, B. *Laser Light Scattering, Basic Principles and Practice*, 2nd ed.; Academic: New York, 1991.

45. Berne, B.J.; Pecora, R. *Dynamic Light Scattering: With Applications to Chemistry, Biology, and Physics*; Dover Publications: Mineola, New York, 2013.

46. *Dynamic Light Scattering: The Method and Some Applications*, 1st ed.; Brown, W., Ed.; Clarendon Press: New York, 1993.

47. Carp, S.A.; Robinson, M.B.; Franceschini, M.A. Diffuse correlation spectroscopy: current status and future outlook. *Neurophotonics* **2023**, *10*, doi:10.1117/1.nph.10.1.013509.

48. Boas, D.A.; Yodh, A.G. Spatially varying dynamical properties of turbid media probed with diffusing temporal light correlation. *J. Opt. Soc. Am. A* **1997**, *14*, 192-215, doi:10.1364/JOSAA.14.000192.

49.   Durduran, T.; Yodh, A.G. Diffuse correlation spectroscopy for non-invasive, micro-vascular cerebral blood flow measurement. *NeuroImage* **2014**, *85*, 51-63, doi:10.1016/j.neuroimage.2013.06.017.

50.   Lemieux, P.A.; Durian, D.J. Investigating non-Gaussian scattering processes by using nth-order intensity correlation functions. *J. Opt. Soc. Am. A* **1999**, *16*, 1651-1664, doi:10.1364/JOSAA.16.001651.

51.   Ackerson, B.; Dougherty, R.; Reguigui, N.; Nobbmann, U. Correlation transfer - Application of radiative transfer solution methods to photon correlation problems. *Journal of Thermophysics and Heat Transfer - J THERMOPHYS HEAT TRANSFER* **1992**, *6*, 577-588, doi:10.2514/3.11537.

52.   Dougherty, R.L.; Ackerson, B.J.; Reguigui, N.M.; Dorri-Nowkoorani, F.; Nobbmann, U. Correlation transfer: Development and application. *Journal of Quantitative Spectroscopy and Radiative Transfer* **1994**, *52*, 713-727, doi:10.1016/0022-4073(94)90037-X.

53.   Boas, D.A.; Campbell, L.E.; Yodh, A.G. Scattering and Imaging with Diffusing Temporal Field Correlations. *Physical Review Letters* **1995**, *75*, 1855-1858, doi:10.1103/PhysRevLett.75.1855.

54.   Durduran, T.; Yu, G.; Burnett, M.G.; Detre, J.A.; Greenberg, J.H.; Wang, J.; Zhou, C.; Yodh, A.G. Diffuse optical measurement of blood flow, blood oxygenation, and metabolism in a human brain during sensorimotor cortex activation. *Opt. Lett.* **2004**, *29*, 1766-1768, doi:10.1364/OL.29.001766.

55.   Durduran, T.; Zhou, C.; Buckley, E.M.; Kim, M.N.; Yu, G.; Choe, R.; Gaynor, J.W.; Spray, T.L.; Durning, S.M.; Mason, S.E.; et al. Optical measurement of cerebral hemodynamics and oxygen metabolism in neonates with congenital heart defects. *Journal of Biomedical Optics* **2010**, *15*, 037004, doi:10.1117/1.3425884.

56.   Durduran, T.; Zhou, C.; Edlow, B.L.; Yu, G.; Choe, R.; Kim, M.N.; Cucchiara, B.L.; Putt, M.E.; Shah, Q.; Kasner, S.E.; et al. Transcranial Optical Monitoring of Cerebrovascular Hemodynamics in Acute Stroke Patients. *Optics Express* **2009**, *17*, 3884-3902, doi:10.1364/OE.17.003884.

57.   Ninck, M.; Untenberger, M.; Gisler, T. Diffusing-wave spectroscopy with dynamic contrast variation: disentangling the effects of blood flow and extravascular tissue shearing on signals from deep tissue. *Biomedical Optics Express* **2010**, *1*, 1502, doi:10.1364/boe.1.001502.

58.   Carp, S.A.; Roche-Labarbe, N.; Franceschini, M.-A.; Srinivasan, V.J.; Sakadžić, S.; Boas, D.A. Due to intravascular multiple sequential scattering, Diffuse Correlation Spectroscopy of tissue primarily measures relative red blood cell motion within vessels. *Biomedical Optics Express* **2011**, *2*, 2047-2054, doi:10.1364/BOE.2.002047.

59.   Goldsmith, H.L.; Marlow, J.C. Flow behavior of erythrocytes. II. Particle motions in concentrated suspensions of ghost cells. *Journal of Colloid and Interface Science* **1979**, *71*, 383-407, doi:10.1016/0021-9797(79)90248-0.

60.   Bishop, J.J.; Popel, A.S.; Intaglietta, M.; Johnson, P.C. Effect of aggregation and shear rate on the dispersion of red blood cells flowing in venules. *American Journal of Physiology-Heart and Circulatory Physiology* **2002**, *283*, H1985-H1996, doi:10.1152/ajpheart.00888.2001.

61.   Higgins, J.M.; Eddington, D.T.; Bhatia, S.N.; Mahadevan, L. Statistical Dynamics of Flowing Red Blood Cells by Morphological Image Processing. *PLoS Computational Biology* **2009**, *5*, e1000288, doi:10.1371/journal.pcbi.1000288.

62.   Twersky, V. Absorption and Multiple Scattering by Biological Suspensions. *Journal of the Optical Society of America* **1970**, *60*, 1084-1093, doi:10.1364/josa.60.001084.

63.   Madden, J.A. The Effect of Carbon Dioxide on Cerebral Arteries. *Pharmacology and Therapeutics* **1993**, *59*, 229-250, doi:10.1016/0163-7258(93)90045-f.

64.   Polderman, K.H. Mechanisms of action, physiological effects, and complications of hypothermia. *Critical Care Medicine* **2009**, *37*.

65.   Leffler, C.W.; Busya, D.W.; Beasley, D.G.; Armstead, W.M.; Mirro, R. Postischemic Cerebral Microvascular Responses to Norepinephrine and Hypotension in Newborn Pigs. *Stroke* **1988**, *20*, 541-546, doi:10.1161/01.str.20.4.541.

66.   Cha, W.; Beissinger, R.L. Evaluation of shear-induced particle diffusivity in red cell ghosts suspensions. *Korean Journal of Chemical Engineering* **2001**, *18*, 479-485, doi:10.1007/bf02698294.

67.   Goldsmith, H.L.; Marlow, J.; MacIntosh, F.C. Flow behaviour of erythrocytes - I. Rotation and deformation in dilute suspensions. *Proceedings of the Royal Society of London. Series B. Biological Sciences* **1997**, *182*, 351-384, doi:10.1098/rspb.1972.0084.

68.   Wang, D.; Parthasarathy, A.B.; Baker, W.B.; Gannon, K.; Kavuri, V.; Ko, T.; Schenkel, S.; Li, Z.; Li, Z.; Mullen, M.T.; et al. Fast blood flow monitoring in deep tissues with real-time software correlators. *Biomedical Optics Express* **2016**, *7*, 776-797.

69.   Buckley, E.M.; Parthasarathy, A.B.; Grant, P.E.; Yodh, A.G.; Franceschini, M.A. Diffuse correlation spectroscopy for measurement of cerebral blood flow: future prospects. *Neurophotonics* **2014**, *1*, 011009, doi:10.1117/1.nph.1.1.011009.

70.   Hueber, D.; Franceschini, M.A.; Ma, H.-Y.; Zhang, Q.; Ballesteros, J.; Fantini, S.; Wallace, D.; Ntziachristos, V.; Chance, B. Non-invasive and quantitative near-infrared haemoglobin spectrometry in the piglet brain during hypoxic stress, using a frequency-domain multidistance instrument. *Physics in medicine and biology* **2001**, *46*, 41-62, doi:10.1088/0031-9155/46/1/304.

71.   Böcklin, C.; Baumann, D.; Stuker, F.; Fröhlich, J. Mixing formula for tissue-mimicking silicone phantoms in the near infrared. *Journal of Physics D: Applied Physics* **2015**, *48*, 105402, doi:10.1088/0022-3727/48.

72.   Bays, R.; Wagnières, G.; Robert, D.; Theumann, J.-F.; Vitkin, A.; Savary, J.-F.; Monnier, P.; van den Bergh, H. Three-dimensional optical phantom and its application in photodynamic therapy. *Lasers in Surgery and Medicine* **1997**, *21*, 227-234, doi:10.1002/(SICI)1096-9101

73.   Pogue, B.W.; Patterson, M.S. Review of tissue simulating phantoms for optical spectroscopy, imaging and dosimetry. *Journal of Biomedical Optics* **2006**, *11*, 041102, doi:10.1117/1.2335429.

74.   Lualdi, M.; Colombo, A.; Farina, B.; Tomatis, S.; Marchesini, R. A phantom with tissue-like optical properties in the visible and near infrared for use in photomedicine. *Lasers in Surgery and Medicine* **2001**, *28*, 237-243, doi:10.1002/lsm.1044.

75.   Beck, G.C.; Akgün, N.; Rück, A.; Steiner, R. Design and Characterisation of a Tissue Phantom System for Optical Diagnostics. *Lasers in Medical Science* **1998**, *13*, 160-171, doi:10.1007/s101030050070.

76.   Lamouche G, K.B., Kennedy KM, Bisaillon CE, Curatolo A, Campbell G, Pazos V, Sampson DD. Review of tissue simulating phantoms with controllable optical, mechanical and structural properties for use in optical coherence tomography. *Biomedical Optics Express* **2012**, *3*, 1381-1398, doi:10.1364/BOE.3.001381.

77.   Tomm, N.; Ahnen, L.; Isler, H.; Kleiser, S.; Karen, T.; Ostojic, D.; Wolf, M.; Scholkmann, F. Characterization of the optical properties of color pastes for the design of optical phantoms mimicking biological tissue. *Journal of Biophotonics* **2019**, *12*, e201800300, doi:10.1002/jbio.201800300.

78.   Bisaillon, C.-É.; Dufour, M.L.; Lamouche, G. Artery phantoms for intravascular optical coherence tomography: healthy arteries. *Biomedical Optics Express* **2011**, *2*, 2599-2613, doi:10.1364/BOE.2.002599.

79.   Krauter, P.; Nothelfer, S.; Bodenschatz, N.; Simon, E.; Stocker, S.; Foschum, F.; Kienle, A. Optical phantoms with adjustable subdiffusive scattering parameters. *Journal of Biomedical Optics* **2015**, *20*, 105008-105001, doi:10.1117/1.jbo.20.10.105008.short.

80.   Rich, P. The molecular machinery of Keilin's respiratory chain. *Biochemical Society Transactions* **2003**, 1095-1105, doi:10.1042/BST0311095.

81.   Chaudhry, R.; Varacallo., M. Biochemistry, Glycolysis. **2022**.

82.   Melkonian, E.A.; Schury, M.P. Biochemistry, Anaerobic Glycolysis. **2022**.

83.   Hutchinson, P.J.; Jalloh, I.; Helmy, A.; Carpenter, K.L.H.; Rostami, E.; Bellander, B.-M.; Boutelle, M.G.; Chen, J.W.; Claassen, J.; Dahyot-Fizelier, C.; et al. Consensus statement from the 2014 International Microdialysis Forum. *Intensive Care Medicine* **2015**, *41*, 1517-1528, doi:10.1007/s00134-015-3930-y.

84.   Tisdall, M.M.; Smith, M. Cerebral microdialysis: research technique or clinical tool. *British Journal of Anaesthesia* **2006**, *97*, 18-25, doi:10.1093/bja/ael109.

85.   Nordström, C.-H. Cerebral energy metabolism and microdialysis in neurocritical care. *Child's Nervous System* **2010**, *26*, 465-472, doi:10.1007/s00381-009-1035-z.

86.   Ko, T.S.; Mavroudis, C.D.; Benson, E.J.; Forti, R.M.; Melchior, R.W.; Boorady, T.W.; Morano, V.C.; Mensah-Brown, K.; Lin, Y.; Aronowitz, D.; et al. Correlation of Cerebral Microdialysis with Non-Invasive Diffuse Optical Cerebral Hemodynamic Monitoring during Deep Hypothermic Cardiopulmonary Bypass. *Metabolites* **2022**, *12*, 737, doi:10.3390/metabo12080737.

87.   71 High Cut-Off Brain Microdialysis Catheter. **2020**.

88.   Merenda, A.; Gugliotta, M.; Holloway, R.; Levasseur, J.E.; Alessandri, B.; Sun, D.; Bullock, M.R. Validation of brain extracellular glycerol as an indicator of cellular membrane damage due to free radical activity after traumatic brain injury. *Journal of Neurotrauma* **2008**, *25*, 527-537, doi:10.1089/neu.2007.0359.

89.   Hillered, L.; Valtysson, J.; Enblad, P.; Persson, L. Interstitial glycerol as a marker for membrane phospholipid degradation in the acutely injured human brain. *Journal of Neurology, Neurosurgery & Psychiatry* **1998**, *64*, 486-491, doi:10.1136/jnnp.64.4.486.

90.   Reinstrup, P.; Ståhl, N.; Mellergård, P.; Uski, T.; Ungerstedt, U.; Nordström, C.-H. Intracerebral Microdialysis in Clinical Practice: Baseline Values for Chemical Markers during Wakefulness, Anesthesia, and Neurosurgery. *Neurosurgery* **2000**, *47*.

91.   Zeiler, F.A.; Thelin, E.P.; Helmy, A.; Czosnyka, M.; Hutchinson, P.J.A.; Menon, D.K. A systematic review of cerebral microdialysis and outcomes in TBI: relationships to patient functional outcome, neurophysiologic measures, and tissue outcome. *Acta Neurochirurgica* **2017**, *159*, 2245-2273, doi:10.1007/s00701-017-3338-2.

92.   Minassian, A.T.; Desfontis, J.C.; Gautier, F.; Douart, C.; Ursino, M.; Denizot, B.; Gogny, M.; Beydon, L. Comparison of Local Measurement of Cerebral Metabolism and to Cerebral PvO2 during Alterations in Intracranial Pressure, PaCO2 and Arterial Pressure – An Experimental Study in Goat. *Journal of Clinical Monitoring and Computing* **2002**, *17*, 403-411, doi:10.1023/a:1026257714988.

93.   Menon, D.K.; Coles, J.P.; Gupta, A.K.; Fryer, T.D.; Smielewski, P.; Chatfield, D.A.; Aigbirhio, F.; Skepper, J.N.; Minhas, P.S.; Hutchinson, P.J.; et al. Diffusion limited oxygen delivery following head injury*. *Critical Care Medicine* **2004**, *32*, 1384-1390, doi:10.1097/01.Ccm.0000127777.16609.08.

94.   Hadanny, A.; Efrati, S. Oxygen - a limiting factor for brain recovery. *Critical Care* **2015**, *19*, doi:10.1186/s13054-015-1034-2.

95.   Larsen, S.; Nielsen, J.; Hansen, C.N.; Nielsen, L.B.; Wibrand, F.; Stride, N.; Schroder, H.D.; Boushel, R.; Helge, J.W.; Dela, F.; et al. Biomarkers of mitochondrial content in skeletal muscle of healthy young human subjects. *J Physiol* **2012**, *590*, 3349-3360, doi:10.1113/jphysiol.2012.230185.

96.   Mavroudis, C.D.; Karlsson, M.; Ko, T.; Hefti, M.; Gentile, J.I.; Morgan, R.W.; Plyler, R.; Mensah-Brown, K.G.; Boorady, T.W.; Melchior, R.W.; et al. Cerebral mitochondrial dysfunction associated with deep hypothermic circulatory arrest in neonatal swine. *Eur J Cardiothorac Surg* **2018**, *54*, 162-168, doi:10.1093/ejcts/ezx467.

97.   Volk, L.E.; Mavroudis, C.D.; Ko, T.; Hallowell, T.; Delso, N.; Roberts, A.L.; Starr, J.; Landis, W.; Lin, Y.; Hefti, M.; et al. Increased cerebral mitochondrial dysfunction and reactive oxygen species with cardiopulmonary bypass. *European Journal of Cardio-Thoracic Surgery* **2020**, doi:10.1093/ejcts/ezaa439 %1 ezaa439.

98.   Kilbaugh, T.J.; Karlsson, M.; Duhaime, A.C.; Hansson, M.J.; Elmer, E.; Margulies, S.S. Mitochondrial response in a toddler-aged swine model following diffuse non-impact traumatic brain injury. *Mitochondrion* **2016**, *26*, 19-25, doi:10.1016/j.mito.2015.11.001.

99.   Mavroudis, C.D.; Karlsson, M.; Ko, T.; Hefti, M.; Gentile, J.I.; Morgan, R.W.; Plyler, R.; Mensah-Brown, K.G.; Boorady, T.W.; Melchior, R.W.; et al. Cerebral mitochondrial dysfunction associated with deep hypothermic circulatory arrest in neonatal swine†. *European Journal of Cardio-Thoracic Surgery* **2018**, *54*, 162-168, doi:10.1093/ejcts/ezx467.

100.   Piantadosi, C.A.; Zhang, J. Mitochondrial Generation of Reactive Oxygen Species After Brain Ischemia in the Rat. *Stroke* **1996**, *27*, 327-332, doi:10.1161/01.STR.27.2.327.

101.   Cao, W.; Carney, J.M.; Duchon, A.; Floyd, R.A.; Chevion, M. Oxygen free radical involvement in ischemia and reperfusion injury to brain. *Neuroscience Letters* **1988**, *88*, 233-238, doi:10.1016/0304-3940(88)90132-2.

102.   Helps, S.C.; Thornton, E.; Kleinig, T.J.; Manavis, J.; Vink, R. Automatic Nonsubjective Estimation of Antigen Content Visualized by Immunohistochemistry Using Color Deconvolution. *Applied Immunohistochemistry & Molecular Morphology* **2012**, *20*.

103.   Pelinka, L.E.; Kroepfl, A.; Schmidhammer, R.; Krenn, M.; Buchinger, W.; Redl, H.; Raabe, A. Glial Fibrillary Acidic Protein in Serum After Traumatic Brain Injury and Multiple Trauma. *Journal of Trauma and Acute Care Surgery* **2004**, *57*.

104.   Hovens, I.; Nyakas, C.; Schoemaker, R. A novel method for evaluating microglial activation using ionized calcium-binding adaptor protein-1 staining: cell body to cell size ratio. *Neuroimmunology and Neuroinflammation* **2014**, *1*, 82, doi:10.4103/2347-8659.139719.

105.   Pinheiro, J.C.; Bates, D.M. *Mixed-Effects Models in S and S-PLUS*; Springer New York: 2000.

106.   Oberg, A.L.; Mahoney, D.W. Linear Mixed Effects Models. Humana Press: 2007; pp. 213-234.

107.   Farzam, P.; Buckley, E.M.; Lin, P.-Y.; Hagan, K.; Grant, P.E.; Inder, T.E.; Carp, S.A.; Franceschini, M.A. Shedding light on the neonatal brain: probing cerebral hemodynamics by diffuse optical spectroscopic methods. *Scientific Reports* **2017**, *7*, doi:10.1038/s41598-017-15995-1.

108.   Giovannella, M.; Contin, D.; Pagliazzi, i.; Pifferi, A.; Spinelli, L.; Erdmann, R.; Donat, R.; Rocchetti, I.; Rehberger, M.; König, N.; et al. BabyLux device: a diffuse optical system integrating diffuse correlation spectroscopy and time-resolved near-infrared spectroscopy for the neuromonitoring of the premature newborn brain. *Neurophotonics* **2019**, *6*, 025007, doi:10.1117/1.nph.6.2.025007.

109.   Gelman, A.; Hill, J. *Data Analysis Using Regression and Multilevel/Hierarchical Models*; Cambridge University Press: New York, 2007.

110.   Huisenga, D.; La Bastide-Van Gemert, S.; Van Bergen, A.; Sweeney, J.; Hadders-Algra, M. Developmental outcomes after early surgery for complex congenital heart disease: a systematic review and meta-analysis. *Developmental Medicine & Child Neurology* **2021**, *63*, 29-46, doi:10.1111/dmcn.14512.

111.   Gaynor, J.W.; Stopp, C.; Wypij, D.; Andropoulos, D.B.; Atallah, J.; Atz, A.M.; Beca, J.; Donofrio, M.T.; Duncan, K.; Ghanayem, N.S.; et al. Neurodevelopmental Outcomes After Cardiac Surgery in Infancy. *Pediatrics* **2015**, *135*, 816-825, doi:10.1542/peds.2014-3825.

112.   Wernovsky, G.; Shillingford, A.J.; Gaynor, J.W. Central nervous system outcomes in children with complex congenital heart disease. *Current Opinion in Cardiology* **2005**, *20*, 94-99, doi:10.1097/01.hco.0000153451.68212.68.

113.   Beca, J.; Gunn, J.K.; Coleman, L.; Hope, A.; Reed, P.W.; Hunt, R.W.; Finucane, K.; Brizard, C.; Dance, B.; Shekerdemian, L.S. New White Matter Brain Injury After Infant Heart Surgery Is Associated With Diagnostic Group and the Use of Circulatory Arrest. *Circulation* **2013**, *127*, 971-979, doi:10.1161/circulationaha.112.001089.

114.   Caputo, M.; Mokhtari, A.; Miceli, A.; Ghorbel, M.T.; Angelini, G.D.; Parry, A.J.; Suleiman, S.M. Controlled reoxygenation during cardiopulmonary bypass decreases markers of organ damage, inflammation, and oxidative stress in single-ventricle patients undergoing pediatric heart surgery. *The Journal of Thoracic and Cardiovascular Surgery* **2014**, *148*, 792-801.e798, doi:10.1016/j.jtcvs.2014.06.001.

115.   Hirsch, J.C.; Jacobs, M.L.; Andropoulos, D.; Austin, E.H.; Jacobs, J.P.; Licht, D.J.; Pigula, F.; Tweddell, J.S.; Gaynor, J.W. Protecting the Infant Brain During Cardiac Surgery: A Systematic Review. *The Annals of Thoracic Surgery* **2012**, *94*, 1365-1373, doi:10.1016/j.athoracsur.2012.05.135.

116.   Kansy, A.; Tobota, Z.; Maruszewski, P.; Maruszewski, B. Analysis of 14,843 Neonatal Congenital Heart Surgical Procedures in the European Association for Cardiothoracic Surgery Congenital Database. *The Annals of Thoracic Surgery* **2010**, *89*, 1255-1259, doi:10.1016/j.athoracsur.2010.01.003.

117.   Greeley, W.J.; Kern, F.H.; Ungerleider, R.M.; Boyd, J.L.; Quill, T.; Smith, L.R.; Baldwin, B.; Reves, J.G.; Sabiston, D.C. The effect of hypothermic cardiopulmonary bypass and total circulatory arrest on cerebral metabolism in neonates, infants, and children. *The Journal of Thoracic and Cardiovascular Surgery* **1991**, *101*, 783-794, doi:10.1016/S0022-5223(19)36647-4.

118.   Mavroudis, C.D.; Karlsson, M.; Ko, T.S.; Hefti, M.; Gentile, J.I.; Morgan, R.W.; Plyler, R.; Mensah-Brown, K.G.; Boorady, T.W.; Melchior, R.W.; et al. Cerebral Mitochondrial Dysfunction Associated with Deep Hypothermic Circulatory Arrest in Neonatal Swine. *European Journal of Cardio-Thoracic Surgery* **2018**, *54*, 162-168.

119.   Mavroudis, C.D.; Ko, T.; Volk, L.E.; Smood, B.; Morgan, R.W.; Lynch, J.M.; Davarajan, M.; Boorady, T.W.; Licht, D.J.; Gaynor, J.W.; et al. Does supply meet demand? A comparison of perfusion strategies on cerebral metabolism in a neonatal swine model. *The Journal of Thoracic and Cardiovascular Surgery* **2022**, *163*, e47-e58, doi:10.1016/j.jtcvs.2020.12.005.

120.   Ferradal, S.L.; Yuki, K.; Vyas, R.; Ha, C.G.; Yi, F.; Stopp, C.; Wypij, D.; Cheng, H.H.; Newburger, J.W.; Kaza, A.K.; et al. Non-invasive Assessment of Cerebral Blood Flow and Oxygen Metabolism in Neonates during Hypothermic Cardiopulmonary Bypass: Feasibility and Clinical Implications. *Scientific Reports* **2017**, *7*, 44117, doi:10.1038/srep44117.

121.   Levy, J.H.; Tanaka, K.A. Inflammatory Response to Cardiopulmonary Bypass. *The Annals of Thoracic Surgery* **2003**, *75*, S715-S720.

122.   Coleman, S.R.; Chen, M.; Patel, S.; Yan, H.; Kaye, A.D.; Zebrower, M.; Gayle, J.A.; Liu, H.; Urman, R.D. Enhanced Recovery Pathways for Cardiac Surgery. *Current Pain and Headache Reports* **2019**, *23*, doi:10.1007/s11916-019-0764-2.

123.   Saxena, S.; Maze, M. Impact on the brain of the inflammatory response to surgery. *La Presse Médicale* **2018**, *47*, e73-e81, doi:10.1016/j.lpm.2018.03.011.

124. Bronicki, R.A.; Hall, M. Cardiopulmonary Bypass-Induced Inflammatory Response: Pathophysiology and Treatment. *Pediatric Critical Care Medicine* **2016**, *17*.

125. Zangrillo, A.; Garozzo, F.A.; Biondi-Zoccai, G.; Pappalardo, F.; Monaco, F.; Crivellari, M.; Bignami, E.; Nuzzi, M.; Landoni, G. Miniaturized cardiopulmonary bypass improves short-term outcome in cardiac surgery: A meta-analysis of randomized controlled studies. *The Journal of Thoracic and Cardiovascular Surgery* **2010**, *139*, 1162-1169, doi:10.1016/j.jtcvs.2009.07.048.

126. Sarkar, M.; Prabhu, V. Basics of cardiopulmonary bypass. *Indian Journal of Anaesthisia* **2017**, *61*, 760-767, doi:10.4103/ija.IJA_379_17.

127. Jonas, R.; Wypij, D.; Roth, S.; Bellinger, D.; Visconti, K.; Du Plessis, A.; Goodkin, H.; Laussen, P.; Farrell, D.; Bartlett, J.; et al. The influence of hemodilution on outcome after hypothermic cardiopulmonary bypass: Results of a randomized trial in infants. . *The Journal of Thoracic and Cardiovascular Surgery* **2003**, *126*, 1765-1774, doi:10.1016/j.jtcvs.2003.04.003.

128. Sakamoto, T.; Zurakowski, D.; Duebener, L.F.; Hatsuoka, S.I.; Lidov, H.G.W.; Holmes, G.L.; Stock, U.A.; Laussen, P.C.; Jonas, R.A. Combination of alpha-stat strategy and hemodilution exacerbates neurologic injury in a survival piglet model with deep hypothermic circulatory arrest. *The Annals of Thoracic Surgery* **2002**, *73*, 180-189, doi:10.1016/s0003-4975(01)03274-x.

129. Ko, T.S.; Mavroudis, C.D.; Morgan, R.W.; Baker, W.B.; Marquez, A.M.; Boorady, T.W.; Devarajan, M.; Lin, Y.; Roberts, A.L.; Landis, W.P. Non-invasive diffuse optical neuromonitoring during cardiopulmonary resuscitation predicts return of spontaneous circulation. *Scientific reports* **2021**, *11*, 1-14.

130. O'Dwyer, C.; Prough, D.S.; Johnston, W.E. Determinants of cerebral perfusion during cardiopulmonary bypass. *Journal of Cardiothoracic and Vascular Anesthesia* **1996**, *10*, 54-65, doi:10.1016/S1053-0770(96)80179-0.

131. Fraser, C.D.; Andropoulos, D.B. Principles of Antegrade Cerebral Perfusion During Arch Reconstruction in Newborns/Infants. *Seminars in Thoracic and Cardiovascular Surgery: Pediatric Cardiac Surgery Annual* **2008**, *11*, 61-68, doi:10.1053/j.pcsu.2007.12.005.

132. Andropoulos, D.B.; Stayer, S.A.; McKenzie, E.D.; Fraser, C.D. Novel cerebral physiologic monitoring to guide low-flow cerebral perfusion during neonatal aortic arch reconstruction. *The Journal of Thoracic and Cardiovascular Surgery* **2003**, *125*, 491-499, doi:10.1067/mtc.2003.159.

133. Busija, D.W.; Leffler, C.W. Hypothermia reduces cerebral metabolic rate and cerebral blood flow in newborn pigs *American Journal of Physiology* **1987**, *253*, H713-H992, doi:10.1152/ajpheart.1987.253.4.H869.

134. Buckley, E.M.; Lynch, J.M.; Goff, D.A.; Schwab, P.J.; Baker, W.B.; Durduran, T.; Busch, D.R.; Nicolson, S.C.; Montenegro, L.M.; Naim, M.Y.; et al. Early postoperative changes in cerebral oxygen metabolism following neonatal cardiac surgery: Effects of surgical duration. *The Journal of Thoracic and Cardiovascular Surgery* **2013**, *145*, 196-205.e191, doi:10.1016/j.jtcvs.2012.09.057.

135. Yoshimura, A.; Shichita, T. Post-Ischemic Inflammation in the Brain. *Frontiers in Immunology* **2012**, *3*.

136. Gobiet, W.; Grote, W.; Bock, W.J. The relation between intracranial pressure, mean arterial pressure and cerebral blood flow in patients with severe head injury. *Acta Neurochirurgica* **1975**, *32*, 13-24, doi:10.1007/bf01405899.

137. Warltier, David C.; Laffey, John G.; Boylan, John F.; Cheng, Davy C.H. The Systemic Inflammatory Response to Cardiac Surgery: Implications for the Anesthesiologist. *Anesthesiology* **2002**, *97*, 215-252, doi:10.1097/00000542-200207000-00030.

138. Ono, M.; Joshi, B.; Brady, K.; Easley, R.B.; Zheng, Y.; Brown, C.; Baumgartner, W.; Hogue, C.W. Risks for impaired cerebral autoregulation during cardiopulmonary bypass and postoperative stroke. *British Journal of Anaesthesia* **2012**, *109*, 391-398, doi:10.1093/bja/aes148.

139. Lynch, J.M.; Ko, T.; Busch, D.R.; Newland, J.J.; Winters, M.E.; Mensah-Brown, K.; Boorady, T.W.; Xiao, R.; Nicolson, S.C.; Montenegro, L.M.; et al. Preoperative cerebral hemodynamics from birth to surgery in neonates with critical congenital heart disease. *The Journal of Thoracic and Cardiovascular Surgery* **2018**, *156*, 1657-1664, doi:10.1016/j.jtcvs.2018.04.098.

140. Jain, V.; Buckley, E.M.; Licht, D.J.; Lynch, J.M.; Schwab, P.J.; Naim, M.Y.; Lavin, N.A.; Nicolson, S.C.; Montenegro, L.M.; Yodh, A.G.; et al. Cerebral Oxygen Metabolism in Neonates with Congenital Heart Disease Quantified by MRI and Optics. *Journal of Cerebral Blood Flow & Metabolism* **2014**, *34*, 380-388, doi:10.1038/jcbfm.2013.214.

141. Takayama, J.; Teng, W.; Uyemoto, J.; Newman, T.; Pantell, R. Body temperature of newborns: what is normal? *Clinical Pediatrics* **2000**, *39*, 503-210, doi:10.1177/000992280003900901.

142. Condo, S.G.; Corda, M.; Sanna, M.T.; Pellegrini, M.G.; Ruiz, M.P.; Castagnola, M.; Giardina, B. Molecular basis of low-temperature sensitivity in pig hemoglobins. *European Journal of Biochemistry* **1992**, *209*, 773-776, doi:10.1111/j.1432-1033.1992.tb17347.x.

143. Baik-Schneditz, N.; Schwaberger, B.; Urlesberger, B.; Wolfsberger, C.H.; Bruckner, M.; Pichler, G. Acid base and blood gas analysis in term neonates immediately after birth with uncomplicated neonatal transition. *BMC Pediatrics* **2022**, *22*, doi:10.1186/s12887-022-03324-z.

144. Peng, Y.-W.; Mohammed, A.; Deatrick, K.B.; Major, T.; Cheng, D.; Charpie, I.; Charpie, J.R. Differential Effects of Normoxic and Hyperoxic Reperfusion on Global Myocardial Ischemia-Reperfusion Injury. *Seminars in Thoracic and Cardiovascular Surgery* **2019**, *31*, 188-198, doi:10.1053/j.semtcvs.2018.09.018.

145. Yücel, M.A.; Selb, J.; Boas, D.A.; Cash, S.S.; Cooper, R.J. Reducing motion artifacts for long-term clinical NIRS monitoring using collodion-fixed prism-based optical fibers. *NeuroImage* **2014**, *85*, 192-201, doi:10.1016/j.neuroimage.2013.06.054.

146. Rajaram, A.; Milej, D.; Suwalski, M.; Yip, L.C.M.; Guo, L.R.; Chu, M.W.A.; Chui, J.; Diop, M.; Murkin, J.M.; Lawrence, K.S. Optical monitoring of cerebral perfusion and metabolism in adults during cardiac surgery with cardiopulmonary bypass. *Biomedical Optics Express* **2020**, *11*, 2967-5981, doi:10.1364/BOE.404101.

147. Selb, J.; Wu, K.-C.; Sutin, J.; Lin, P.-Y.; Farzam, P.; Bechek, S.; Shenoy, A. Prolonged monitoring of cerebral blood flow and autoregulation with diffuse correlation spectroscopy in neurocritical care patients. *Neurophotonics* **2018**, *5*, 1, doi:10.1117/1.nph.5.4.045005.

148. Zirak, P.; Delgado-Mederos, R.; Dinia, L.; Carrera, D.; Martí-Fàbregas, J.; Durduran, T. Transcranial diffuse optical monitoring of microvascular cerebral hemodynamics after thrombolysis in ischemic stroke. *Journal of Biomedical Optics* **2014**, *19*, 018002, doi:10.1117/1.jbo.19.1.018002.

149. Wheelock, M.D.; Culver, J.P.; Eggebrecht, A.T. High-density diffuse optical tomography for imaging human brain function. *Review of Scientific Instruments* **2019**, *90*, 051101, doi:10.1063/1.5086809.

150. Matlis, G.C.; Zhang, Q.; Benson, E.J.; Weeks, M.K.; Andersen, K.; Jahnavi, J.; Lafontant, A.; Breimann, J.; Hallowell, T.; Lin, Y.; et al. Chassis-based fiber-coupled probe design for reproducible quantitative diffuse optical spectroscopy measurements. **under review**.

151. Lewis, A.; Forti, R.M.; Alomaja, O.; Mesaros, C.; Piel, S.; Greenwood, J.C.; Talebi, F.M.; Mavroudis, C.D.; Kelly, M.; Kao, S.-H.; et al. Preliminary Research: Application of Non-Invasive Measure of Cytochrome c Oxidase Redox States and Mitochondrial Function in a Porcine Model of Carbon Monoxide Poisoning. *Journal of Medical Toxicology* **2022**, *18*, 214-222, doi: 10.1007/s13181-022-00892-5.

152. Forti, R.M.; Hobson, L.J.; Benson, E.J.; Ko, T.S.; Ranieri, N.R.; Laurent, G.; Weeks, M.K.; Widmann, N.J.; Morton, S.; Davis, A.M.; et al. Non-invasive diffuse optical monitoring of cerebral physiology in an adult swine-model of impact traumatic brain injury. *Biomedical Optics Express* **2023**, *14*, 2432-2448, doi:10.1364/BOE.486363.

153. Sherkat, H.; Pinto-Orellana, M.A.; Mirtaheri, P. SHADE: Absorption spectroscopy enhancement with ambient light estimation and narrow-band detection. *Optik* **2020**, *220*, 165116, doi:10.1016/j.ijleo.2020.165116.

154. Lin, P.-Y.; Roche-Labarbe, N.; Dehaes, M.; Fenoglio, A.; Grant, P.E.; Franceschini, M.A. Regional and Hemispheric Asymmetries of Cerebral Hemodynamic and Oxygen Metabolism in Newborns. *Cerebral Cortex* **2013**, *23*, 339-348, doi:10.1093/cercor/bhs023.

155. Brigadoi, S.; Ceccherini, L.; Cutini, S.; Scarpa, F.; Scatturin, P.; Selb, J.; Gagnon, L.; Boas, D.A.; Cooper, R.J. Motion artifacts in functional near-infrared spectroscopy: A comparison of motion correction techniques applied to real cognitive data. *NeuroImage* **2014**, *85*, 181-191, doi:10.1016/j.neuroimage.2013.04.082.

156. Dehaes, M.; Grant, P.E.; Sliva, D.D.; Roche-Labarbe, N.; Pienaar, R.; Boas, D.A.; Franceschini, M.A.; Selb, J. Assessment of the frequency-domain multi-distance method to evaluate the brain optical properties: Monte Carlo simulations from neonate to adult. *Biomedical Optics Express* **2011**, *2*, 552-567, doi:10.1364/BOE.2.000552.

157. Ahmad, F.B.; Anderson, R.N. The Leading Causes of Death in the US for 2020. *JAMA* **2021**, *325*, 1829, doi:10.1001/jama.2021.5469.

158. D, N.-O.; JC, S.-M. *Neuroanatomy, Middle Cerebral Artery*; StatPearls Publishing: Treasure Island (FL), 2022.

159. Forti, R.M.; Favilla, C.G.; Cochran, J.M.; Baker, W.B.; Detre, J.A.; Kasner, S.E.; Mullen, M.T.; Messé, S.R.; Kofke, W.A.; Balu, R.; et al. Transcranial Optical Monitoring of Cerebral Hemodynamics in Acute Stroke Patients during Mechanical Thrombectomy. *Journal of Stroke and Cerebrovascular Diseases* **2019**, *28*, 1483-1494, doi:10.1016/j.jstrokecerebrovasdis.2019.03.019.

160. Favilla, C.G.; Forti, R.M.; Zamzam, A.; Detre, J.A.; Mullen, M.T.; Yodh, A.G.; Kasner, S.E.; Busch, D.R.; Baker, W.B.; Mesquita, R.C.; et al. Perfusion Enhancement with Respiratory Impedance After Stroke (PERI-Stroke). *Neurotherapeutics* **2019**, *16*, 1296-1303, doi:10.1007/s13311-019-00744-1.

161. Favilla, C.G.; Mesquita, R.C.; Mullen, M.; Durduran, T.; Lu, X.; Kim, M.N.; Minkoff, D.L.; Kasner, S.E.; Greenberg, J.H.; Yodh, A.G.; et al. Optical Bedside Monitoring of Cerebral Blood Flow in Acute Ischemic Stroke Patients During Head-of-Bed Manipulation. *Stroke* **2014**, *45*, 1269-1274, doi:10.1161/strokeaha.113.004116.

162. Pringle, J.; Roberts, C.; Kohl, M.; Lekeux, P. Near Infrared Spectroscopy in Large Animals: Optical Pathlength and Influence of Hair Covering and Epidermal Pigmentation. *The Veterinary Journal* **1999**, *158*, 48-52, doi:10.1053/tvjl.1998.0306.

163. Strangman, G.; Boas, D.A.; Sutton, J.P. Non-invasive neuroimaging using near-infrared light. *Biological Psychiatry* **2002**, *52*, 679-693, doi:10.1016/S0006-3223(02)01550-0.

164. Robbins, C.R. *Chemical and Physical Behavior of Human Hair*, 4th ed.; Springer-Verlag: New York, 2002.

165. Jimenez, F.; Ruifernández, J.M. Distribution of Human Hair in Follicular Units: A Mathematical Model for Estimating the Donor Size in Follicular Unit Transplantation. *Dermatologic Surgery* **1999**, *25*.